Magnetic Nanoparticles and Clusters for Magnetic Hyperthermia: optimizing their heat performance and developing combinatorial therapies to tackle cancer

Helena Gavilán,[a] Sahitya Kumar Avugadda,[a] Tamara Fernández-Cabada,[a] Nisarg Soni,[a] Marco Cassani,[a,%] Binh T. Mai,[a] Roy Chantrell[b] and Teresa Pellegrino[a*]*

[a] *Istituto Italiano di Tecnologia, via Morego 30, 16163 Genoa, Italy*

[b] *Department of Physics, University of York, York YO10 5DD, United Kingdom*

% Current affiliation: International Clinical Research Center (FNUSA-ICRC), St. Anne's University Hospital, Brno, Czech Republic

Abstract: Magnetic hyperthermia (MHT) is a therapeutic modality for the treatment of solid tumors that has now accumulated more than 30-year experience. In the ongoing MHT clinical trials for brain and prostate tumors treatments, iron oxide nanoparticles are employed as intra-tumoral MHT agents under a patient safe 100-kHz alternating magnetic field (AMF) applicator. Although iron oxide nanoparticles are currently FDA approved for imaging purposes and for anemia treatments, magnetic nanoparticles (MNPs) designed for an efficient MHT treatment must respond to specific physical-chemical properties in terms of magneto-energy conversion, heat dose production, surface chemistry and aggregation state. This need, in the past few decades, has boosted the development of a new generation of MNPs, specifically aimed for MHT. In this review, we will give an excursion on MNPs and their assemblies produced by different synthetic routes, stressing which MNPs features have enabled to reach unprecedented levels of heating efficiency in MHT and highlighting those nanoplatforms preserving magnetic heat losses in an intracellular environment. Moreover, we will review advances on MNPs based nano-platforms that embrace the concept of multimodal therapy aiming at combining MHT with chemotherapy, radiotherapy, immunotherapy, photodynamic or phototherapy. Next, for a better control of the therapeutic temperature at the tumor, we will focus on those studies that have optimized MNPs to maintain gold-standard MHT performances and are also tackling MNP imaging with the aim to quantitatively assess the amount of nanoparticles accumulated at the tumor site and regulate the MHT field conditions. To conclude, future perspectives with guidance on how to advance MHT therapy will be provided.

Keywords: Magnetic hyperthermia, Magnetic nanoparticles, assembly of nanoparticles, iron oxide, Viscosity and microenvironment effect, cancer therapy, chemotherapy, immunotherapy, radiotherapy, photodynamic tehrapy.

1. Introduction

In the area of nanotechnology-based cancer research, MNPs are assuming a central role as they can be tuned to provide functionality for multiple tasks both in diagnostic and therapeutic applications.[1] In MHT,

the temperature increase at a therapeutic range (42 – 46 °C) mediated by MNPs under an alternating magnetic field (AMF) is exploited to kill tumor cells.[2] Currently, MHT is based on the intratumoral administration of MNPs.[3] More specifically, superparamagnetic iron oxide nanoparticles (SPIONs) directly deposited at the tumor act as transducer to convert electromagnetic energy into heat upon exposure to an AMF of kHz radiofrequency range (100-300 kHz) and an appropriate field intensity (few tens of kA/m).[3-8] This approach received the first medical device European approval for the treatment of Glioblastoma Multiforme (GBM) brain tumor;[4] and more recently, the clinical trials for the U. S. Food and Drug Administration (FDA) for treating prostate[4] and pancreatic cancer[3] are ongoing.

From the past few decades, there has been hectic research aiming at developing MNPs for MHT and correlating heating performances of MNPs to i) their structural and magnetic properties;[5-11]; ii) the AMF parameters [12, 13] iii) the microenvironment (i.e. the tumor milieu)[14, 15]; iv) the understanding and modelling of the MNP heating mechanism.[16-22]

Keeping as a reference the outcome of the clinical trials where MHT is combined with standard chemotherapy and/or radiotherapy, this therapeutic approach although promising, does not enable to achieve a complete tumor regression.[23] Multiple reasons may be responsible for such an outcome, but the heat performances of the injected MNPs play a crucial role. Moreover, the direct heat effects favoring cell death, the temperature increase of MNPs,[24] may be exploited to promote other AMF-triggered therapeutic modality (i.e. chemotherapy). Alternatively, they can be merged with other therapeutic modalities that favour disruption of cell metabolic pathways in a synergistic approach.

In recent years, combinatorial cancer therapies have offered more promising outcomes with respect to that of monotherapies. A combination of MHT with other therapeutic modalities such as, photothermal, photodynamic, radio, immunotherapy and chemotherapies have required the development of MNPs-based platforms aimed for improving synergic effects to improve tumor therapeutic efficiency with minimal adverse effects.[25, 26] More specifically, for a more efficacious and specific tumor treatment, we will review the MNPs used in clinical and pre-clinical studies in which MHT has been exploited to render tumor cells: i) more sensible to a drug, which is selectively released at the tumor site under specific physical stimuli (chemotherapy), ii) more exposed to oxygen species including reoxygenation (radiotherapy) or radical oxygen species production (photodynamic therapy), iii) more responsive to the immune response (immunotherapy) and iv) to synergic enhance heat damage effects by multimodal heat-based therapies (photo-thermal (PTT) therapy).

Here, we will first overview few basic physical principles of MHT, highlighting the connection between the magnetic and physical parameters of the MNPs with the equations describing the heat dissipation in MHT. We will provide an update of the MHT performances of MNPs with respect to the preparation routes, their structural and magnetic features including, size, size distribution, crystallinity, shape, composition, magnetic parameters and their aggregation/assemblies state. Within this comparison, we will always point out to the assessment of performances at clinical magnetic parameters. It will follow the development of the main MNP-based materials that have enabled to combine MH with other therapeutic modalities and that have already shown promising outcomes in clinical and pre-clinical (*in vivo*) studies.

In this regard, it is important to point out that, despite the 30 years of clinical trials of MNPs in MHT, so far MNP-based materials have been approved as medical devices and not yet as pharmaceutical formulations[27-38].There is however a long way ahead for the regulatory approval of newly discovered MNP-based materials, which would need to prove advances with respect to the unmet needs of a spatial and temporal controlled MHT heat therapy alone or in combination with other smart therapeutic

modalities. This will help the transition towards an ultimately “personalized heat medicine” while possibly enabling the use of standard diagnostic tools for the tumor diagnosis.[39, 40]

As a note to the reader, although we aimed at covering the different topics of this review in an exhaustive way, we have made a selection of works to be included based on two main criteria. The first one is based on the need to compare MHT data with each other, therefore we have selected those studies that were reporting basic and needed information, in order to properly compare heat performances of the MNPs materials. The second criterion regards the choice of those biological studies that, besides providing a well-documented MNP materials information, had also reported preclinical data on a murine model thus more advanced than test tube or *in vitro* cell studies.

We finally close this review with some future perspectives, to provide scientific tips to tackle actual limitations of the state of the art technology and to highlight the most promising future developments for the magnetic material developments to be undertaken for a most effective MHT-based tumor therapy.

2.1. Basic principles of Magnetic hyperthermia

With the aim to design optimized magnetic nanomaterials for MHT application, understand the principles of MHT and correlate the main heat dissipation equations to magnetic and physical parameters of the MNPs requires a brief introduction of basicl concept of MHT. MHT is the electromagnetic energy conversion to heat mediated by MNPs and it is caused by the coupling of the magnetic moments (*m*) of the atoms that constitute the MNPs with the time-varying external magnetic field applied.[41] To understand this concept, few basic notions on magnetic materials need to be recalled. Once MNPs are exposed to an external magnetic field, their magnetic moments align with the external field with a degree of orientation depending on the materials features (crystal structures, composition, size and shape), the amplitude of the external magnetic field (H) and the temperature. The response of the magnetic moment of MNPs to the (H) is often recorded, obtaining the so-called magnetization (M) versus field (H) curves. These curves enable us to classify magnetic materials in different categories (i.e. ferro/ferrimagnetic, antiferromagnetic, paramagnetic, diamagnetic, etc.). Such characteristic M(H) curves are called hysteresis loops, and the following parameters can be extracted from them: the saturation magnetization (M_s), the remanent magnetization (M_r) and the coercivity (H_c).[42]

For bulk magnetic materials, magnetic properties, including hysteresis, are dominated by a magnetic structure formed of magnetic domains separated by domain walls. However, below a certain particle size, a single magnetic domain becomes energetically more favourable than multidomains. Such critical size of mono-domain depends on the balance of several energies within the material, which are derived from the composition and shape of the MNPs in addition to the domain wall energy.

In addition, the crystal lattice of most magnetic materials has magnetic anisotropy, which means they have an "easy" direction of magnetization, parallel to one of the crystal axes. The magnetic moment of mono-domain MNPs has usually only two stable orientations antiparallel to each other (along the easy axis of magnetization), separated by an energy barrier, which is called the anisotropic energy (E_a) and it is proportional to the magneto-crystalline anisotropy constant (K) and the magnetic volume (V) of the MNPs (E_a=KV). The smaller the nanoparticle is, the lower is the energy barrier needed to invert the magnetic spin. When thermal energy k_BT (k_B being the Boltzmann constant) is sufficiently high, the particle spins will be switched randomly between the minima. Below a critical diameter value, the magnetic moments of the particles are spontaneously and continuously reversed by thermal activation, and the total magnetic moment of the particle is averaged to zero. This phenomenon is called superparamagnetism and it is characterized by the absence of coercivity in the M(H) curve. For superparamagnetic MNPs, high magnetic

moments are observed under the effect of a magnetic field (high M_s), but no remanent magnetic moment is present when the external magnetic field is removed. The M(H) curve of superparamagnetic MNPs does not show any hysteresis cycle. MNPs displaying a superparamagnetic behavior at body temperature (T= 37°C) are particularly desirable for MHT, as they will serve as inert and non-interacting heating probes/carriers/ or tracers in absence of an external magnetic field but they are easily activated in presence of an external field. Because of the dynamics of the process, the critical volume V_c is dependent on the measurement timescale (t) such that $KV_c = \ln(f_0 t)$, where the frequency factor $f_0 \approx 10^9 s^{-1}$. This is important because, although the MNPs behave as superparamagnets at low frequencies, at the high frequencies of the hyperthermia process, hysteresis is activated.[43]

In the presence of an AMF, the heating mechanism of single or multi-domain magnetic materials is different, but in both cases, it is related to the generation of the hysteresis cycle. By the first law of thermodynamics and the principle of conservation of energy, the heat generated by the MNPs (W_{heat}) corresponds to the magnetic work done by the electromagnetic field to align the atomic magnetic moments with the applied field (H) while the change in internal energy is kept constant. It can be determined through the contour integration ($\oint$) of H with respect to the magnetization (M), as described in equation 1:

$$W_{heat} = \oint H \cdot dM \text{ [Eq. 1]}$$

Therefore, the thermal loss is proportional to the area enclosed by the M(H) hysteresis loop when a H_{AC} field is applied (Figure 1a):

$$A = \oint \mu_0 M(H) H dH \text{ [Eq. 2]}$$

With the integration carried out over a hysteresis cycle.
The heat dissipation power (P) is given by the product of the area of each cycle (A) and the number of times per second (f) that the cycle is completed, giving P= A*x**f*

For superparamagnetic nanoparticles, to correlate the nanoparticle's features to the area of the hysteresis generated under AMF, the Rosensweig model can be applied.[44] In this model, the dynamic behavior of nanoparticles considers the linear approximation of the magnetic response of sample to the field applied and it can be written as that: **M**=χ**H** being χ the susceptibility with X= χ'-iχ" *where χ"* is the loss component of susceptibility and represents the portion of magnetization which is out of phase with respect to the magnetic field.

This theory, the linear response theory (LRT) – also called Néel–Brown relaxation model – can be applied for superparamagnetic NPs and for H_{AC} that is relatively small such that the susceptibility is to a good approximation field independent. Under this regime, P is equal to the product of the loop area (*A*) and the frequency (*f*), and is shown in (44) to be proportional to H_{max}^2 and *f* as follows :

$$P = f \times A = \mu_0 \pi H_{max}^2 f \chi'' \text{[Eq. 3]},$$

with μ_0 the permeability of free space. Finally, the loss component of susceptibility (*χ"*) can be further expressed as in Eq. 4:

$$\chi'' = \chi_0 [\omega\tau/(1+\omega\tau)^2] \text{[Eq. 4]}$$

With X_0 being the static susceptibility, which in turn is described in Eq. 5 as:

$$\chi_0 = \frac{M_S^2 V}{3k_b T}$$ [Eq. 5]

χ'' represents the dephasing of the moment of the MNPs with respect to the AMF and thus it reflects the opening of the area of hysteresis, which reaches its maximum a when ωτ=2πf=1.

The term τ is the effective relaxation time[45] and it can be expressed as :

$$\frac{1}{\tau} = \frac{1}{\tau_N} + \frac{1}{\tau_B}$$ [Eq. 6]

τ_N and τ_B are the Néel and Brownian relaxation times and are given by Eq. 7 and 8, respectively:

$$\tau_N = \tau_0 \exp(\frac{KV}{k_B T})$$ [Eq. 7]

$$\tau_B = \frac{3V_H \eta}{k_B T}$$ [Eq. 8]

The factor τ_0 can be considered as an 'attempt time' and its value is ≈ 10^{-13}–10^{-9} s,[46] η is the viscosity of the liquid containing the particles and V_H is the hydrodynamic volume of the particle. The Néel relaxation time is related to the thermal fluctuations of the magnetic moment of the MNPs while the Brownian relaxation time relates to the rotational fluctuations with the shortest time dominating the total relaxation time. It is generally accepted that for iron oxide (maghemite γ-Fe_2O_3 or magnetite Fe_3O_4) MNPs with a diameter smaller ca. 15 nm, τ_N is smaller than τ_B and hence τ is dominated by τ_N.

For MHT, it important to define the specific loss power (SLP, Eq. 10), also known as the specific absorption rate (SAR) that is the heat rate at which a magnetic material absorbs electromagnetic energy and converts it to heat.[47] The amount of heat generated by the MNPs depends on the area A of the hysteresis cycle recorded under the applied AMF, the frequency of the applied field and the density of the MNPs (ρ):

$$SAR = SLP = \frac{P}{\rho} = \frac{A f}{\rho}$$ [Eq. 10]

.

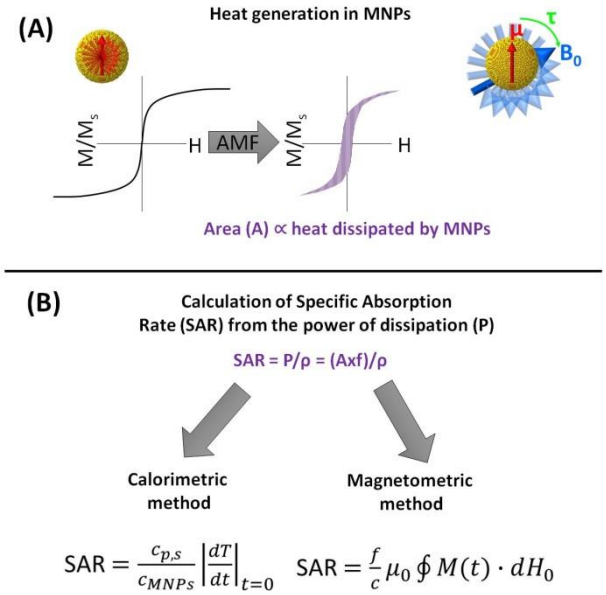

Figure 1. Basic principles of Magnetic Hyperthermia (MH): (a) mode of heat release by superparamagnetic MNPs under the influence of an alternating magnetic field (AMF) and hysteresis losses in MNPs: the larger the area of the hysteresis loop, the higher the power P dissipated by the MNPs. The formula for the power is shown. (b) Methods to determine the Specific Absorption Rate (SAR) in MNPs: calorimetric and magnetometric, with their corresponding formulas.

However, in the ferromagnetic regime or for MNPs close to the superparamagnetic/ferromagnetic transition, LRT is no more valid, and instead, theories derived from the Stoner–Wohlfarth (SW) model should be used,[17] in which the area of the hysteresis loop is calculated to be $A=\alpha\mu_0 M_s H_{C0}$ (for randomly oriented MNPs),[48] where $\alpha\approx 2$ and H_{C0} is the value of the coercive field at T= 0. MNPs in the SW regimes are highly desirable for MHT, as reported by Lacroix et al., at least in those cases where they can be saturated by H_{max}, and if they display a coercive field as large as possible but below H_{max}.[48] However, given the conditions of AMF used in the clinic for MHT, this only occurs in soft ferromagnetic NPs or superparamagnetic NPs close to the ferromagnetic transition. Thus, we can say that this kind of MNPs (single domain particles with uniaxial anisotropy) can display the highest magneto energy heat conversion.[49] On the other hand, when the particles are large enough to be multidomain, the reversal of the magnetization occurs by wall motion, leading to moderate heating.[50] We summarise the situation regarding models of hyperthermic heating as follows. The LRT and SW models are limiting cases. However, a more general approach exists, termed 'kinetic Monte-Carlo' (kMC) models.[51] These combine SW theory with Néel–Brown relaxation to introduce the mechanism of thermal activation over the anisotropy energy barrier. In Ruta S *et al*. work,[43] it was shown that the kMC approach which recover both the LRT and SW models in the appropriate limits and is a general approach for all time- and temperature- ranges relevant for MHT.

In order to determine the heat generated by MNPs, the specific absorption rates (SAR values) of a colloid of MNPs is measured either through calorimetric measurements (left) or by magnetometric measurements (right) using the corresponding formulas (Figure 1b), as it has been widely described in literature.[2, 52] Another complementary method to determine SAR values is through magnetometry measurements, by recording the dynamic magnetization M(t) of the sample under an AMF (Figure 1B). The SAR value is proportional to the area of the AC hysteresis loop.[2, 53] In addition, the magnetometric method is especially useful, as the dynamic hysteresis cycles can be easily compared in different media, aggregation state, concentration, etc. SAR values are quite often used in the literature to characterize and compare the heating ability of MNPs, however, they have the limitation of being somehow an equipment-specific measure, depending on the frequencies and amplitude of the applied AMF. In order to compare the heating ability among different samples and field conditions, SAR values can be normalized to the intrinsic loss power (ILP), as defined in Eq. 11:

$$ILP = \frac{SAR}{H^2 f} \text{ [Eq. 11]}$$

However, this normalization is valid only under certain conditions of frequencies (for f values up to several MHz) and field strengths (for H values well below the saturation field of the MNPs).[54] In addition, as noted from the formula, there is a field-frequency relation only applicable to superparamagnetic nanoparticles.

2.2. Biological limits for the field conditions.

Eq. 3 for superparamagnetic nanoparticles indicates that the heat dissipation depends on AMF conditions: it increases linearly with f and quadratic with field amplitude (H^2). However, f and H parameters cannot be arbitrary because body tissue may overheat due to the induced eddy current unless the product $H \times f$ is

maintained below a certain value.[1] The eddy current's non-specific heating is proportional to the square of the product H_{AC}×f and inversely proportional to the distance from the AMF source. Mamiya *et al.* calculated the eddy current (P_e) generated in humans using the following expression:

$$P_e = 1/2\,\pi^2 \mu_0^2 \sigma r^2 f^2 H_{AC}^2 \text{ [Eq. 14]}$$

Where σ is the electrical conductivity, assumed to be constant and to have a value of σ = 0.2 S×m^{-1} and r is the radius (of the simple model body considered), which is r = 0.1 m. [19]

Although currently there is no formally agreed value for the H_{AC}×f limit, the first proposed value was reported by Atkinson and Brezovich when using stainless-steel thermo seeds (≤ 4.85 × 10^8 A×m^{-1}×s^{-1}).[55]. Later, Hergt *et al.*[50] reported a biological acceptance limit of H_{AC}×f ≤ 5 ×10^9 A×m^{-1}×s^{-1}. This limit could be lower (H_{AC}×f from 4.2 ×10^9 to 1.6 ×10^9 A×m^{-1}×s^{-1}), accordingly to Jordan's first clinical trial on GBM patients or prostate carcinoma.[56] Lastly, Mamiya's work also calculates the heat transport, or cooling ability, caused by blood flow and approximates it to 0.06 MW×m^{-3}, and thus corresponds to a minimally acceptable P_e for the condition H_{AC}×f = 2 ×10^9 A×m^{-1}×s^{-1}.[19] All these values are summarized in Table 1.

Table 1. Limits of the Hf factor for the cancer treatment of MH in clinic.

Name	H×f(Am^{-1}s^{-1})	Ref
Atkinson-Brezovich	≤ 4.85 × 10^8	[55]
Hergt et al.	≤ 5 × 10^9	[50]
B. Thiesen & A. Jordan	≤ 1.8 × 10^9	[56]
H. Mamiya et al.	2 × 10^9	[19]

3. Synthesis of magnetic nanoparticles

3.1 Synthesis routes for optimal magnetic nanoparticles for MHT

Apart from the magnetic field conditions, as outline in section 2, it is also evident that some MNPs features such as M_s, V, and K have great impact on SAR values.[8] Understanding basic principles of MHT is necessary to correlate magento-energy conversion and heat performance to physical parameters important thus aiming to designed optimized magnetic nanomaterialsthat affect . The design of nanomaterials for MHT has been centered on the development of synthesis methods to tune such critical MNPs parameters, by adjusting the diameter (D), the shape/structure, and the composition.[57, 58] Table 2 summarizes the M_s and K for diverse MNPs reported in literature for the specific application of MHT and includes important information in this case like D, shape/structure and composition. M_s is often within the range of 40-200 emu·g^{-1}and K = 8 ×10^2 -1.6 ×10^5 J·m^{-3}. With respect to the volume, the optimal value is V = 0.5-27 x10^3 nm^3 (if we consider the most common morphologies, i.e nanospheres and nanocubes, this includes D between 10-40 nm); In addition, each synthesis method designed is associated with a characteristic size distribution. Narrow size distributions often lead to maximum heating efficiency because of the maximum coercivity found for the single domain size range.[59]

Table 2. Structural and magnetic properties of MNPs reported in literature for the specific application of Magnetic Hyperthermia. A, B, C stands for specific temperature conditions at which magnetic features were measured (a= 2 K, B= 300 K and C=10 K).

Composition	D (nm)	**Shape/ Structure**	M_s^{5K} (emug^{-1})	H_c^{5K} (Oe)	M_r/M_s^{5K}	K (J m^{-3})	Ref
$MnFe_2O_4$	7-18	**Spherical**	50-80	150	0.2-0.3	3.0 × 10^3	[60, 61, 62]
Fe_3O_4	4-17	**Spherical**	60-80	170-400	0.3	1.3 × 10^4	[63, 64, 65, 66]
$CoFe_2O_4$	6-12	**Spherical**	60-110	1200	0.6-0.7	2.0 × 10^5	[63, 67, 68]
$ZnFe_2O_4$	8	**Spherical**	42-78	200-400	0.1-0.2	- 6.7 × 10^4	[61, 69]
Fe(0)	12	**Spherical**	210[a]	145[a]	-	1.2 × 10^5	[70, 71]

Fe(0)/Fe$_{2.2}$C	13	**Spherical**	163[a]	212[a]		1.6×10^5	[70, 71]
Fe$_{2.2}$C	15	**Spherical**	170[a]	345[a]		3.7×10^5	[70, 71]
Fe$_3$O$_4$	12-38	**Cubic**	78-95	141-500	-	8×10^2	[72, 73, 74]
CoFe$_2$O$_4$	14-28	**Cubic**	58-73	800-1400	0.7-0.8	-	[75]
ZnFe$_2$O$_4$	18-120	**Cubic**	165-190	60-140	-	-	[76]
Fe	11-16	**Cubic**	178-200[b]	50-160[b]	0.06-0.2	1.6×10^5	[77, 78]
Fe$_3$O$_4$	17-47	**Octapods**	50-81[b]	0-103[b]	0.03-0.12[b]	$6.4\text{-}9.5 \times 10^3$	[79]
Fe$_3$O$_4$	40-70/5-10	**Nanorods**	20-80[b]	0-50[b]	-	-	[79, 80]
Fe$_3$O$_4$	20-28	**Nanoflowers**	83-88	200-290	0.36-0.45	$1.8\text{-}2.6 \times 10^4$	[81]
Fe$_3$O$_4$	13-260	**Octahedra**	68-92[b]	0-118	0-0.14	-	[82]
CoFe$_2$O$_4$@ MnFe$_2$O$_4$	15	**Spherical/ Core-shell**	110	2530	-	1.5×10^4	[63]
CoFe$_2$O$_4$@ Fe$_3$O$_4$	15	**Spherical/ Core-shell**	108	2530	-	2.0×10^4	[63]
MnFe$_2$O$_4$@ CoFe$_2$O$_4$	15	**Spherical/ Core-shell**	105	11,600	-	1.7×10^4	[63]
Fe$_3$O$_4$@ CoFe$_2$O$_4$	15	**Spherical/ Core-shell**	105	11,600	-	1.8×10^4	[63]
Zn$_{0.4}$Co$_{0.6}$Fe$_2$O$_4$@ CoFe$_2$O$_4$	50@5	**cubic/ Core-shell**	145	1900	0.73	-	[83]
Fe$_3$O$_4$@ FeO	19	**Spherical/ Core-shell**	Not reaching saturation	2527	-	-	[84]
Fe$_3$O$_4$@ FeO	16-23	**Cubic/ Core-shell**	40-80[c]	1200-5754[c]	-	$1.0\text{-}1.3 \times 10^4$	[84, 85]
Fe$_3$O$_4$@ FeO	24	**Octapod/ Core-shell**	Not reaching saturation	1380	-	-	[84]
Au@ Fe$_x$O$_y$	21-52	**Dimers**	28-92	280-550	0.29-0.32	6.0×10^3	[86, 87, 74]
Ag@ Fe$_3$O$_4$	120	**Nanoflowers**	56[b]	50[b]	-	-	[88]
FeO/Fe$_3$O$_4$	-	**ClustersDimers/trimers**	110[b]	583[c]	0.7[b]	-	[89]
FeO/Fe$_3$O$_4$	-	**ClustersCentrosymetric**	82[b]	520[c]	0.7[b]	-	[89]
Fe$_3$O$_4$	103	**Clusters Centrosymetric**	105[b]	135	-	-	[90]

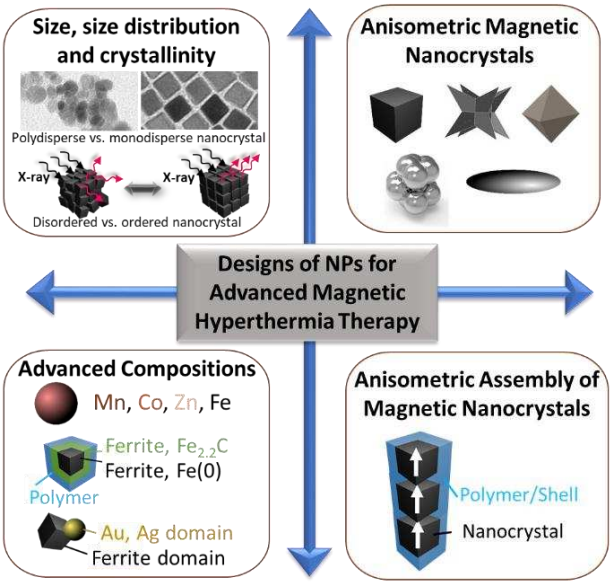

Figure 2. Design strategies of magnetic nanoparticles (MNPs) for an advanced magnetic hyperthermia therapy: anisometric MNPs, anisometric assembly of MNPs, advanced composition with high magnetization and advanced nano-heterostructures.

The design and preparation of MNPs for an optimal heat performance has been pursued by dealing with different aspects of a nanoparticle (Figure 2). This list includes the following control parameters i) its size, size distribution and crystallinity; ii) the exploitation of its anisotropic shape; iii) its chemical composition and iv) the controlled assembly of MNPs into well-defined clusters with well-defined geometrical orientation. While the first three points require the choice of synthesis conditions, the last requires skill of soft polymer or inorganic coatings for the development of assemblies based on pre-formed MNPs, as discussed later.

3.2 Size, size distribution and crystallinity

For a given magnetic nanomaterial, a major parameter to optimize the SAR is the nanomaterials's dimensions. An experimental study of this parameter (d_{opt}) requires synthesizing monodisperse NPs with a varying mean size and studying the size-dependence of SAR.[17] This is not a trivial question and indeed requires to carry out such studies with field conditions close to those found in clinics (typically 100 kHz and 16 kA/m). Mehdaoui *et al.* reported that d_{opt} is not constant but increases with the amplitude of the applied magnetic field. The authors analyzed the heating performance of a series of iron MNPs from 5 to 30 nm and found d_{opt} to be 19.7 nm for field conditions close to those used in clinics (35 kHz and 45.5 kA/m). Fortin *et al.* studied series of iron oxide and cobalt ferrite NPs with a size range of 5-17 nm and 4-10 nm, respectively.[17] Interestingly, the authors investigated the heating mechanism by which each size is releasing heatNéel in both water and glycerol (η ranged from 0.75-335 $x10^{-3}$ PI) and the heating performance (measured under AMF whose amplitude was 24.8 kA/m and frequencies from 100 kHz to 1 MHz).[91] The authors concluded that the loss process is governed by Néel relaxation for maghemite MNPs with diameters below 16 nm in water and 19 nm in glycerol, and below 7.5 and 9 nm, respectively, for cobalt ferrite MNPs, and found d_{opt} to be 16-14 nm for iron oxide and 6-5 nm for cobalt ferrite. For larger diameters, losses are mainly due to Brownian relaxation. This concept is key for the real application of MNPs in complex media like the tumor microenvironment.[91, 92] This study also commented on the importance of size distribution. The authors used a theoretical model of the heating power of single-crystal MNPs and likewise predicted a sharp maximum for a well-defined diameter (at a given frequency) and a rapid decrease of the SLP when the particle size differs by only one nanometer with respect to the ideal size, in agreement with other authors from literature.[93] By doing size-sorting of a polydisperse sample, as will be described below, it is possible to increase the heat performance of a sample up to 3 orders of magnitude. G. Salas *et al.* also reported that the size distribution affects the M_s and thus in turn the SAR values, obtaining superior heat performance for the sample with higher monodispersity.[94] The last parameter considered is the crystallinity. For MHT purposes, it was reported that it is important to avoid crystal defects even in homogeneous samples. Levy *et al*. studied a series of highly monodisperse iron oxide MNPs with increasing size prepared by seeded-growth and detected big discrepancy between the crystal volume and the effective magnetic volume of the MNPs, which had a negative impact on the SAR values. The presence of surface and internal defects (i.e. antiphase boundaries) within the MNPs provided a lower crystallinity and a magnetic disorder layer at the interface between the seed and the growing nanocrystal layer. Therefore, the use of seed grow method to produce bigger nanocrystals starting from small seeds was discourage for MHT applications.[5] S. Kubickova went further in this matter and reported that for large MNPs (d > 7 nm) internal structural disorder affects spin canting on the MNPs surface and thus the M_s, which indeed would decrease the SAR values.[95] These three parameters (size, size distribution and crystallinity) are strictly linked to the synthesis protocol used for their preparation and can easily degrade their magnetic performance. Therefore, next we describe the different synthesis

routes to prepare MNPs and review the advantages/disadvantages of each one, comparing the heating performance of the MNPs associated to each route.

Several criteria can be used for grouping the preparation routes of MNPs. Indeed, they can be grouped by the approach used (bottom-up versus top-down), the nature of the process, i.e. physical or chemical, etc. In case of the synthesis of MNPs for MHT, the methods commonly used are based on wet chemistry (a chemical process carried out in a liquid), and more specifically on sol-gel processes, in which the formation of an inorganic colloidal suspension (sol) takes place, followed by a gelation of such sol in a continuous liquid phase (gel). Considering the main solvent in which MNPs are delivered, sol-gel processes can be either hydrolytic or non-hydrolytic.

3.3 Hydrolytic methods for the synthesis of MNPs. It was in 1960 when Prof. Egon Matijević and Prof. Tadao Sugimoto set the basis for the colloidal synthesis of monodisperse iron oxide nanoparticles.[96] For the synthesis of MNPs (magnetite or maghemite phases), the most commonly adopted hydrolytic routes include the chemical co-precipitation of metal salts M(II) and M(III); and the oxidative precipitation of M(II) salts[58](Figure 3a,b). Chemical co-precipitation of ferrites was first reported by R. Massart *et al*.[97] A typical chemical co-precipitation reaction starts by dissolving metal salts (iron chloride, iron nitrate, iron sulfate, etc.) into a mixture of water/alcohol. With the addition of a strong base like NaOH, some insoluble species (iron II and III hydroxide) precipitate out of the solution at supersaturation and evolve into Fe_3O_4.Thus, the overall reaction can be described as $2Fe^{3+} + Fe^{2+} \rightarrow 2Fe(OH)_3 + Fe(OH)_2 \rightarrow Fe_3O_4 + 4H_2O$. The size of the MNPs can be varied by changing the temperature, time and pH.[98, 99] The study of the growth mechanism/kinetic evolution in this case is not trivial. However, it is now known that the main stages of this synthesis involve the deprotonation of the water (occurring due to the solvation of the cation), hydrolysis (forming the metal hydroxide complexes, M-OH) and condensation (forming M-O-M polymeric frameworks), finally evolving to the final $M_xFe_{3-x}O_4$.[100]

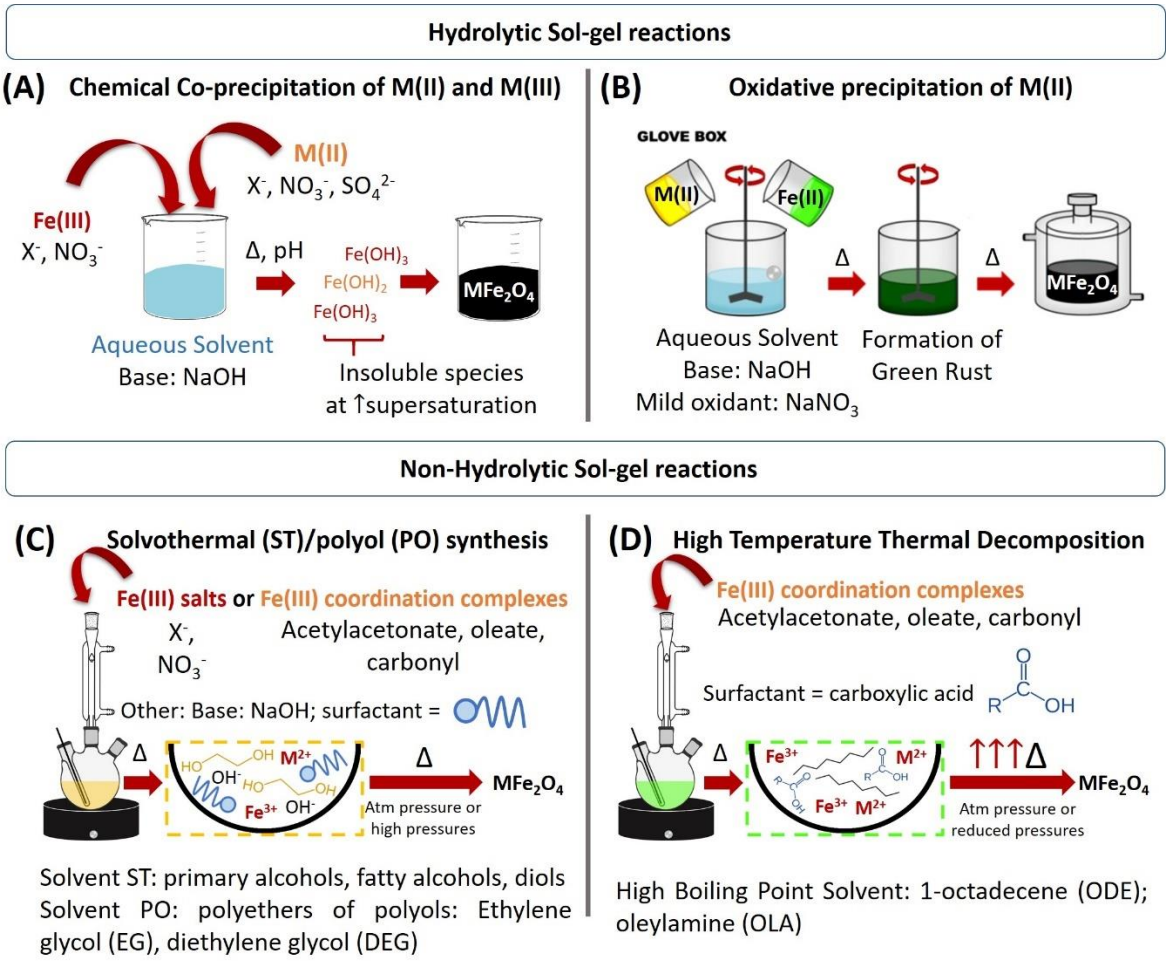

Figure 3. Chemical approach for the synthesis of MNPs through sol-gel colloidal methods: (a) Hydrolytic chemical co-precipitation; (b) Hydrolytic oxidative precipitation; (c) Non-hydrolytic solvothermal/polyol synthesis; (d) Non-hydrolytic high temperature decomposition of organic precursors. R stands for a portion of a complete molecule (not necessarily a free radical) containing carbon and hydrogen atoms, such as a methyl group.

Recently, A. P. LaGrow studied the growth mechanism in the co-precipitation of iron oxide nanoparticles[101] with the aid of synchrotron X-Ray diffraction in solution. Using this route, the kinetic growth of the particles is so fast that the particle size increases quickly (within the first 5-10 minutes), as well as the size distribution. These MNPs showed also low crystallinity, which is reflected in poor M_s values (4-11 nm MNPs have values of M_s of 40-70 emu.g^{-1} at room temperature).[102, 103] and, in turn, poor SAR values (for a size range 8 - 20 nm SAR values correspond to 10-52 Wg^{-1}). We could compare such SAR values to that of Resovist®, which although it is now discontinued (only available from the Japanese distributor), it was approved in 2001 in Europe for clinical use in MRI and it has is still widely used in MPI studies and as a reference in comparative studies of MNP proposed for MHT. As such, co-precipitation route can offer MNPs with similar SAR values. On the other hand, this route offers the possibility to easily scale up the mass of nanomaterial obtained per batch. This is one of the reasons why most of the commercially available MNPs are synthesized by hydrolytic methods.[104, 105]

The other common hydrolytic route that has been developed to a lesser extent for MHT, is oxidative precipitation. In this case, the partial oxidation of Fe(II)/M(II) salts (where M could be a transition metal like Co, Ni, Cu, Zn, etc.) in alkaline media (NaOH) occurs thanks to a mild oxidant, like $NaNO_3$, present in the solution (Figure 3b).[106] An intermediate phase (the green rust) is formed owing to the presence of the base and undergoes dehydroxylation steps leading to the formation of magnetite. The overall synthesis involves these three reactions: 3 $FeCl_2$ + 6 NaOH → 3 $Fe(OH)_2$ + 6 NaCl; 2 $Fe(OH)_2$ + 0.5 O_2 → 2 FeOOH + H_2O; 2 FeOOH + $Fe(OH)_2$ → Fe_3O_4+ 2 H_2O.[107] Vergés *et al.* reported nanoparticles with a diameter around the monodomain-multidomain limit.[108] The selection of the oxidant, iron concentration, pH and the temperature leads to MNPs having cubic/octahedral shape in a size range of 20-200 nm with higher crystallinity and higher saturation magnetization values (85 emu/g at 250 K)[109] than those obtained with other hydrolytic routes. Although oxidative precipitation slightly improves the heating performances of MNPs, as it allows a better control of shape and crystallinity, size distribution is still an issue. As standard co-precipitation, it offers a gram scale batch of MNPs (around 20 g).[109] However, this route requires oxygen-free atmospheres. MNPs with a size range of 22-34 nm have SAR values of 95-170 Wg^{-1} (10-35 kA/m and 70-249 kHz, keeping in all cases a safe H×*f* product of 2.45 x10^9 A/ms).

Methods often used in order to improve the monodispersity and decrease the standard deviation of a MNP sample prepared by hydrolytic routes are those of size-sorting, including ultracentrifugation, microfiltration, size exclusion chromatography,[91, 110, 111] static magnetic fractionation[112] or asymmetric flow field–flow fractionation.[113, 114] Fortin *et al.* demonstrated that by the size sorting of a sample of 7.1 nm and σ of 0.37, it is possible to obtain different fractions of MNPs (from 5 to 10 nm and an improved σ of 0.1-0.2). Indeed, some fractions displayed up to a 2-fold increase in the SAR, in comparison to the non-sorted original MNPs.[91] Similarly, other authors have demonstrated that size-sorting significantly helped to optimize MNP for different biomedical applications, like MRI and MPI.[110, 115] Therefore, the applicability of MNPs prepared by hydrolytic methods requires a size-sorting process which usually is time-consuming, costly and reduces the yield of the fraction of MNP material that can be used. This is the reason why the research in the field of synthesis of MNPs for an optimized MHT is mostly focused on non-hydrolytic methods.

***3.4 Non-hydrolytic methods for the synthesis of MNPs*.** In contrast to hydrolytic processes, non-hydrolytic routes use alkyl oxygen derivatives, i.e. ethers, alcohols, carboxylates, carboxylic acids etc., rather than water as oxygen donors to react with iron and form iron oxide, which frequently act as solvent and/or surfactant of the reaction to stabilize the iron-based species in solution.[116] Two main non-hydrolytic routes of synthesis of MNPs are available: solvothermal syntheses and the thermal decomposition of organic precursors (Figure 3c&d). Solvothermal synthesis uses alcohols as solvents, namely ethanol, 1-octanol, 1 2-hexanediol or polyols such as ethylene glycol (EG) and diethylene glycol (DEG).[107] The metal precursors include either the metal salts (i.e. iron chlorides, iron nitrate) or metal-coordination complexes (iron-acetylacetonates/acetates, iron- oleates or iron- carbonyl). This synthesis frequently uses surfactants, which can have very different nature, from water-soluble polymers (i.e. polyvinylpyrrolidone, PVP, sodium carbonate, etc.), or organic molecules (oleic acid, oleylamine, etc.), to surfactants with a hydrophobic tail, depending on the polarity of the chosen alcohol.[117] To decompose the metal precursors, the reaction takes place at temperatures well above 100 °C and they can occur at atmospheric pressure or, as in the case of solvothermal reaction, frequently at high pressure through the use of pressurized vessels (Figure 3c). Few significant works delve into the mechanism of formation of MNPs using solvothermal routes.[118, 119] Niederberguer *et al.* demonstrated that alcoholic solvents undergo a solvolysis reaction to form iron enolate by coordinating and partially reducing Fe(III) to Fe(II) and providing the

correct stoichiometry of Fe_3O_4.[118] Solvothermal synthesis provides MNPs in a broad range of sizes, shapes, and a variable crystallinity depending on the experimental conditions. Among the most promising results for MHT are MNPs in the size range of 6-38 nm, having SAR values of 40-500 Wg^{-1}(considering only safe conditions of AMF with an H*xf* product below $5x10^9$ A/ms) that corresponds to an improvement in the SAR of about 20 times in comparison with Resovist®, as first demonstrated by Lartigue *et al.* using a solvothermal polyol method.[81] Moreover, MNPs prepared by solvothermal method could be directly transferred to water upon an acidic treatment, rendering this synthesis route straightforward for MHT. The main disadvantage of this particular synthesis route is that it is often related to a production of MNPs oftens of milligrams. In addition, the solubility of MNPs depends critically on the surfactants used during the synthesis, frequently needing to further process the MNPs.[81]

In the case of thermal decomposition (TD) approach, the solvent of the reaction is still an organic molecule which has a high boiling temperature and that stays inert to temperatures that are high enough to enable the metal precursor to decompose (frequently well above 200 °C). In this case, the solvent is not necessarily involved in the reaction.[107] Frequent solvents used in TD reactions of MNPs are 1-octadecene,[120] benzyl ether,[121] phenyl ether, octylether, dioctyl ether and squalane.[72] The usual metal precursors for iron oxide MNP synthesis are iron acetylacetonates, oleates or carbonyls. The control of the MNPs' size, shape and aggregation, depends on the number of nuclei generated in the first nucleation stage and on the crucial presence of surfactants that chemisorbed on the ionic species, nuclei and growing crystals facilitating the nanoparticle growth process.[94] Often, some of the surfactants having specific high-affinity for some of the facets of the nanocrystal impair the growth along some well-defined crystal directions thus facilitating the growth along the surfactant-free (naked) crystal facets. The most usual surfactants for the synthesis of MNPs are oleic acid, decanoic acid, trioctylphosphine oxide (TOPO), trimethylamine oxide, oleylamine, hexadecylamine, or quaternary ammonium salts.[122-124] The TD reaction are frequently conducted either at atmospheric pressure or under reduced pressure (mBar pressure generated in an argon- vacuum lines, i.e. Schlenk line).

The elucidation of the reaction mechanism behind high temperature TD process is still a matter of study and is strictly related to the reaction mixture components. The oxidative decarboxylation of iron oleate was first proposed by Kwon *et al.,* who determined through gas chromatography that carbon dioxide and hydrogen are generated during the heating of iron oleate.[125] Scott J. Kemp *et al.* proposed that the thermolysis of the metal carboxylate precursor and its reduction, from iron(III) to iron(II) (both species necessary to form Fe_3O_4), occurs simultaneously in the heat-up stage by two possible reduction mechanisms,: i) the oxidative decarboxylation of iron oleate and ii) the oxidation of 1-octadecene. In a more recent study, it was demonstrated that the breaking of the metal precursor leads to the formation of radical species, which can recombine or decompose into smaller molecules, or react with other metal carboxylate molecules to propagate the decomposition reaction.[119] Interestingly, Gonzales-Weimuller M *et al.* also determined that the air-free thermolysis of iron(III) oleate favors formation of wüstite (FeO)[126] and not magnetite, as reported by Chen *et al*.[127] The mechanism of decomposition of other iron precursors, i.e. iron pentacarbonyl, has been studied occurring with the release of CO, followed by the formation of iron oleate complex, and its further thermolysis.[128] It is still unclear at which temperature iron oleate, formed in-situ after the thermolysis of iron pentacarbonyl, decomposes.[129, 130] Recent studies suggest that the decomposition temperature of the iron oleate complex can be different than that of iron oleate synthesized ex-situ.[129]

Thanks to the high temperature reaction as well as the use of surfactants, which control the reactivity of iron and other transition metals used in these non-hydrolytic routes, an overall control in the

reaction kinetics can be pursued allowing a fine control over crystallinity, size, size distribution and shape of MNPs in comparison to hydrolytic routes. In particular, this non-hydrolytic method offers the possibility of tuning several experimental conditions, including the suitable choice of precursors, solvent, stabilizer molecules, adjustment of their relative concentration ratio in the liquid phase, the application of a temperature ramp (in order to separate the stage of nanocrystal nucleation from the growth of the nanocrystals), providing an unprecedented control over the structural and magnetic parameters of MNPs. This is indeed reflected in better SAR values, ranging from 70 to 650 Wg^{-1} for MNPs with a size range of 5-35 nm (considering only safe H*x*f product below $5x10^9$ A/ms).[72, 131] In general, this method is likewise limited by the low amount of nanomaterial obtained per batch (in the range of milligrams) and the overall difficulties to scale up the production. Moreover, the need to water transfer the MNPs once produced in the apolar solvents makes the overall protocol more complex and expensive.

3.5 Comparison of SAR of MNP obtained by classical hydrolytic and non-hydrolytic sol-gel colloidal routes. The comparison of the SAR values of MNPs obtained by classical hydrolytic or non-hydrolytic routes although complicated by the different measurement conditions (different H, *f* and H*x*f product) reflects the importance of choosing the most proper synthetic route depending on the specific application of MHT. We attempt to plot the SAR values with respect to the synthesis routes by considering the highest SAR value reported in literature for each type of synthesis and plot the H*x*f product at which each system was characterized, highlighting where both H*x*f biological limit and the H*x*f reported for the clinics are (Figure 4). As shown, SAR values of iron oxide MNPs obtained by hydrolytic methods (yellow), thermal decomposition (pink) and solvothermal (purple) were compared to Resovist® (Bayer Pharma AG.[132, 133] Considering only safe conditions of field (H*x*f product below $5x10^9$ A/ms), SAR magnitude can be ordered with respect to the preparation route as follows: $SAR_{Thermal\text{-}decomposition}$ (650 Wg^{-1}) >$SAR_{Solvothermal}$(500 Wg^{-1}) >$SAR_{Hydrolytic}$(370 Wg^{-1}), and even the last one very much exceeds the heating performance of Resovist® (Figure 4 and see also the Table 3 for more detail). In general, MNPs produced by hydrolytic methods do not offer a significantly relevant improvement of the SAR with respect to Resovist® and TD stands out as the most promising route for MHT. However, although there is an example of large-scale production of MNPs using TD method,[130] their hyperthermia performances were not considered (the aim of this work was different). Therefore, in this direction, there is plenty of room to improve the hydrolytic/non-hydrolytic routes to obtain scaled production of MNPs optimized for MHT.

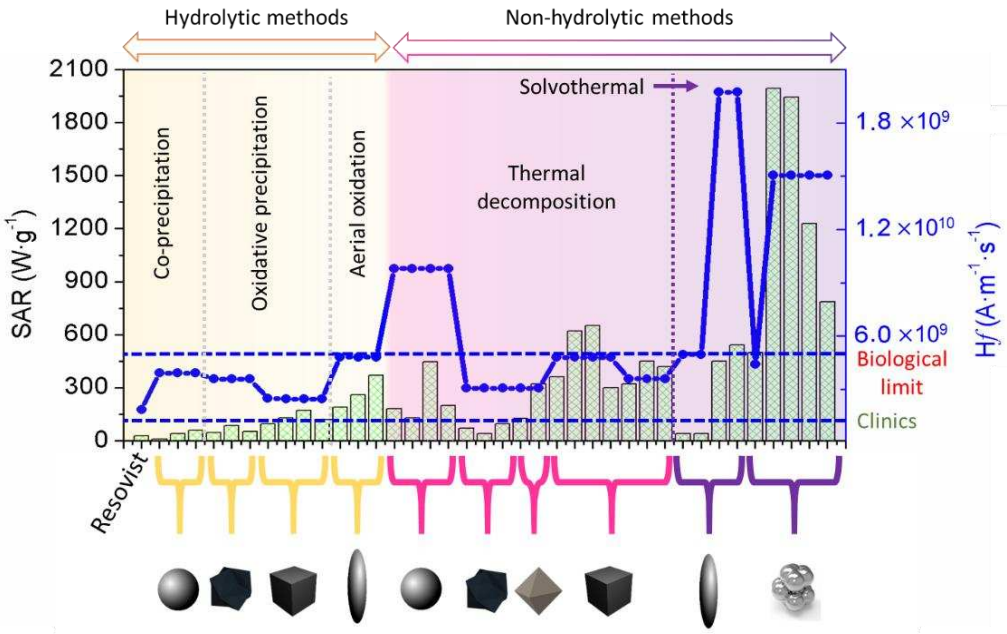

Figure 4. SAR values of iron oxide MNPs summarized in Table 3, which were obtained by different synthetic approaches: hydrolytic methods (yellow), thermal decomposition (pink) and solvothermal (purple). Besides traditional spherical MNPs, SAR of different shaped-MNPs are also included. On the right Y-axes (blue) the H*xf* product associated to each SAR determination is shown. Dashed Blue lines indicate the H*xf* used in clinics and the H*xf* limit for biological acceptance. As plotted for some MNPs, SAR values have been measured at H*xf* values above the biological limit.

Table 3 Heating performance represented by the SAR values of iron oxide MNPs synthesized by different colloidal synthesis methods.

Synthesis method	Size (short axis) (nm)	Volume (nm^3)	Shape	**SAR (W/g)**	H (kA/m)	f (kHz)	Hf (A/ms)	ILP (nHm^2/kg)	Ref
Co-precipitation	20	4.189×10^3	Resovist	**26.8**	3.1	600	1.86×10^9	3.1	[54]
Co-precipitation	8	2.681×10^2	Spherical	**10**	7.5	522.7	3.92×10^9	0.34	[12]
Co-precipitation	11	6.969×10^2	Spherical	**40**	7.5	522.7	3.92×10^9	1.36	[12]
Co-precipitation	13	1.150×10^3	Spherical	**58**	7.5	522.7	3.92×10^9	1.98	[12]
Co-precipitation	13	2.197×10^3	Faceted	**47**	11.93	300	3.58×10^9	1.10	[134]
Co-precipitation	18	5.832×10^3	Faceted	**87**	11.93	300	3.58×10^9	2.04	[134]
Co-precipitation	20	8.000×10^3	Faceted	**52**	11.93	300	3.58×10^9	1.22	[134]
oxidative precipitation	33	3.594×10^3	Cubic	**95**	10	249	2.49×10^9	3.82	[108]
oxidative precipitation	22	1.065×10^4	Cubic	**130**	35	70	2.45×10^9	1.52	[109]
oxidative precipitation	26	1.758×10^4	Cubic	**170**	35	70	2.45×10^9	1.98	[109]
oxidative precipitation	34	3.930×10^4	Cubic	**120**	35	70	2.45×10^9	1.40	[109]
aerial oxidation + reduction	26 x 98	6.123×10^4	Elongated	**190**	43.76	109.8	4.80×10^9	0.90	[135]
aerial oxidation + reduction	25 x 95	5.579×10^4	Elongated	**260**	43.76	109.8	4.80×10^9	1.24	[135]
aerial oxidation + reduction	16 x 87	1.964×10^4	Elongated	**370**	43.76	109.8	4.80×10^9	1.76	[135]
Thermal decomposition	5	6.545×10^1	Spherical	**180**	24.5	400	9.80×10^9	0.75	[126]

Thermal decomposition	10	5.236×10^{2}	Spherical	**130**	24.5	400	9.80×10^{9}	0.54	[126]
Thermal decomposition	14	1.437×10^{3}	Spherical	**447**	24.5	400	9.80×10^{9}	1.86	[126]
Thermal decomposition	13	1.150×10^{3}	Spherical	**200**	24.5	400	9.80×10^{9}	0.83	[126]
Thermal decomposition	14	2.744×10^{3}	Faceted	**70**	39.78	77	3.06×10^{9}	0.57	[94]
Thermal decomposition	18	5.832×10^{3}	Faceted	**40**	39.78	77	3.06×10^{9}	0.33	[94]
Thermal decomposition	22	1.065×10^{4}	Faceted	**95**	39.78	77	3.06×10^{9}	0.78	[94]
Thermal decomposition	18	3.055×10^{2}	Octahedral	**124**	39.78	77	3.06×10^{9}	1.02	[52]
Thermal decomposition	22	5.577×10^{2}	TruncatedOctahedra	**320**	39.78	77	3.06×10^{9}	2.63	[52]
Thermal decomposition	14	2.744×10^{3}	Cubic	**360**	16	300	4.80×10^{9}	4.69	[72]
Thermal decomposition	19	6.859×10^{3}	Cubic	**620**	16	300	4.80×10^{9}	8.07	[72]
Thermal decomposition	24	1.382×10^{4}	Cubic	**650**	16	300	4.80×10^{9}	8.46	[72]
Thermal decomposition	35	4.288×10^{4}	Cubic	**300**	16	300	4.80×10^{9}	3.91	[72]
Thermal decomposition	14	2.744×10^{3}	Cubic	**320**	12	300	3.60×10^{9}	7.41	[72]
Thermal decomposition	19	6.859×10^{3}	Cubic	**450**	12	300	3.60×10^{9}	10.42	[72]
Thermal decomposition	24	1.382×10^{4}	Cubic	**420**	12	300	3.60×10^{9}	9.72	[72]
Solvothermal	7 x 41	1.757×10^{3}	Nanorods	**40**	16	310	4.96×10^{9}	0.50	[88]
Solvothermal	6 x 65	1.951×10^{3}	Nanorods	**40**	16	310	4.96×10^{9}	0.50	[88]
Solvothermal	7 x 41	1.757×10^{3}	Nanorods	**450**	63.66	310	1.97×10^{10}	0.36	[88]
Solvothermal	6 x 65	1.951×10^{3}	Nanorods	**540**	63.66	310	1.97×10^{10}	0.43	[88]
Solvothermal	21	4.849×10^{3}	Nanoflowers	**500**	11	400	4.40×10^{9}	10.33	[136]
Solvothermal	24	7.238×10^{3}	Nanoflowers	**1992**	21.5	700	1.51×10^{10}	6.16	[136]
Solvothermal	28	1.149×10^{4}	Nanoflowers	**1944**	21.5	700	1.51×10^{10}	6.01	[136]
Solvothermal	34	2.058×10^{4}	Nanoflowers	**1230**	21.5	700	1.51×10^{10}	3.80	[136]
Solvothermal	38	2.873×10^{4}	Nanoflowers	**787**	21.5	700	1.51×10^{10}	2.43	[136]

3.6. MNPs with anisometric shape for improved MHT

To tune MHT heat performances, nanocrystal shape is another important factor to be considered. So far, non-spherical shaped MNPs were mostly obtained by non-hydrolytic methods, as only these routes enable to vary a series of reaction parameters thus allowing to control the MNP anisometry, and in turn, positively affect SAR values. Some anisometric shaped MNPs present 20-30 fold-increase in the SAR in comparison to Resovist® (Figure 4 and Table 3). In particular, when comparing different shaped MNPs, the reported SAR values indicate the following order in heat performances: $SAR_{Nanocubes}>SAR_{Nanoflowers}>SAR_{Nano-octahedra}>SAR_{Truncated\ MNPs}>SAR_{Nanorods}$, although their comparison with performances of spherical shaped MNPs is not straight forward as SAR values for poor heating nanospheres are often characterized at H*x*f product much higher than the safe region.

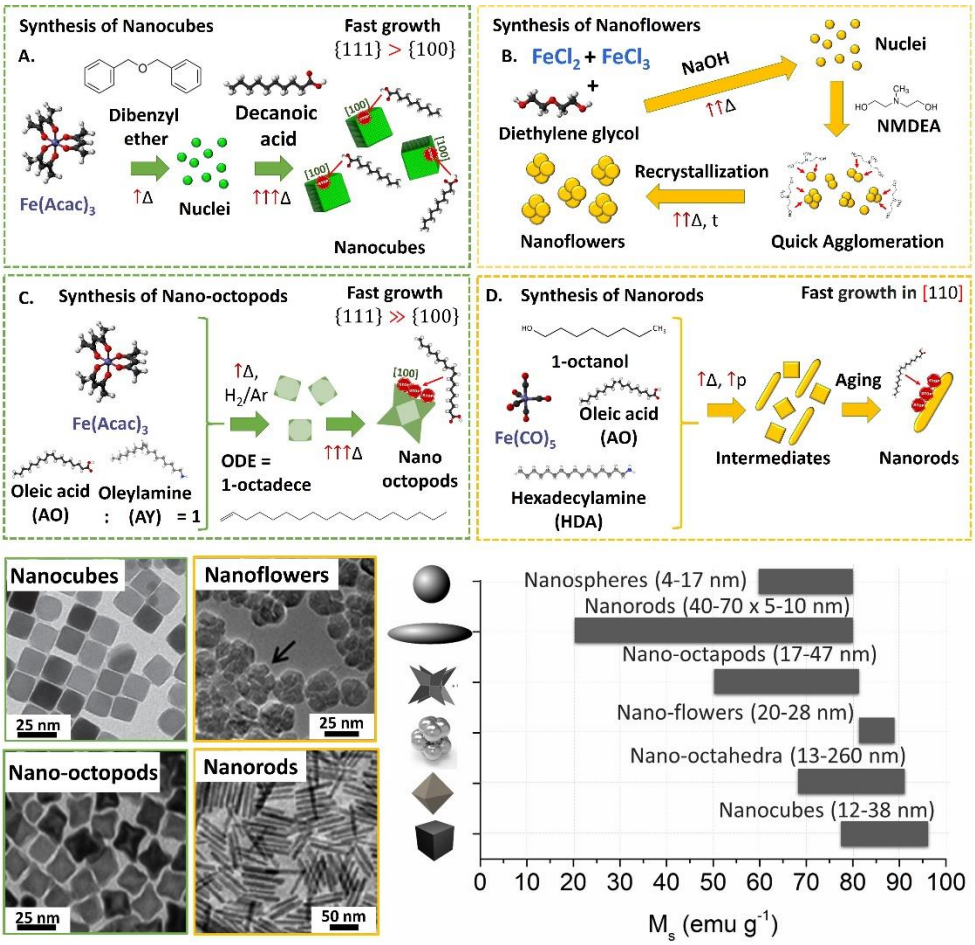

Figure 5. MNPs with anisometric shape for MHT: synthesis approaches for nanocubes (green dashed line): Reprinted with permission from[73] Copyright © 2012, by ACS Publications; nano-octopods (green dashed line): Reprinted with permission from[137] Copyright © 2016, by ACS Publications; nanoflowers (yellow dashed line): Reprinted with permission from[81] Copyright © 2012, by ACS Publications ; and nanorods (yellow dashed line): Reprinted with permission from[79] Copyright © 2016, by ACS Publications. On the right panels the saturation magnetization M_s of different MNPs with a size range for a given shape at room temperature.

To promote the shape-controlled synthesis of nanocrystals (like cubic, octopod, octahedral, rod and flower), the selection of certain ligands/stabilizers (i.e. surfactants, amines, etc.), it's molar ratio to the metal precursor, the molarity of the metal precursor and the optimization of specific experimental conditions (heating rate, temperature ramp, time, pressure, etc.) are crucial.[123] Cubic shape iron oxide MNPs were first reported by Hyeon *et al.* in 2008 at a cube edge of 20 - 160 nm and a chemical composition of magnetite.[138] The well-defined cubic shape of the MNPs was the result of fast (kinetically controlled) heat-up process of a mixture of $Fe(acac)_3$, oleic acid, and aromatic ethers, which promoted the nanocrystal growth along ⟨111⟩ directions, corresponding to nanocubes with crystal planes, similar to the those produced by magnetotactic bacteria.[139] Pellegrino *et al.* (Figure 5a) first reported the SAR characterization of magnetite nanocubes with a cube edge defined in the range of 14-35 nm.[72, 73] The authors showed that dibenzyl ether used as a solvent in the synthesis is not inert and whose thermal decomposition generates sub-products (aldehyde, benzyl alcohol and toluene), which they associated to

thermal instability but also to the cubic shape control. Moreover, by changing the relative volume ratio of the squalane to dibenzyl ether, the size of the particles could be tuned. This route has provided nanocubes with very high SAR values (360-650 Wg^{-1} for a H*x* of 4.8 $x10^9$ $Am^{-1}s^{-1}$). Later, R. Chen *et al.* further demonstrated that by introducing aromatic ethers that undergo radical decomposition during thermolysis, the electrochemical potential of the solvent environment was tuned and this parameter favored the nucleation of the ferrimagnetic phase and could obtain nearly defect-free ferrite nanoparticles.[140] The need to have an aromatic ether and a high boiling point solvent to obtain nanocubes would also support the initial finds of Hyeon *et al.,* who in order to synthesize regular iron oxide nanocubes, added 4-biphenyl carboxylic acid to dibenzyl ether, following a similar protocol.[138] Likely the dibenzyl ether thermolysis and the high boiling point (373°C) of 4-biphenyl carboxylic acid, both contribute to temperature stabilization during dibenzyl ether decomposition whose sub-products act as essential shape directing agents. Other authors,such as Ahn *et al.,*[141] attributed the cubic shape to the thermal decomposition of iron (III) oleate in the presence of other specific ligands like sodium oleate and alkaline metal reagents. The authors demonstrated a high reduction potential capability allowing magnetite phase formation of cubic shape nanoparticles at significantly lower temperatures of 200 °C (generally to form magnetite, temperatures as high as 300 °C are required). The authors proposed that this decrease of temperature is related to the reduction of acetylacetonate and acetate anions to the corresponding aldehyde and alcohol, which are the oxygen source molecules for iron oxide nucleation, in presence of the magnesium compound.[141]

An alternative to the cubic shape is the nano-octapod, which is essentially a deformed nanocube with sharper cube edges. This shape has recently attracted the attention for MHT purposes as it could generate additional local symmetry breakings, which could increase the surface anisotropy and have enhanced heating performance. Weller *et al.* reported that wüstite-magnetite nano-octopods or "star-shaped nanocrystals" (kinetically favored product) undergo a metamorphism toward cubic-shaped particles (thermodynamically favored product) thoroughly describing the chemistry and the formation mechanism of such nanoparticles. The authors use octadecene and oleic acid as solvent and surfactant, respectively, and stated that by simply diluting the reaction mixture (increasing the volume percentage of solvent), the driving force of oleic acid to block the facets of the crystal is suppressed,[142] promoting a fast nucleation of cube-shaped particles formed instead.[143] Nemati *et al.* reported the possibility to obtain nano-octopods shape, in the range of 17−47 nm, by TD synthesis (Figure 5b). The authors attributed the nano-octopod shape to the use of a mixture of stabilizers (Oleic acid/Oleylamine) at well-defined molar ratio.[137] However, the resulting octapods are composed of a mixture of wüstite /magnetite (FeO/Fe_3O_4) phases, which were oxidized to one-single phase Fe_3O_4 by annealing under an air flux. Although this is a novel shape type of MNPs for MHT, the authors reported very poor SAR values, even for the annealed samples of pure magnetite composition (60 Wg^{-1} for a H*x* of 4.9 $x10^9$ $Am^{-1}s^{-1}$), getting values very similar as those of Resovist®. In general, it can be assessed that Fe-oleate source in alkene hydrocarbon solvent (e.g.,1-octadecene) provides cubic or cubic-related shapes, however, under certain conditions, it gives rise to undesired wüstite (FeO). The decomposition to iron (II) oleate to intermediate species continuously happened during the heating-upstage and the complete decomposition of iron oleate complexes at reflux temperature under an inert environment promotes the nucleation of FeO due to reduction environment effect of alkene hydrocarbon solvent.[119] Nevertheless, the synthesized iron oxide nanoparticles can be oxidized to magnetite after exposure in the air.[130] In contrast, the reductive environment of a mixture of oleylamine and aromatic ether (e.g., dibenzyl ether) has been applied for the uniform nucleation and growth of iron oxide nanoparticles. Other shape related to cubic is the octahedral. G. Salas *et al.* reported

the synthesis of truncated octahedral and octahedral MNPs of 18-22 nm[52] by modifying the Sun route for nanocubes.[144] The author stated that the domination of octahedral over cubic shape was achieved by promoting growth rate along the <100> over the <111>, leading to crystals exhibiting the most stable {111} facet. Interestingly, spherical polyhedral shape was observed in the case of particles prepared only with Oleic acid, and the octahedral shape was obtained only in the presence of Oleic Acid/oleylamine mixtures with specific molar ratios. MNPs were transferred to water using a ligand exchange protocol with dimercaptosuccinic acid (DMSA), resulting in acceptable values of SAR (124-320W.g^{-1} for a H×*f* of 3 x10^9 $Am^{-1}s^{-1}$),[94] which supposes an improvement in contrast to Resovist®. Finally, A. Shavel *et al.* reported the synthesis of highly monodisperse octahedral MNPs and attributed the shape control to the ligand trioctylammonium bromide (TOAHB) in the process of thermal decomposition of iron oleate.[145]

On the other hand, other non-hydrolytic routes like polyol-based solvothermal methods have been used to synthesize nanoflowers and nanorods, respectively. Lartigue *et al.* reported the SAR characterization of iron oxide nanoflowers, obtained by modifying the nanoflower recipe initially reported by Caruntu *et al.*[146] (Figure 5c). In this synthesis in diethylene glycol, a mixture of $FeCl_2$/$FeCl_3$ was annealed in the presence of N-Methyldiethanolamine (NMDEA) and NaOH. Caruntu *et al.* reported that this reaction starts with the formation of chelate metal alkoxide DEG complexes followed by the hydrolysis at elevated temperature to generate the nuclei, which thanks to high viscosity of NMDEA, slows down the hydrolysis of the metal alkoxide complexes, forcing the aggregation of the nuclei. At prolonged reaction time and high temperature, recrystallization occurs and the nanoflowers are formed. They can be easily transferred to water using an acid treatment and upon a size-exclusion chromatography (SEC) size-sorting process, the resulting nanoflowers reached values of SAR (for a sample of 21 nm in diameter) significantly higher than Resovist® (500 W.g^{-1} for a H×*f* of 4.4 x10^9 $Am^{-1}s^{-1}$). R. Das *et al.* reported iron oxide nanorods with short-axis size of 5-6 nm and longest axis of 40-70 nm (Figure 5d).[79] The intermediates of the reaction are wüstite cubes and nanorods, which at high temperatures quickly evolve to iron oxide nanorods. Indeed, this route was developed by Sun H. *et al.*,[80] hypothesizing that the elongated shape was due to a reaction between the surfactant and the base (Oleic acid and hexadecylamine), forming small quantities of water. Indeed, the authors demonstrated that either the initial addition of water or the use of small quantities of a strong acid (like HCl) was associated to MNPs elongated shape, thus hypothesizing that these experimental conditions promote the growth in the [100] direction. It was possible to easily transfer such elongated MNPs with tetramethylammonium hydroxide however, this shape leads to MNPs with poor SAR values when considered safe MH conditions (40 Wg^{-1} for a H*f* of 5 x10^9 $Am^{-1}s^{-1}$),[79] getting values very similar as those of Resovist®. This surprising low SAR values may be attributed to the presence of other crystal phases (for example hematite or goethite) in the sample (along with the desired magnetite/maghemite), which are less performing than magnetite/maghemite in MHT. Avolio *et al*.[135] reported a hydrolytic route for the synthesis of elongated nanoparticles involving the following steps: i) aerial oxidation to obtain goethite elongated NPs, ii) silica coating to preserve the shape, iii) chemical reduction of goethite to magnetite. Such post-synthetic reduction treatment at high temperatures yielded to elongated mono-crystals of highly pure magnetite (the percentage of maghemite was below 5%, thanks to the inorganic silica coating, preventing the oxidation of the samples),[147] showing, in the case of MNPs whose shortest axis was 16-26 nm, SAR values of 190-370 Wg^{-1}.[135] This supposes an improvement in the SAR of ca. 15 times in comparison with Resovist®, and exceeds the performances so far obtained for this shape using the non-hydrolytic route reported by R. Das. Indeed, shapes with highest M_s (nanoflowers, nano-octahedra and nanocubes) have proven to have higher SAR than spherical MNPs while it is surprising that nanorods and nano-octopods have such low values of SAR (Figure 5 and table 3). In general, cubic-

shaped MNPs display higher M_s values in comparison with regular spherical-shaped MNPs due to a combination of different effects such as lower surface spin disorder, higher crystallinity, and higher magnetic moments.[148] In fact, the magnetic spin states was simulated for nanocubes and nanospheres of the same volume and the outcomes reveal different degree of spin canting against external magnetic field (B_0). Cube exhibits lower spin disorder rate (4%) than spheres (8%).[83] For nanorods and nano-octapods despites the synthetic approaches offer a great control over the shape and size distribution, it may be possible that the control over the phase composition is not optimal, and some intermediate FeO phase impurities may decrease M_s, explaining such low SAR values.

For spherical MNPs, despite their broad application in several preclinical MHT studies, their heat performances are surely not the highest if compared to iron oxide MNPs of other shapes as the nanocubes. Moreover, preclinical biodistribution studies with iron oxide nanocubes have proven their safety and their efficacy as MHT heat mediators[74, 149] in xenograft murine tumor model. For these studies, the intratumoral injections of milligram amounts of MNPs dose (as low as 0.7 mg Fe) and the exposure to clinical AMF treatment (10-24 kA/m and 110 kHz for 600-900 s) successfully led to therapeutic temperature increase (42-45°C),and the delay of the tumor growth.[150, 151]

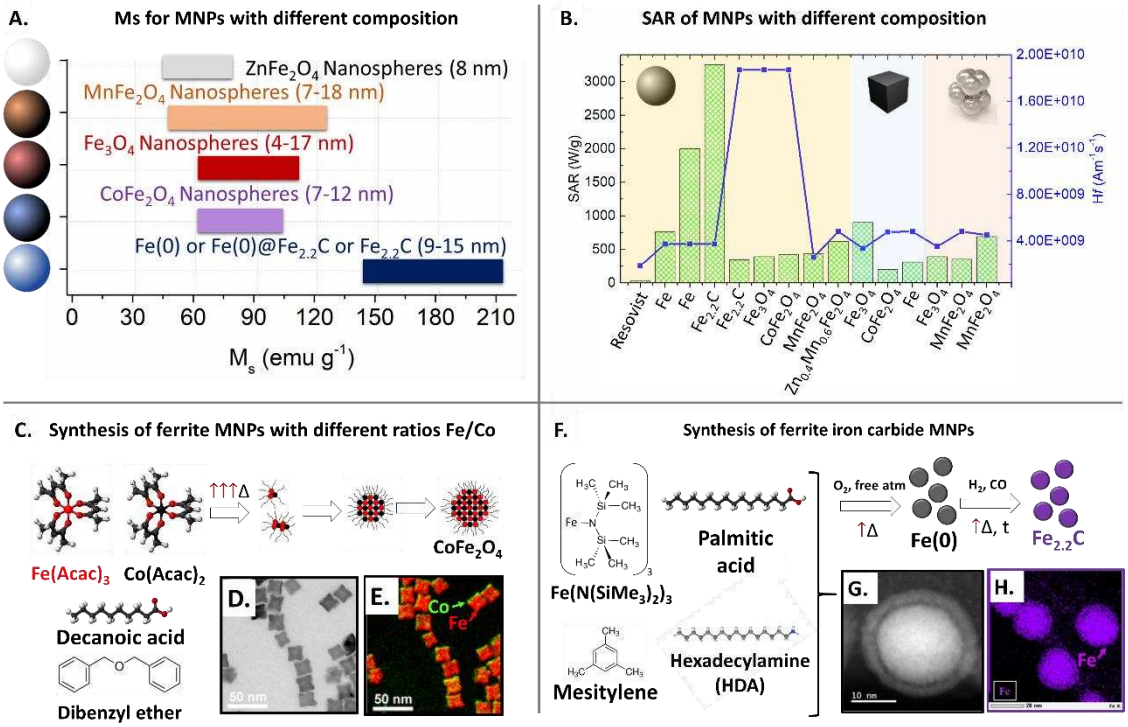

Figure 6. MNPs with tuned composition for MHT: (a) Saturation magnetization Ms of spherical nanoparticles with different composition (M_s values are taken from Table 2); (b) SAR values as a function of H×*f* product for MNPs with different composition and shape. SAR data available in Table 4; Selected examples of chemical approaches developed to tune the MNPs composition for (c) synthesis of cobalt ferrite nanocubes involving the thermal decomposition or iron and cobalt organic precursors in the presence of decanoic acid and dibenzyl ether; (d-e) micrographs showing the cubic shape and the elemental mapping of Fe (red) and Co (green). Reprinted with permission from[75], Copyright © 2016, by

ACS Publications; (f) synthesis of iron and iron carbide spherical nanoparticles involving the decomposition, in an inert oxygen free atmosphere, of an iron organic precursor; (g-h) micrographs showing the metallic iron core and iron oxide shell, along with the elemental mapping showing the Fe (purple). Reprinted with permission from[152], Copyright © 2019, by ACS Publications.

3.7. Advanced compositions for improved MHT

The doping of iron oxide ferrite MNPs with different transition metals with controlled distribution of cation among the crystalline structure is another smart strategy used to tune the magnetic properties of MNPs. Mixed metal ferrites described as MFe_2O_4, where M represents usually any divalent transition metal ions, display a spinel structure. This structure is a face-centered cubic arrangement of oxygen atoms and M^{2+} and Fe^{3+} occupying either tetrahedral or octahedral sites. The possibility to improve the SAR by tuning the composition of ferrites is related to i) the chosen cations as, indeed, each transition-metal atom has a characteristic magnetic moment and ii) the presence of vacancies. Both hydrolytic and non-hydrolytic routes were employed to obtain metal ferrites by the addition of the desired metal precursors: from chemical co-precipitation,[153] oxidative precipitation,[154] aerial oxidation[155] to thermal decomposition[156, 157] and polyol method.[158] The successful doping for MHT purposes has pointed to Mn, Zn and Co bivalent ion doping. In few studies, other elements like Bi and Gd were assessed but the reported SAR values were lower in comparison to those offered by iron oxide. Apart from spinels, other compositions were successfully exploited recently for MHT, and among them, metallic Fe NPs (α-Fe), whose crystal structure is cubic close-packed or iron-carbon alloys such as Fe carbide NPs, (ε'-$Fe_{2.2}C$), whose crystal structure is hexagonal close-packed,[71] both of which exhibit conveniently a soft ferromagnetic behavior. Other alloys, such as Fe-Co,[159] Ni-Cu[160] and Fe-Ni-Co,[161] were also developed and studied for their SAR characterization but they have shown poor SAR values and also at field conditions far from the biological acceptable values. Instead, iron and iron carbide nanospheres,[71] $Co_{0.7}Fe_{2.3}O_4$nanocubes[75, 83] and $Mn_{0.7}Fe_{2.3}O_4$ nanoflowers[162] obtained through non-hydrolytic methods were showing better SAR values in water and thus heat performance than the corresponding iron oxide MNPs at the same size and shape (Figure 6b). This may be related to the Ms values of these new metal and metal alloys composition. Indeed, if we compare spherical MNPs, while M_s for all the different ferrites (Zn, Co, Mn and iron oxide) is assessed below 120 emu.g^{-1}, for Fe(0), Fe(0)@$Fe_{2.2}C$ or $Fe_{2.2}C$ the M_s values are well above the ferrites values (Figure 6a), displaying values in the range of 160-210 emug^{-1} ($M_{s,\ Fe(0)}$>$M_{s,\ Fe(0)@\ Fe2.2C}$>$M_{s,\ Fe2.2C}$).This is indeed reflected in the comparative SAR values (Figure 6b). The synthetic approach to synthesize MNPs metal and metal alloys compositions, was pioneered by Chaudret *et al*.[70] In these routes, the thermal decomposition of $\{Fe[N(SiMe_3)_2]_2\}_2$ in presence of hexadecylamine and palmitic acid (PA) occurred in mesitylene under a hydrogen atmosphere at 150 °C. After the formation and nucleation of Fe(0), the iron carbide shell is formed through a carbidization process which, depending on the duration of the process, provides a shell thickness that was found to be critical in the composition/structure of the final samples. Bordet *et al.* recently investigated the water-transfer with a wide variety of dopamine-based ligands and found that when iron carbide nanoparticles are exposed to air once in water, they are partially oxidized to iron oxide and M_s decreased from 160 emu×g^{-1} to 100 emu×g^{-1}, in accordance with the formation of a shell of iron oxide of 2-3 nm [152]. This phase transformation, in turn, affects heating values: indeed the SAR values of initial Fe(0) MNPs of 15 nm are 700 W×g^{-1} and those of $Fe_{2.2}C$ are exceedingly higher, 3250 W×g^{-1} (H×*f* of 3.7 x10^9 $Am^{-1}s^{-1}$ in both cases) and upon oxidation of iron carbide MNPs to magnetite on the shell, the SAR decreases to 1000 W×g^{-1} (H×*f* of 3.7 x10^9 $Am^{-1}s^{-1}$) after 4 months in water. Despite the oxidation, these SAR values are at least 40-fold higher

than Resovist® and, importantly, under safe MHT conditions. In addition, their ability to undergo surface oxidation suggests that the Fe core could be slowly converted to iron oxide which in turn, can be degraded by liver cells in vivo, as already shown by other groups.[163] Among the MNPs of spherical shape and diverse mixed ferrite, Jang *et al.* reported SAR values of 432 Wg^{-1} (for a H*x*f of 2.6 x10^9 $Am^{-1}s^{-1}$) for 15 nm $Zn_{0.4}Mn_{0.6}Fe_2O_4$, which are nearly 20-fold more efficient than Resovist®.[76]

With respect to mixed ferrites having other nanoparticle shapes, such as cubic shape, the introduction of Co ions within MNPs was leading to the highest SAR increase in comparison to its corresponding iron oxide counterpart. Sathya *et al.* successfully synthesized cobalt ferrite nanoparticles by a non-hydrolytic route controlling either the cube edge in the range 14-27 nm nanocubes and the cobalt stoichiometry in the range from 0.1 to 0.7.[75] The approach is based on the addition of a mixture of $Fe(Acac)_3$ and $Co(Acac)_2$ rather than just the iron precursors (Figure 6c). Samples of 17-19 nm had 880-900 Wg^{-1} (for a H*x*f of 3.36 x10^9 $Am^{-1}s^{-1}$), higher than iron oxide nanocubes of similar volume (a sample of 19 nm had 620 Wg^{-1} for a H*x*f of 4.8 x10^9 $Am^{-1}s^{-1}$), and having a nearly 40-fold increase in SAR of Resovist®. It is striking that metallic iron NPs of cubic shape display SAR values that are lower than any other composition for the cubic shape (Figure 6b).[77] This surprising SAR data for Fe cubic shape MNPs may be related to a worse colloidal stability due to stronger magnetic interparticle interactions, which destabilize the samples. Lastly, for mixed ferrite nanoflowers synthesized *via* TD method , the highest SAR value was reported for those doped with Mn,[162] achieving SAR values as high as 689 Wg^{-1} (for nanoflowers of 19 nm and for a H*f* of 4.5 x10^9 $Am^{-1}s^{-1}$), which is higher than that measured for magnetite nanoflowers (21 nm) produced by the polyol method (300-500 Wg^{-1} for H*f* of 3.5-4.4 x10^9 $Am^{-1}s^{-1}$). Lastly, Casula *et al.* reported 57 nm Mn-doped nanoflowers synthesized through the polyol method.[164] The maximum SAR value recorded was 350 Wg^{-1} (for a H*x*f of 4.8 x10^9 $Am^{-1}s^{-1}$). In summary, we can conclude that SAR values of iron oxide ferrites can be further increased by tuning the composition of MNPs, by choosing as dopants such as Co, Mn or mixed Mn and Zn ferrite. Iron and iron carbide MNPs have unprecedented SAR values at low H*x*f products, demonstrating the great potential of this composition. All plotted SAR values are gathered in Table 4.

Whilst only iron oxide formulation has been so far assessed in MHT clinical trials, some of the presented chemical compositions have already given promising results in pre-clinical studies. The therapeutic effect of Zn-ferrite MNPs was assessed *in vivo* (in mice bearing solid tumors) after their intratumoral injection ((dose of 50 μg) and -an AMF exposure of 37.4 kA/m and 500 kHz for 30 min in a single session (very much surpassing in the latter case the bio-safe limits of the field). This treatment led to the an increase of the temperature up to the value considered therapeutic(43 °C), and proved delay the tumor growth.[165] In addition, this composition gave no significant *in vitro* cytotoxicity up to the studied concentrations (200 μg_{metal}/mL). In a recent work, the efficacy of Co ferrite nanoparticles (ca. 11 nm) for MHT was assessed *in vivo*. More specifically, the nanotherapy consisted of intratumoral injections in mice bearing solid tumors corresponding to 0.4 mg of nanomaterials, followed by an exposure to theamagnetic field (27 kA/m and 115 kHz) for multiple sessions were conducted. The temperature reached at the tumor site was 45 °C (ΔT > 9 °C) within 120 s and such treatments showed considerable tumor inhibition rate. Furthermore, more than 64% of these particles could be rapidly eliminated from the body within 2 weeks.[166] However, in contrast to the previous case, Co ferrite composition gave cytotoxicity at concentrations of 200 μg_{metal}/mL. Interestingly, it was recently reported by P. B. Balakrishnan *et al.* that PMAO-coated Co-ferrite nanocubes with mean sizes of 17 ± 2 nm injected intratumorally in a murine xenograft tumor model (using xenograft murine tumor model of human A431 epidermoid carcinoma cells), could eliminate tumor (showing no recurrence up to 200 days) with a dose of 0.7 mg ([Co+Fe]) and

after 3-magnetic hyperthermia cycles (on three different days and *f* of 110 kHz and H of 20 kA×m^{-1}, which are clinically acceptable conditions).[167] The authors pointed that complete tumor elimination could be achieved thanks to cobalt nanocubes, which have the unique ability to form growing chains under an alternating magnetic field. Apart from Co ferrite, in one remarkable *in vivo* study in mice bearing solid tumors, the efficacy of Zn-Mn ferrite nanoparticles was tested upon multiple intravenous injections (3 doses of 0.3 mg Fe/ g of animal body weight each), followed by MHT treatment (for 30 min cycle performed every day for 7 days using fields of 2.58 kA/m and 390 kHz, complying the bio-safe limit). The temperature achieved at the tumor site was measured to be 43-44 °C (ΔT >7-8 °C) and considerable tumor inhibition rate was monitored over time.[168] The Mn ferrite composition has been tested mostly *in vitro* and further studies needs to be carried out.[162, 169]

Other chemical compositions such as the promising iron carbide or iron based nanoparticles have not been tested *in vivo* despite promising *in vitro* viability assays suggesting their relatively low cytotoxicity.[152]

Table 4. Heating performance represented by the SAR values of different MNPs synthesized by different colloidal synthesis methods at different size, shape and chemical composition.

Strategy to improve MHT	Composition	Shape	Size (nm)	SAR (Wg^{-1})	Hf ($Am^{-1}s^{-1}$)	Ref.
COMPOSITION	**$CoFe_2O_4$**	Nanocubes	15	**300**	3.36×10^{9}	75
	$CoFe_2O_4$	Nanocubes	17	**900**	3.36×10^{9}	75
	$CoFe_2O_4$	Nanocubes	19	**880**	3.36×10^{9}	75
	$CoFe_2O_4$	Nanospheres	12	**389**	1.87×10^{10}	63
	$MnFe_2O_4$	Nanospheres	15	**424**	1.87×10^{10}	63
	$MnFe_2O_4$	Nanoflowers	19	**689**	4.50×10^{9}	162
	$MnFe_2O_4$	Nanoflowers	54	**350**	4.80×10^{9}	164
	$Zn_{0.4}Mn_{0.6}Fe_2O_4$	Nanospheres	15	**432**	2.60×10^{9}	76
	Fe	Nanospheres	13	**305**	3.24×10^{9}	71
	Fe	Nanospheres	13	**700**	3.74×10^{9}	152
	$Fe_{2.2}C$	Nanospheres	14	**280**	3.24×10^{9}	71
	$Fe_{2.2}C$	Nanospheres	13	**3200**	3.74×10^{9}	152
	Fe	Nanocubes	11	**200**	4.77×10^{9}	77
HETEROSTRUCTURE CORE-SHELL	**$CoFe_2O_4$@$MnFe_2O_4$**	Nanospheres	15	**2284**	1.87×10^{10}	63
	$MnFe_2O_4$@$CoFe_2O_4$	Nanospheres	15	**3007**	1.87×10^{10}	63
	$CoFe_2O_4$@Fe_3O_4	Nanospheres	15	**1108**	1.87×10^{10}	63
	Fe_3O_4@$CoFe_2O_4$	Nanospheres	15	**2778**	1.87×10^{10}	63
	$ZnFe_2O_4$@$CoFe_2O_4$	Nanocubes	60	**10600**	1.87×10^{10}	83
	FeO@Fe_3O_4	Nanocubes	23	**310**	4.80×10^{9}	85
	Fe@$Fe_{2.2}C$	Nanospheres	13	**355**	3.24×10^{9}	70
	Fe@$Fe_{2.2}C$	Nanospheres	13	**2000**	3.74×10^{9}	70
HETEROSTRUCTURE MAGNETO-PLASMONIC	**Au@Fe_xO_y**	Dimers	17	**480**	4.92×10^{9}	86
	Au@Fe_xO_y	Dimers	21	**850**	4.92×10^{9}	86
	Au@Fe_xO_y	Dimers	23	**820**	4.92×10^{9}	86
	Au@Fe_xO_y	Dimers	26	**770**	4.92×10^{9}	86
	Fe_3O_4@Au	Nanoflowers	50	**170**	2.18×10^{9}	170
	Ag@Fe_3O_4	Nanoflowers	120	**49**	9.87×10^{9}	88

3.8 Synthesis of heterostructures

Another strategy to tune MHT heat performances is to prepare MNPs that merge together more than one domain at different compositions in the so-called nano-heterostructures. The first example of heterostructures are core-shell nanoparticles with different magnetic composition layers grown one on top of the other in a core/shell configuration. The SAR values of bi-magnetic core-shell structures, including MNPs with a mixed ferrite core/shell, metallic iron core and an iron carbide shell or wüstite core and ferrite shell are some examples and in the case of Co ferrite core and a shell of Zn ferrite, the reported

SAR values are as high as 1000 $W \times g^{-1}$, although this value was recorded at H*xf* product out of the range of safe MHT (Figure 7a).

Cheon *et al.* coupled magnetically hard material to a magnetically soft material as at the interface between these two materials a magnetic exchange coupling phenomenon occurs providing a direct effect on the opening of hysteresis loop under MHT (Figure 7b-d). For the preparation of this kind of core-shell bi-magnetic structures, the synthesis consists of a seed growth method, in which pre-formed seed nanoparticles are used as cores on which to grow a second material (a uniform shell). For a successful reaction, both the core and the shell must have very similar lattice parameters.[63] More in detail, the seeds were synthesized by using a mixture of M(II) chloride and $Fe(Acac)_3$ in the presence of OA, oleylamine at high temperatures. For the shell growth, the same metal precursors/surfactant mixture is added at increased temperatures along with trioctylamine. As an example of comparative heat performances, 9 nm $CoFe_2O_4$and 15 nm $MnFe_2O_4$nanospheres have SAR values below 500 $W \times g^{-1}$, but the corresponding 15 nm core-shell $CoFe_2O_4$@$MnFe_2O_4$ displays SAR values above 2000 $W \times g^{-1}$and by varying the different compositions outstanding SAR values were measured up to 2778 $W \times g^{-1}$ (for Fe_3O_4@$CoFe_2O_4$ (Figure 7a) at H*f* values of 1.84×10^{10} $Am^{-1}s^{-1}$.[63, 76] These values could be increased even more by choosing ferrite nanocubes rather than spherical nanoparticles as seeds reaching record SAR values of 10,600 $W \times g^{-1}$ for $ZnFe_2O_4$@$CoFe_2O_4$ MNPs (see Table 4 for a summary).[83] Among the materials having a soft magnetic core (either iron oxide, manganese ferrite or zinc ferrite) and a hard magnetic shell (cobalt ferrite), the SAR values follows the order: $SAR_{Zn\ ferrite\ core} > SAR_{Mn\ ferrite\ core} > SAR_{Iron\ oxide\ core}$. Despite the fact that the SAR characterization was not complying with the H*xf* factor, this strategy may be the most promising to increase the heating efficiency of MNPs at the minimal dose of magnetic materials needed to be administered. However, for all those compositions where besides iron and oxygen other potentially toxic elements are included (Co, Mn, Zn), the *in vivo* toxicity must be evaluated. Indeed, with those mixed compositions if the toxic ions are locally released only to the tumor upon MHT, their elemental toxic action may thus contribute to the heat damage. This was recently reported for Co-ferrite nanocubes for instance.[167]

Other examples of core-shell structures are FeO@Fe_3O_4, which offer other advantageous features. Lak *et al.* synthesized and studied the stepwise phase transformation, at mild thermal annealing (80°C) of FeO@Fe_3O_4 core-shell nanocubes (23 nm in cube-edge) into single-phase Fe_3O_4 nanocubes already stabilized in water by a multi-dentate copolymer.[85] The oxidation process caused a 10-fold increase in the SAR heat losses performances with respect to the initial nanocubes and with a 13-fold increase in SAR value in comparison to Resovist® (Figure 7b). The peculiarity of these single-phase Fe_3O_4 nanocubes obtained from oxidation of the core-shell materials resides is their viscosity-independent SAR performances which makes these nanocubes optimal heat mediators even in intracellular or intratumoral viscous environment.

Lastly, another example of a core-shell system is represented by the metallic iron MNPs coated by the iron carbide shells.[71] In this case, it is also possible to convert the metallic iron to fully Fe/carbide nanoparticles by a very long process (140 h) and at some intermediate time points, Fe/carbide core-shell structure were obtained and correlated to the SAR values, finding out that the thicker the iron carbide shell was the higher was the SAR value of the corresponding core-shell system (Figure 7e). This offers the possibility to increase the SAR from 700 to 3250 Wg^{-1} under the clinical relevant H*xf* factor of 3.24×10^9 $Am^{-1}s^{-1}$.

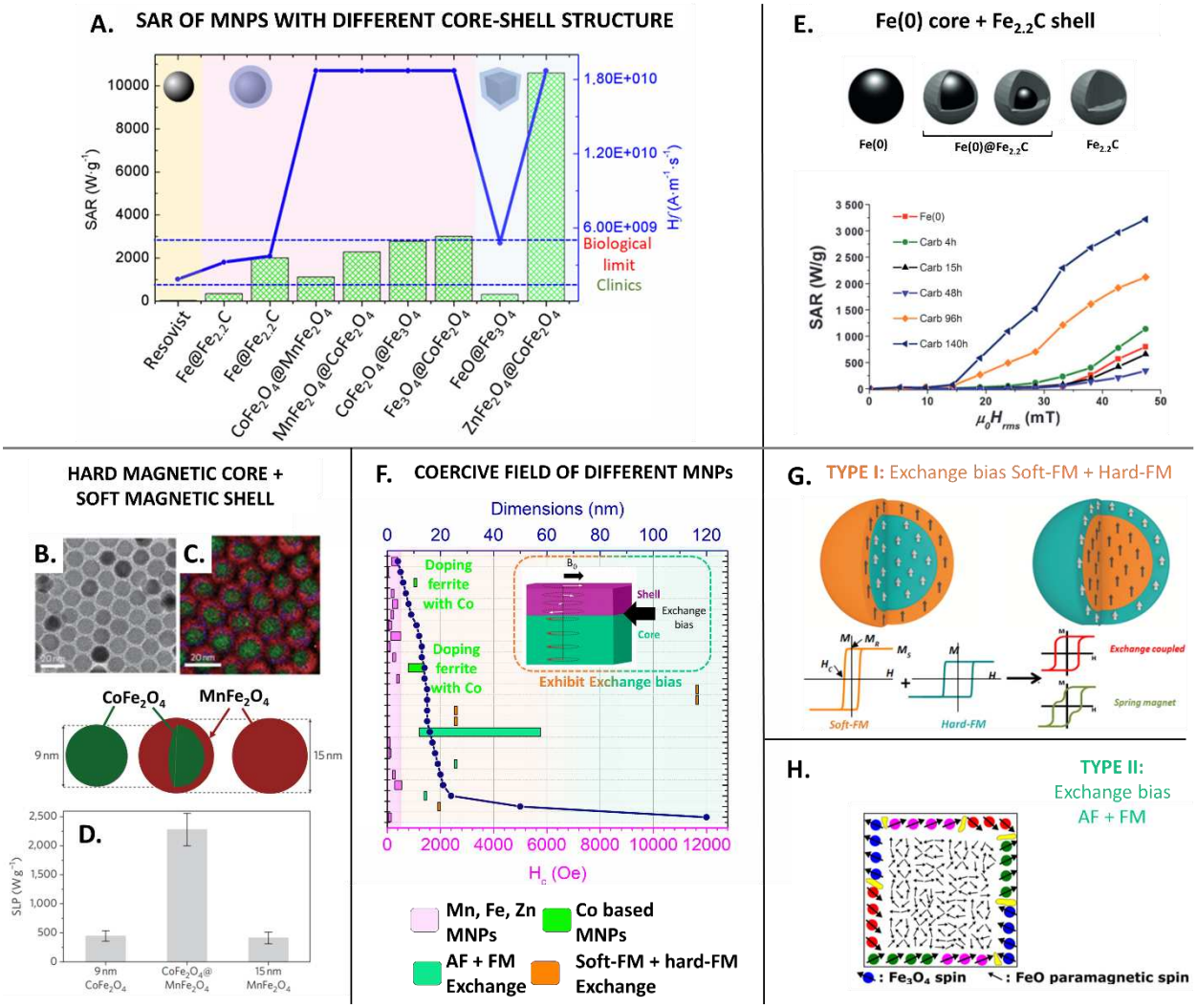

Figure 7.(A) SAR values of MNPs with core-shell structure (SAR data available in Table 4). (B-C) TEM images and compositional elemental mapping of core-shell MNPs with a hard magnetic core ($CoFe_2O_4$) and a soft magnetic shell ($MnFe_2O_4$), and (D) corresponding SAR values at Hxf of 1.84 $x10^{10}$ $Am^{-1}s^{-1}$. Reprinted with permission from[63], Copyright © 2011, by Nature Nanotechnology; (E) Examples of core-shell iron@iron carbide MNPs and corresponding SAR values at different carbidization times at 3.24 $x10^{9}$ $Am^{-1}s^{-1}$. The iron carbide shell thickness changes in the time frame between 0 and 140 hours and affect SAR values. Reprinted with permission from[70], Copyright © 2016, by Wiley Online Library; (F) Coercive field of MNPs as a function of metal compositions and size. (G-H) Types of possible exchange bias interactions: (G) Type I occurring in core-shell with a soft ferrimagnetic (sof-FM) material and a hard-FM material. Reprinted with permission from[171], Copyright © 2015, by Elsevier; and (H) Type II of exchange bias interaction occurring in core-shell with an antiferromagnetic (AF) domain and a ferrimagnetic shell (FM). Reprinted with permission from[85], Copyright © 2018, by ACS Publications.

The underlying reason for the improved values of SAR in bi-magnetic core-shell MNPs resides in such exchange coupling interaction, which can be detected by DC magnetometry by a significant increase in the coercive field of the samples. This interaction adds an extra degree of freedom to tailor the overall

magnetic properties of the nanoparticles by simply coupling different compositional core-shell materials.[171] In Figure 7f the coercive fields at 5 K are plotted for MNPs grouped by composition and as a function of their size (See also Table 2). The graph clearly shows that iron-based (iron oxide, iron(0) and iron-carbide), manganese ferrite and zinc ferrite, regardless of the size/shape, exhibit a coercive field below 500 Oe (grouped in pinked). Doping MNPs with cobalt led to coercive fields of 1200 Oe for spherical MNPs with a diameter of 6-12 nm and 800-1400 Oe for nanocubes with a cube-edge of 14-28 nm (grouped in orange).

In mixed ferrites, doping effects could be crucial. Mameli *et al.* investigated the effect of doping cobalt ferrite nanospheres with Zn ions. While cobalt ferrite MNPs of 8 nm had a coercive field value of 1200 Oe at 5K, by introducing Zn ions, the coercive field decreased to 440 Oe and, as a consequence, also the hysteresis loop under MHT closes (Figure 7f). Interestingly, for core-shell structures whose core is hardly magnetic and whose shell is soft magnetic, the coercive field is approximately 1900-2500 Oe and on the contrary, when the core is a soft magnet and the shell is a hard magnetic material, the coercive field achieves values as high as 11,600 Oe in agreement with the opening of the hysteresis loops and the highest reported SAR valued measured for both cases (Figure 7 a and f). [171] In some cases, the soft ferrimagnetic and hard ferrimagnetic materials coupling can lead to the so-called "spring-magnets", whose main manifestation in the M(H) curves is shown by "bumps". Sathya *et al.* for instance reported spring-magnet behaviour for graded composition of Co-ferrite nanocubes, with a sudden drop on the magnetization at low magnetic fields and exhibiting a maximum coercive field of 13,400 Oe at 5 K.

Lastly, FeO@Fe_3O_4 core-shell MNPs also display quite significantly high values of coercive field of 1,200-5,754Oe at 300 K due to exchange bias between antiferromagnetic (AF) material and ferrimagnetic material (FM) (Figure 7 h). Aidin Lak *et al.* showed that for smaller percentages of Fe_3O_4 the coercive field increases and the loop is shifted.[85]

Besides core-shell MNPs, other heterostructures having different arrangements of materials subdomains have been specifically synthesized for thermo-therapy. This is the case of magneto-plasmonic NPs in which the magnetic domain serves for MHT and the plasmonic domain acts as a photothermal material under laser excitation. The SAR, in this case, can be increased by concomitant application of two different activation stimuli. We can find different structures that have been studied for MHT, including hetero-dimers, nano-stars and nano-flowers (Figure 8a). With respect to the dimers, Sun *et al.* developed for the first time a seed-mediated growth-based synthetic method for magneto-plasmonic heterodimers.[172, 173] The MO_x nanocrystals are synthesized by the decomposition of the corresponding metal carbonyls, *i.e.* $Fe(CO)_5$, on the surface of the metal nanocrystal (previously synthesized or in-situ synthesized), followed by their oxidation in 1-octadecene solvent. The sizes they reported however were well below those optimal for MH (in general < 12 nm). Pellegrino *et al.* succeeded to increase the size of the iron oxide domain, by removing 1,2-hexadecanediol (HDDOL), a commonly used chemical in this synthesis, and exploit the addition of a chlorine compound, i.e. HCl or dichloroethane, to promote the growth of iron oxide domains on top of gold domain in well-faceted nanoparticles, reaching nanoparticles size of 18-40 nm and showing optimized MHT performance,[86] exhibiting SAR values of 500-650 $W \times g^{-1}$ (Hxf = 3.5-4.4 $x10^9$ $A \times m^{-1}s^{-1}$) (Figure 8 b). In comparison to the iron oxide counterparts,[72] dimers produced through this route, indeed, do not lose the heating performance when applying AMFs. However, the authors did not exploit the increase of SAR by the exposure of the samples to a laser. Nevertheless, *In vitro* results demonstrate their use is safe and that they are biodegradable[174, 175] and that once internalized by cells, their heating ability is not suppressed.[74] A. Abou-Hassan *et al.* reported a solvothermal method for the synthesis of Fe_3O_4 seeds and subsequent Au growth with nano-star shape. The seeds are subjected

to an acid treatment and their surface is activated with a small citrate ligand.[170] These heterostructures were characterized for hyperthermia treatment using magnetic fields of 900 kHz and 20 kA×m^{-1} (H*xf* = 1.8 x10^{10} A×m^{-1}s^{-1}, conditions far from that found in the clinics)[50] and a 680-nm NIR laser at a power density of 0.3 W/cm^2 (in this case authors meet the safe limit imposed in clinics for cutaneous tissues).[176] Indeed, the SAR values of MHT alone is high 634 ± 76 W/g and comparable to what has been reported by Guardia, P. *et al.* but with H*xf* combination too high for clinics. They also report SAR value of 170 ± 30 W/g when used safe conditions for clinics (H*xf* = 2.2 x10^9 A×m^{-1}s^{-1}), which implies that for the modality of MHT alone this system is not significantly better than Resovist®. On the other hand, this magneto-plasmonic design has shown *in vitro* and *in vivo* that their use is safe, and in tumor bearing mice, intratumoral injections corresponding to 0.8 mg Fe and further exposure to AMF (complying with the bio-safe limit: 20 kA/m and 110 kHz for 300 s) successfully lead to increased tumor temperatures of 8°C. However, the authors did not report the tumor growth curve. The same authors recently showed similar behavior for other similar heterostructures, i.e. Fe_3O_4-CuS, opening the possibility of tri-therapy *via* photothermal therapy, magnetic hyperthermia and photodynamic therapy.[177] Finally, R. Das *et al.* reported the solvothermal synthesis of Ag@Fe_3O_4 nanoflowers, synthesized through a solvothermal method although the reported SAR values (H*xf* = 9.8 x10^9 A×m^{-1}s^{-1}) were moderate: 47 Wg^{-1} with MHT only and 170 ± 30 Wg^{-1} when used MHT and a laser of λ = 442 nm and power density of 0.52 Wcm^{-2}, none of which improves SAR values offered by Resovist®.

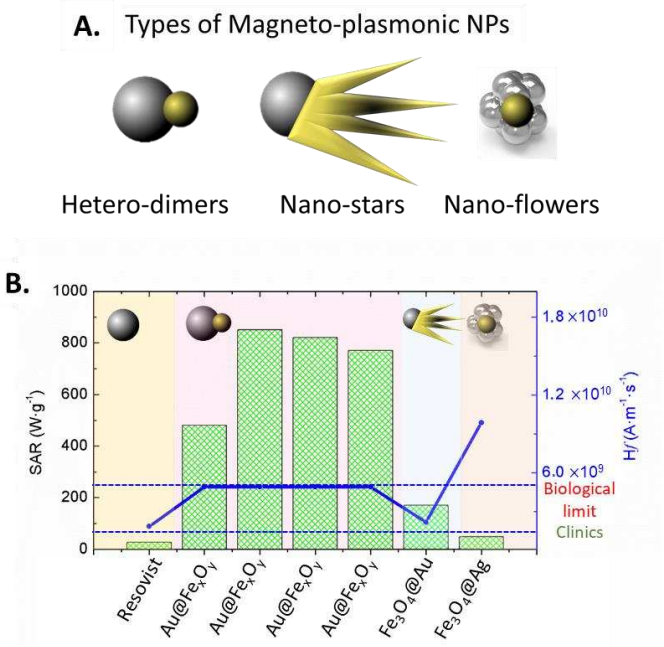

Figure 8. Design magneto-plasmonic heterodimers: (a) Types of magneto-plasmonic NPs: hetero-dimers, nano-stars and nano-flowers. Please, note that the magnetic domain is grey and the plasmonic domain is yellow in all cases; (b) SAR values of reported for each type of magneto-plasmonic NPs, having a chemical composition of either Au-Fe_xO_y or Ag-Fe_3O_4 and their comparison to Resovist®.

4.1 Magnetic assemblies and correlation with MHT heat performances

Despite tuning the intrinsic MNPs' features (magnetocrystalline anisotropy, shape anisotropy, surface/interface anisotropy, *M*s, *H*c, χ, etc.), which all affect the heating efficiency of MNPs in MHT,[142] it is also important to consider the behavior of MNPs not as individual units but as a whole sample because certain inter-particle interactions between MNPs can have a significant effect on MHT heat performances.[178, 179] In fact, it has been observed that the SAR properties of MNPs profoundly varies either positive or negative based on the inter-particle interactions thus on the orientation of their collective magnetic easy axis, occurring for instance under certain nanoparticle concentration ranges and applied magnetic field conditions.[6, 10, 16, 84, 167, 180-183] Salas, G. *et al.* investigated the heating abilities of 22 nm MNPs in agarose at two different nanoparticle concentrations (2.5 mg_{Fe} and 10 mg_{Fe} /mL) and noted a higher reduction of SAR at high concentrations with respect to the less concentrated samples.[52] This behavior was associated with inter-particle interactions arising due to the concentration effect, the magnetic moments of MNPs are brought in close proximity.[52] Indeed in random assemblies of MNPs, a demagnetizing effect can occur, due to the strong antiferromagnetic couplings of the MNPs within the clusters owing to magnetic frustration in the relaxation of individual magnetic moments[184, 185] which, in turn suppresses the heat efficiency. Such SAR reductions were also observed in other experimental studies in which, rather than studying the concentration effect, the authors had purposely to assemble the MNPs in polymeric beads with pseudo-spherical/spherical configurations.[89, 186-192] In line with these observations, the reduction of SAR values for individual MNPs once internalized by the tumor cells, have been associated to the clustering of MNPs within quasi-spherical endosomal vesicles.[74, 193-196]

It is important to note that the magnetic relaxation under MHT also depends on average hydrodynamic size of clusters[182, 184, 188] and the degree of inter-particle spacing within the cluster.[81, 189] Fu R. *et al.,* through a simulation work, which was also supported by experimental data, concluded that MNP assemblies achieve SAR improvement only if the clustering structure remains small enough and have a chain like assembly (specifically they reported higher SAR values for dimers and trimers of nanoparticles with respect to single coated nanocubes and centrosymmetrical clusters) (Figure 9a1).[185]

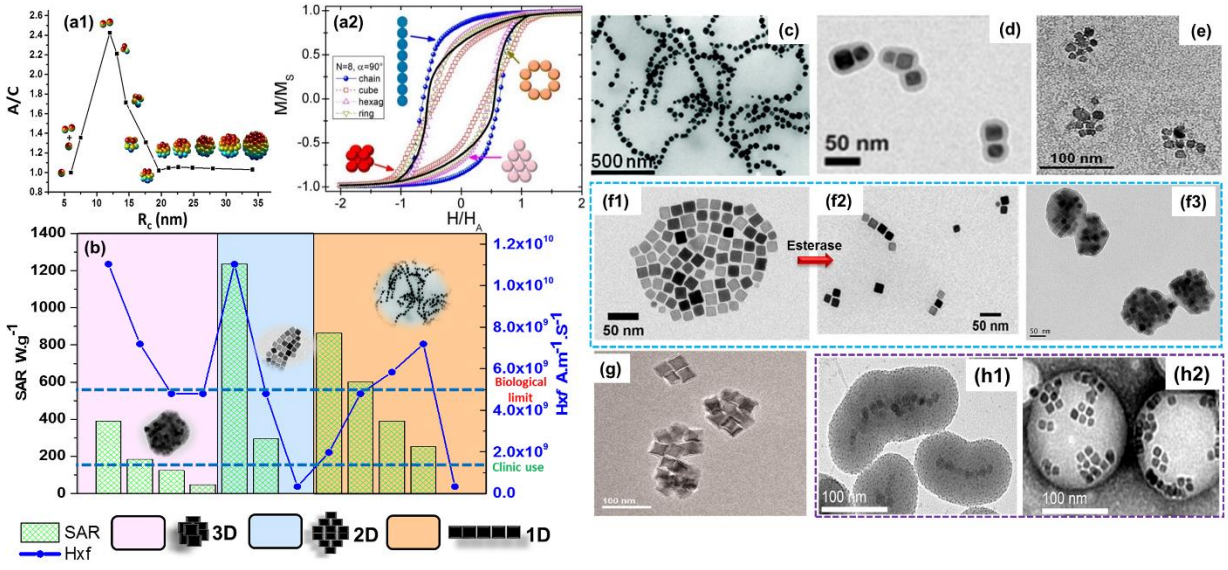

Figure 9. a1) Effect of MNPs clustering in numerical simulations: the change in shape anisotropy as function of average radius (R_c) of the cluster (reprinted with permission from[185], Copyright © 2016, by ACS Publications); (a2). Simulated magnetization hysteresis curves $M(H)$ for different spatial arrangements (bidimensional chain, hexagonal lattice, ring assembly and 3D assembly) of the same number of MNPs (N = 8), whose easy anisotropy axes randomly distributed in the direction of cone angle (α) of 90°. While the

black line represents *M*(*H*) curve of non-interacting particles (reprinted with permission from[186], Copyright © 2014, by ACS Publications); b) SAR values of nanoclusters at different geometrical so far reported in literature. c-h) TEM images of various nanoclusters produced in different studies, through solution-phase self-assembling routes, using biocompatible polymers or silica coatings. Image 'c' reprinted with permission from[197] Copyright © 2011. 'd' reprinted with permission from[89] Copyright © 2017; 'e' reprinted with permission from[198], Copyright © 2019; 'f1-3' reprinted with permission from[199], Copyright © 2019; 'g' reprinted with permission from[90], Copyright © 2012; 'h1-2' reprinted with permission from[200], Copyright © 2012, all by ACS Publications.

In support to this study, in another study, Monte-carlo simulations of the M(H) hysteresis cycles under AMF of nanoparticles arranged in linear chains were computed and compared to 2D, ring assembly of MNPs and 3D centro-symmetrical MNPs clusters (Figure 9a2).[186] These simulations confirmed that the magnetic dipolar interactions decrease the loop areas in mostly all the configurations except for the linear chain geometry where the opening of the hysteresis loop at the frequency of MHT is maximized. The dipolar coupling favored by the longitudinal alignment of magnetic crystallographic easy axis, enables the chain to behave as single long magnetic nanorod whose magnetic susceptibility enhances along the chain direction[201] thus resulting in improved effective anisotropy of MNPs and, in turn, increasing the heat losses. It is worth adding that the SAR values associated with linear geometries of MNPs depend on the angle at which they are oriented towards applied magnetic fields (Figure 9a2).[202, 203] Serantes, D*. et al.* demonstrated that chains dispersed in agarose, which significantly limits the MNPs motion, showed maximum SAR if aligned parallel (0°) to AC magnetic fields and progressively less opening of the M(H) cycles were calculated if the chain were oriented at 45°or 90° respectively.[186] At 0°, chains aligned in the direction of magnetic fields may have more freedom to flip/rotate than at other angles, thus this results in higher SAR.[186] These computed hysteresis data were also supported by MNPs forming spontaneous linear clusters under AC magnetic fields which still enabled to record SAR values higher than the corresponding individual MNPs.[201] More theoretical[186, 201, 204] and experimental studies have further confirmed the importance of chain assemblies for improved SAR values.[205-208] Very recently, Beatriz S, *et al.* by co-culturing $MnFe_2O_4$ MNPs with BV2 microglial cells under constant applied magnetic fields, observed that cells loaded within their cytoplasm with MNPs assembled into low dimensional linear chains, in contrast to spherical aggregates formed in absence of magnetic fields.[209] Interestingly, in such cellular sub-compartments, despite the fact of their Brownian motion in cellular viscous condition, the elongated assemblies retain Néel relaxation to enhance SAR values (under AMFs) by factors of 2 (576±33 W/g), with respect to random aggregates (305±25 W/g) formed in absence of DC magnetic fields.[209] Another example of forming linear structures due to inter-particle interaction under AMFs was given by Bala P. K, *et al*.[167] The authors observed the formation of chains of cobalt ferrites nanocubes directly in tumor microenvironment in an in vivo murine xenograft model upon intratumoral injections of MNPs, in response to the magnetic hyperthermia cycles that they hypothesized may induce mechanical damage alongside with a mild hyperthermia (few degree) and promoted a complete regression of tumor volume.[167]

In the direction to exploit colloidal anisotropic assemblies, the first example of chain assembly is found in nature and it is represented by magnetosome chains produced by magnetotactic bacteria made of faceted MNPs coated by a liposome membrane layer kept all together in linear assembly by actin filaments (Figure 9c). These MNP chains have greater heating properties,[206] in terms of SAR, than their isolated counterparts and they exceed by far that of commercially available superparamagnetic MNPs. Moreover, their heating was sufficiently high to inhibit the growth of human breast cancer cells (MDA-MB-231), both *in vitro* and *in vivo* model under MHT fields of clinical range (108 kHz and 40 mT).[205, 210].Overall, these configurations stood out as the best heat mediators, even under the biological limits of

magnetic excitation fields (H*xf* <5 x10^9 Am^{-1} s^{-1}) suggesting at the same time, the controlled colloidal clustering as a strategy to improve heat performance and reduce the dose of magnetic materials (Figure 9b).

Supported by theoretical studies that endorse the anisotropic arrangements for MHT, in recent years some efforts have been made to prepare colloidally stable structures of a well-defined configuration purposely made for MHT calorimetric measurements. For such assembly procedure generally high-quality MNPs synthesized by non-hydrolytic routes have been exploited.[72, 73, 211] To produce anisotropic magnetic assemblies, the micro-emulsion-based encapsulation method was found to be a promising approach,[212] to control the assemblies of MNPs and amphiphilic block co-polymers by affecting both miscibility and change of stability in aqueous solutions of the clusters building blocks.[139, 213-215] Within this, the role of various parameters which includes: the type of MNPs, the choice of amphiphilic polymer, amount of polymer and particles, solvents mixture, shaking speed, addition rates of precipitating solvent, and the rate of solvent evaporation were considered as parameters to properly control the encapsulation of hydrophobic MNPs within hydrophobic moieties of amphiphilic polymer and the cluster configuration. [187, 212, 216]

Niculaes D. *et al.* were able to successfully fabricate asymmetric clusters from stable non-interacting wüstite-magnetite core-shell nanocubes (FeO/Fe_3O_4), by using a commercially available polystyrene maleic anhydride cumene terminated (PS*c*MA, 1600 Da) polymer.[89] In this work, a mixture of THF with FeO/Fe_3O_4 NPs and PS*c*MA were precipitated by water dropping addition. To control the cluster configuration, the gradual increase of polymer amount per surface unit of MNP promoted their assembly from isolated MNPs, to short chains of two to three nanocubes (dimers/trimers, Figure 9d) to large centrosymmetric clusters, respectively. SAR values of dimer/trimers nanocube chains have higher SAR (34-40 %) in comparison to both isolated and centrosymmetric forms (at *f* = 302 kHz, H = 23.8 kA/m). Monte Carlo computational simulations concluded that longitudinal dipolar coupling of magnetic easy axis in short chains was the one which contributed mainly to increase its SAR.[89] For controlling the assemblies during co-precipitation, author highlighted the need to select non-interacting core/shell (FeO/Fe_3O_4) MNPs as building blocks due to the paramagnetic core FeO . However, the thermal annealing treatment (80 °C) of premade assemblies was promoted the phase transformation of the core/shell MNPs to single-phase Fe_3O_4 MNPs and improved the SAR values.

For the cluster preparation, besides pure iron oxide, other mixed ferrites were also exploited for microemulsion based precipitation methods. For instance, Albarqi, Hassan A., *et al.* encapsulated highly efficient cobalt and manganese doped hexagonal iron oxide nanocrystals (CoMn-IONPs) by using an amphiphilic polymer; poly(ethylene glycol)-b-poly(ε-caprolactone) (PEG−PCL, 15 kDa) (Figure 9e).[198] The anisotropic CoMn-IONP clusters, displayed the highest heating abilities (SAR = 1237 $W.g^{-1}$) with respect to nanoclusters of IONPs (390.4 $W.g^{-1}$) and to the corresponding isolated particles of CoMn-IONP (997.2 $W.g^{-1}$) and IONPs (364.5 $W.g^{-1}$) although this comparative study was performed at field excitation range exceeding the bio-limit (H*xf* = 11 x 10^{10} $Am^{-1}s^{-1}$). Follow up *in vivo* studied after systemic administration of the clusters revealed a great accumulation just by enhanced passive retention (EPR) effect of these clusters at the ovarian cancer site (26 μg_{Fe}/gram of tissue, 3.5 % of the injected dose within 12 h), with a significant tumor regression only in the mice injected with CoMn-IONP clusters and exposed to AMF of H*xf* = 11 x 10^{10} $Am^{-1}s^{-1}$.[198]

Besides synthetic polymers, bioresorbable polymers such as bacteria derivatives and polysaccharide-based polymers, were also exploited for the controlled assembling and disassembling of colloidal anisometric designed magnetic clusters. Avugadda, S. K. *et al.* have recently reported the preparation of bidimensional (2D) clusters (2D-MNBs)[189] based on an esterase cleavable polymer of bacteria origin, the Oligo polyhydroxyalkanoate (Oligo-PHA) and one single phase iron oxide nanocubes (IONCs)[189, 217] (Figure 9f1). The linearity, crystallinity and amphiphilic features of Oligo-PHA together with cubic facet interaction of particles played both a critical role for desired 2D geometry. In direct

comparison, 2D-clusters have intermediate SAR values with respect to isolated particles and the three-dimensional clusters made of the same iron oxide nanocubes (3D-MNBs). However, the real advantage of these 2D-clusters derived by the degradation of the polymer to lytic enzyme and, in turn, to the effect on the heat performances: the disassembling of the 2D-clusters into short-chain of nanocubes by esterase at 37 °C, after a short incubation time (3h) (Figure 9f2), resulted to at least 2-fold increase in the SAR values (599 $W.g^{-1}$) in comparison to the assembled 2D-MNBs (294 $W.g^{-1}$) and significant with respect to that of the single coated nanocubes (Figure 9f3).[189]

In another study, IONCs (FIONs) of size 30 nm were clustered into (D = 103±15 nm) water-soluble assemblies (Chito-FIONs, Figure 9g) within an amphiphilic chitosan oligosaccharide-conjugated with L-3,4-dihydroxyphenylalanine (chitosan-DOPA) where each cluster held 4-10 MNPs. Under MHT (f= 1 MHz and H= 0.66kA/m, H*x*f value =6.6 x 10^8 $Am^{-1}s^{-1}$), the clusters dissipate remarkably high heating, with SAR values up to 2614 $W.g^{-1}$, which are higher than the corresponding single-core IONCs (1792 $W.g^{-1}$) and notably, 30 times higher than commercial IONPs (83 $W.g^{-1}$, Feridex; another commercial standard). This heat performance has been attributed to the inter-particle magnetic dipolar coupling and enhanced saturation magnetization of the clusters (105 emu g^{-1}_{Fe}). These clusters were also proven to have antitumor efficacy in vitro and in vivo models on a Human lung carcinoma) when exposed to an ac magnetic field of H*f* value = 6.6 x 10^8 $Am^{-1}s^{-1}$.[90]

An alternative strategy to fabricate assemblies is to use a two-step sol-gel-based Stöber process to condensate tetraethyl orthosilicate (TEOS, silica precursor) and form an inorganic layer of silica (SiO_2) on the surface of MNPs arranged in a well-defined nano-worms configuration.[207] In this protocol, the initial hydrophobic nanocubes (13±1 nm) were first water-transferred using tetramethylammonium hydroxide and later the Stöber process occurred in a mixture of water/EtOH, with ammonia and TEOS as chemical precursors. The thickness of silica was adjusted by varying the amount of TEOS or the sonication time. Despite the low SAR values, likely due to the very tiny nanocubes used (13±1 nm), even in this case the anisotropic shape nano-worms (Figure 9h1) exhibited relatively high M_s and SAR values with respect to isolated and close-packed structures representing 2D arrangement (Figure 9h2).[207]

Table 5. SARs of different MNPs reported in literature under viscous conditions using various solvent mixtures.

Composition	Size (nm)	Coating	Medium	Solvent Mixture (v/v %)	*H* *kA.m^{-1}*	*f* *kHz*	H×*f* $Am^{-1}.s^{-1}$	SAR (Media) $W.g^{-1}$	SAR (Water) $W.g^{-1}$	% of SAR lost	Ref
Fe_3O_4	11	Citrate	Glycerol /water	81	20	100	2.0×10^9	38	40	5	[194]
Fe_3O_4	21	Citrate	Glycerol /water	81	20	100	2.0×10^9	48	78	38,46	[194]
Magnetosome chains (maghemite)	-	Phospho lipids	Agarose	2 wt%	18,3	108	$1,97 \times 10^9$	54	864	93,7	[206]
Induvidual Magnetosome (maghemite)	-	SDS	Agarose	2 wt%	18,3	108	$1,97 \times 10^9$	270	529	48,96	[206]
Fe_3O_4 Cubes	14	ND-PEG-COOH	Glycerol /water	81	24	302	$7,24 \times 10^9$	300	310	3,2	[15]
Fe_3O_4 Cubes	18	ND-PEG-COOH	Glycerol /water	81	24	302	$7,24 \times 10^9$	280	502	44,2	[15]
Fe_3O_4	20	-	Agar	5	39,8	105	$4,17 \times 10^9$	69	85	18,8	[21]

FeO/Fe$_3$O$_4$	23	Multidentate	Glycerol /water	84,3	24	301	7,22× 10^9	319	375	38,46	[85]
Fe$_3$O$_4$ Cubes	14	Gallol-PEG	Glycerol /water	86	24	100	2,4 × 10^9	98	120	18,3	[218]
Fe$_3$O$_4$ Cubes	23	Gallol-PEG	Glycerol /water	86	24	100	2,4 × 10^9	38	205	81,4	[218]
CoFeNPs	21	PC18	Glycerol /water	86	24	100	2,4 × 10^9	4	440	99,1	[218]
CoFe$_2$O$_4$	20	-	Agar	3 wt%	5,17	178	2,4 × 10^8	9,1	38,7	76,4	[219]
MnFe$_2$O$_4$	20	-	Agar	3 wt%		178	2,4 × 10^8	10	12	16,6	[219]
Fe$_3$O$_4$ Cubes	23	Gallol-PEG	PEG 400	100	16	300	5 × 10^9	154	222	30,6	[187]
Mag Beads-in PEG 400	173	PC18	PEG 400	100	16	300	5 × 10^9	9	48	81,25	[187]
***MAG Beads in* Diethylene glycol**	173	PC18	Diethylene glycol	100	16	300	5 × 10^9	31	48	35.5	[187]

4.2 Viscosity and microenvironment effects on heat performances of MNPs and assemblies

At first sight, the comparison of the heat efficiency of MNPs requires the measurement of SAR values in aqueous solutions. However, aiming at clinical use, to evaluate SAR performances in conditions that mimic cellular or tumor environments, it becomes crucial to achieve optimal heat effects. Generally, magnetic hyperthermia studies on cells have highlighted that the heating efficiency of MNPs substantially drops (up to 70-90 %) as soon as they are associated with tumor cellular microenvironment.[74, 196, 220] This behavior is attributed to the intracellular aggregation and due to intracellular viscous conditions.[221, 222]. For instance, iron oxide nanocubes and nanoflowers showed a substantial drop of SAR by 74 % and 100 %, respectively, once internalized into cells depending upon the dimensions (For example, in the case of iron oxide nanocubes this effect was more marked for 18 nm than for 15 nm nanocubes).[74] For this, a wide range of viscosity-dependent calorimetric measurements and AC susceptibility studies have been conducted [74, 85, 91, 223, 224] choosing solvent mixtures at different viscosity values or in colloidal suspensions that mimic aggregation conditions (i.e. addition of albumin protein), which may also induce changes in hydrodynamic size. Table 6 summarizes the solvents typically used to investigate the effect of viscosity on MHT heat performance, along with the corresponding viscosity. It is worth noting that the hysteresis area of MNPs is determined by coexistence of relaxational losses such as Néel (τ_N) or Brownian(τ_B) under the AMFs. The Brownian reversal mechanism shows a strong dependence on the hydrodynamic size of the nanoparticles and viscosity of the media (see eq 5), which are both substantially affected in cellular environments.[195, 225] Therefore, MNP heating through Néel relaxation is mostly preferred for magnetic hyperthermia application in the view of their dependence on magnetic parameters of the nanoparticles, which are less affected by biological environments. Henceforth, viscosity studies also help to predict which relaxation process governs preferably the effective relaxation (τ) of MNPs for heating. Different MNPs parameters include volume (V)/hydrodynamic size (d_H), composition and resulting anisotropy profoundly determines the SAR performance in media more viscous than that of water (0.9 mPa.s).[15, 85, 194] As shown in the Table 6, generally, MNPs of Fe_3O_4 composition with size <15 nm have SARs relatively independent on viscosity (low SAR drop percentages) in comparison to nanoparticles of the same composition but

bigger sizes or to iron oxide ferrites doped with elements such as cobalt, which are known to have hard ferromagnetic behavior with high anisotropy.[194, 218, 226] The same is true for iron-based ferromagnetic iron carbide nanoparticles.[152]. This is because, when crystal volume or the anisotropy increase (in the case of doped nanoparticles) the effective relaxation (τ) of MNPs will be dominated by Brownian motion, which limits their performance in viscous conditions. For instance, Cabrera, D. *et al* studied the SAR of Fe_3O_4 nanocubes of size 14 and 24 nm in comparison with Co-ferrite (CoFe) NPs of size 21 nm in glycerol (viscosity range from 0.9 - 153.5 mPa.s) by considering anisotropy (*K*) and volume (*V*) of crystals as factors. Here, the SAR of 24 nm Fe_3O_4 nanocubes and 21 nm CoFe NPs decreases with an increase in η due to the fact of the increase in volume and anisotropy respectively. However, the dependence was notably very strong in the case of highly anisotropic CoFe nanocubes (*K* of cobalt ferrite = 290 kJ m^{-3}) with respect to Fe_3O_4 cube (K = −13 kJ m^{-3}), though the size was smaller than 24 nm IONC.[218] On the other hand, iron carbide showed a drop of nearly 40% in glycerol mixture (50 % v/v) but it has still a SAR value comparable to 21 nm IONPs with SAR of 300 $W.g^{-1}$ in viscous media.[152] Another study on 11 and 21 nm citrate coated IONPs in glycerol (97 mPa.s) also confirmed the drop of heat only for 21 nm IONPs (of about 37 %) in viscous media (97 mPa.s).[194] Besides the above-mentioned compositional and size parameters, deficiencies and structural defects can also drive the effective relaxation process mostly by the Néel instead of the Brownian mechanism. Aidin L. *et al*. reported that 23 nm core-shell IONC (FeO/Fe_3O_4), once thermally oxidized at mild conditions (80 °C for 48h), were converted into a single-phase Fe_3O_4 composition but the presence of Fe^{2+} deficiencies and structural defects affected the magnetic moment response with the final effect that the SAR remains essentially unchanged with viscosity increase (only a drop of 15 %) [85] in contrast to nearly 100 % drop for 24 nm prepared with very high crystalline structure such as the Fe_3O_4 nanocubes reported by Cabrera *et al*.[218].

The impact of viscosity can be evident even in colloidal nano-assemblies, as they generally possess larger hydrodynamic size and are more susceptible to Brownian motion impairment in viscous media, thus limiting the SAR. Indeed, a distinguished behavior was noted in long magnetosome chains containing iron oxide nanocrystals of 35-50 nm, whose SARs drastically shrunk by 93% in agar aqueous solution (2% (w/v), with respect to the same sample in water, while in comparison, the immobilization of their corresponding individual particles in agar matrix (2% (w/v)) brought to a SAR loss of only 48 % with respect to the same nanoparticles in water.[210] Similarly, results were observed for larger hydrodynamic size magnetic nanobeads (clusters of iron oxide nanocubes, d_H size 173 ± 61 nm), whose SAR at 300 kHz and 16 kA/m has been decreased by 35 % and 81 % in viscous solvents of diethylene glycol (η = 35.7 mPas) and PEG 400 (η = 90 mPas) respectively, in comparison to the same clusters in water[187]; refer Table 6.

To summarize, despite the large portfolio of MNPs and clusters produced, the SAR viscosity data are available only for a small fraction of those materials. SAR-dependent-viscous measurements may help to predict the behavior of MNPs in tumor environment and in vitro cellular experiments as they could anticipate the heat behavior of MNPs at the tumor under MHT clinical conditions.[227]

Table 6. List of solvents typically used to investigate significance of viscosity on magnetic nanomaterials heat performance.

Solvent	Mixture (v/v %)	Viscosity (mPas)	Ref.
Glycerol	Upto 84	97.3	15, 67, 85, 152, 194, 218
Agarose	Upto 5	-	21, 186, 206
Diethylene glycol	100	35.7	187
Poly(ethylene glycol) 400	100	90	187, 223
1-2-propanediol	100	40	223
Ethylene glycol	100	17	223
Gelatin	20	-	136

5 Clinical Trials of Magnetic Hyperthermia Therapy

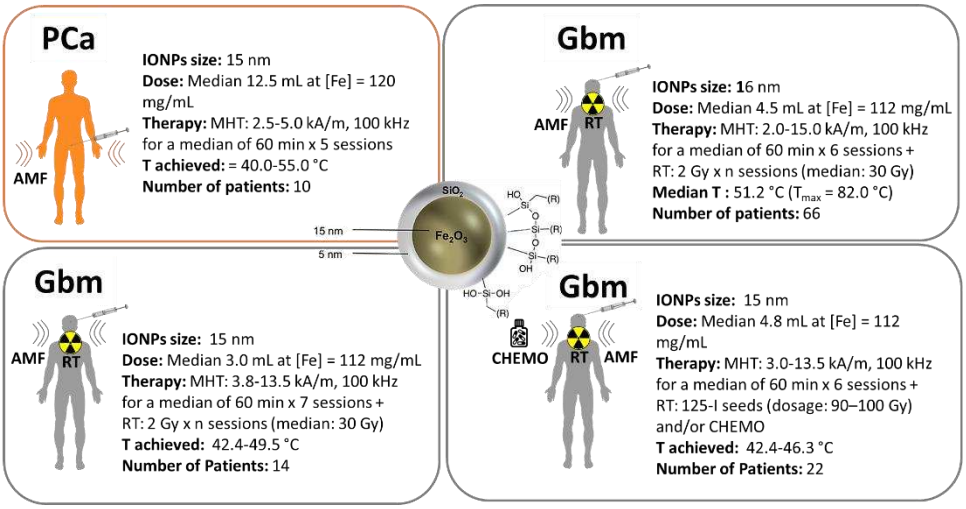

Figure 10. Main clinical trials conducted so far with MHT using iron-oxide magnetite (Fe_3O_4) nanoparticles (15-16 nm) with an aminosilane coating . In each box, the main conditions of the treatment are summarized. The amount of ferrofluid, number of sessions and total amount of radiation were adjusted to the patients need, thus in this figure, the median numbers are provided, which have been rounded up.

Very recently, approvals to conduct phase I and phase II clinical trials with MHT have been granted to the Magforce company which have built an AMF applicator (MFH 300F) suitable for GBM and PCa patients (Figure 10). In these trials, at a frequency of 100 kHz, the intensity field (H) conditions were adjusted in the range of 2 to 15 kA/m to personalize the MHT treatment depending on the patient tumor.[228] The selected ferrofluid used on patients consists of spherical Fe_3O_4 nanoparticles synthesized by hydrolytic methods and provided with an aminosilane coating, with a mean diameter (D) between 12-16 nm.[229] Indeed, although no SAR values of the as prepared MNPs are available, in one of those clinical studies the estimated SAR at the tumor was of 288 WKg^{-1} assuming a homogeneous distribution of nanoparticles in the tumor mass. Practically, the inhomogeneous distribution of MNPs at the tumor make this SAR estimation very challenging and still methods to determine the tumor temperature increase, and thus the SAR at the tumors are still matter of study.

Besides nanoparticles features, the dose of MNPs to be deposited at the tumor to raise the temperature to a therapeutic value strongly depends on type of tumor and patient tumor volume (thus it is adjusted to the patient's needs) and it is in the range of few milliliters (3-13 mL) of a highly concentrated solution of MNPs ([Fe] = 112-120 $mg \cdot mL^{-1}$).

For prostate cancer (PCa) patients, the dose injected per patient ranged to a median value of 1.5 g_{Fe} and MNPs could be visualized at the prostate by CT-scans several months (more than 4) after the magnetic fluid's injection. This suggest that IONPs were retained in the tumor tissue for at least several

weeks and were not cleared by macrophages. The reduction of prostate-specific antigen (PSA) on prostate gland was used as a marker to verify the effectiveness of MHT thermal cytotoxicity.

For GBM patients, the median MNP dose was less (0.3-0.5 g Fe), however, in this case MHT was used as adjuvant therapy to external radiation therapy (RT)[230] or to chemotherapy.[231] It is worth to note that the MNP dose used in MHT significantly differs from that needed in MRI scan (milligram scale for MHT versus only microgram scale in MRI). The large MHT dose has a strong impact on the use of MRI as a diagnostic tool: indeed, it impairs the use of MRI for tumor monitor after MHT, requiring other diagnostic imaging tools (like CT or PET). [230] In a first randomized trial (DRKS00005476) the efficacy and safety of monotherapy (MHT alone or RT alone) versus the combination of MHT with RT was evaluated in recurrent/progressive glioblastoma. This combinatorial treatment was well tolerated by all the patients with minimal side effects. Indeed, the impact of MHT treatment was evaluated in terms of Quality of Life (QoL) of patients at different time window indicating only early moderate and manageable morbidity that is a clear indication of no medical problems caused by the MHT treatment, while there was no significant deterioration of physical functioning, global health status and treatment-related symptoms. The phase II trial was aimed to evaluate the overall patient survival following the diagnosis of first recurrence of the tumor and involved 57 patients with recurrent GBM, and maximum tumor diameter of 7 cm. The median overall survival from the diagnosis of the first tumor recurrence was 13.4 months, which increased from 6.2 months with respect to the median overall survival of people suffering from GBM. The patients suffered from moderate side effects with no severe complications, which makes this combinatorial therapy very attractive.

Despite these pivotal clinical studies, MHT lacks a large phase III clinical trials in which the hyperthermia effects are combined with chemotherapy and/or radiotherapy.[232] [233] At the same time, experimental research is quickly moving towards the preparation of multifunctional magnetic based nanoplatforms and their preclinical evaluation with the aim to develop novel nanoplatforms which fulfill multiple therapeutic/imaging actions and that is why in the next paragraphs we focus on summarizing the efforts of different groups to develop multifunctional nanoplatforms and performing preclinical tests that enable to combine MHT with other tumor therapeutic strategies.

6. Magnetic hyperthermia in combination with Radiotherapy

6.1 Rationale to combine Radiotherapy with Magnetic Hyperthermia. At tumors, the presence of a vasculature that is significantly different from that of normal vasculature leads to hypoxic tumor environment [234, 235]. The lack of oxygen, contributes to render the tumor cells radio-resistant.[236] One of the key approaches to overcome the radioresistance of the tumors is to couple radiation therapy with conventional hyperthermia.[237-239] Indeed, hypoxic cells are radioresistant but susceptible to the external heat.[240] When a normal tissue is heated (not necessarily by MHT, but by any kind of heat source), the vasculature tends to expand and the rate of the blood perfusion increases thus helping to regulate the heat. However, in the tumor the disorganized blood vessel networks is not able to efficiently dissipate the heat thus trapping it inside the tumor.[241, 242] Moreover, the low pH at the tumor microenvironment, due to lactic acid accumulation in hypoxic conditions[243] makes also the tumor cells more sensitive to heat.[244, 245]

This knowledge of combining radiation therapy with external heat, of any kind of hyperthermia for the treatment of tumors, has been applied in pre-clinical and clinical models [246-250]. However, deep-seated tumors did not heat up adequately[251] and the key observation in the clinical trials was that external hyperthermia did not exhibit any substantial difference between the radiation alone and the combined therapy groups.[252] MHT based on MNPs represents an alternative approach to supplying heat with spatial and temporal control, as shown in several recent and ongoing preclinical studies.[253]

6.2 Relevant *in vivo* studies on the combination of radiotherapy + magnetic hyperthermia: The sequence of application of the hyperthermia and irradiation treatment modalities, as well as the time difference between each application is one of the key parameters for the enhancement of the damage caused to the cancerous cells. Studies have shown that reducing the time difference between the irradiation and heating will maximize the tumor cell death,[254] while a difference of more than 4 hours will nullify the radiosensitization of cells caused due to the heat.[255] However, in tumors, it was found that mild hyperthermia treatment may induce temporary resistance to any subsequent heat treatment,[256] a phenomenon known as thermo-tolerance. Considering the knowledge taken from the conventional hyperthermia studies,[257, 258] a general scheme of in vivo radiotherapy and MHT therapy protocol (as shown in Figure 11a) was designed, where the tumor region was first irradiated, then the MNPs were injected and, soon after, the MHT treatment was performed. The first proof of concept study combining radiotherapy and MHT was based on spherical 15 nm iron-oxide MNPs coated with aminosilane shell, and upon injection into orthotopic tumor model, the additive effects of MHT and radiation therapy were tested.[30] The key finding of this work was that the dual therapy was significantly able to reduce the tumor growth in comparison with irradiation therapy alone (in the latter case even when using a three times higher dose of radiation). These same MNPs were then successfully applied in GBM clinical trials and this study remained the only work that has been tested on human patients.[33, 259]

Newer magnetic materials are being developed, which have SAR enhancement or which could also enable imaging the dual therapy response. For instance, Ohki *et al.* quantitatively evaluated tumor response to dual thermo- and radiation-therapy using Magnetic Particle Imaging (MPI). They used clinically approved Resovist® (bare superparamagnetic IONPs), in xenograft tumor models in mice [260]. Indeed, the therapeutic response in the dual mode (MHT+RT) was found to be better than any single modality (MHT or RT) (Figure 11b). MPI could track the presence of MNP in tumor and this may also facilitate the monitoring of MNPs bio-distribution after MHT sessions till the MNPs completely disappear (Figure 11b). Furthermore, the average MPI signal intensity in the MHT+RT animal group was higher than that of MHT group alone, up to 14 days after injection likely because, the radiation is known to reduce the interstitial fluid pressure (IFP) in the tumor tissue which may help for better diffusion of the nanoparticles inside the tumor and hence better MNPs' retention.

Attaluri *et al.* characterized the effect of ionizing radiation and heat on two different human prostate cancer cell lines, PC3 and LAPC-4, and observed that LAPC-4 lines having a mutated BRCA2 gene, were more sensitive to radiation as well as heat-sensitive when compared to PC3 [261]. Commercially available MNPs of spherical magnetite core and a shell of hydroxyethyl starch (Bionised nanoferrite, BNF-starch nanoparticles, from from Micromod Partikeltechnologie with ca. 100 nm in hydrodynamic size) were then injected in LAPC-4 tumors xenograft tumor models and upon dual radiation + MHT treatment, 77% of this animal group showed a tumor growth delay whereas for PC3 tumors, lacking the BRCA2

mutation, showed only 38% of the same response. This study mainly underlines the biological differences in different tumors and the need of the therapy parameters to be modulated in accordance.

Drake *et al.* had developed gadolinium doped iron oxide particles (GdIONP) by coprecipitation method which offers four times greater SAR values as compared to commercially available Resovist®. The enhanced heat performance of GdIONP was attributed to the presence of Gd dopant in Fe_3O_4 lattice which causes the changes in Néel relaxation by altering the anisotropy constant K [262]. Jiang *et al*.[263] used these GdIONPs and further demonstrated the dual magnetic hyperthermia and radiation therapy in xenograft tumor models (Figure 11c). Due to the doped Gd ions, the GdIONPS were tracked and quantified by both T_1 and T_2 contrast in MRI during the course of therapy. The temperature profile at the tumors suggests that temperature exceeds 45°C at the center of the tumor, where most of the GdIONPs were localized (based on MRI quantification), but it tends to decrease by 1.5°C every 2 mm with increasing distance from the MNPs localization. Moreover, longer times for the tumor regrowth were found after dual RT + MHT therapy as compared to single mode of therapy. This improved therapeutic response was attributed to two effects – of high temperature mediated thermal ablation in the core of tumor and mild-temperature hyperthermia mediated tumor re-oxygenation towards the periphery.

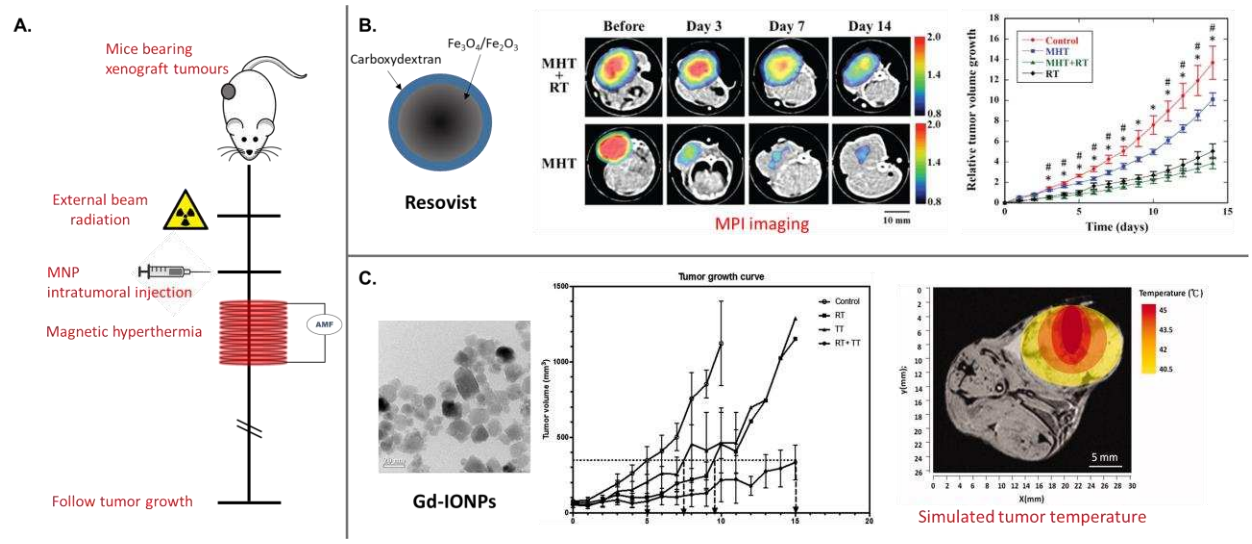

Figure 11. A) A general scheme summarizing the therapy plan for combining magnetic hyperthermia with radiotherapy in preclinical studies. B) The quantification of the MNPs (Resovists) present in the tumor tissue after MHT or MHT+RT using magnetic particle imaging (left panels), also the tumor growth graph (left panel) showing the therapeutic response for dual-modal treatment and single modal treatment (reprinted with permission from [260], Copyright © 2016, by Sci Forschen). C) The tumor growth curves under mono and dual-therapies when using Gadolinium doped MNPs-and also the simulated tumor temperature images showing the distribution of heat in the tumor region after dual therapy (reprinted with permission from[263], Copyright © 2017, by Taylor & Francis.

7. Magnetic Hyperthermia and Chemotherapy

7.1 Rationale to combine Chemotherapy with Magnetic Hyperthermia. Among several possible treatments to be combined with MHT, chemotherapy is perhaps the most intensively studied approach due to several intriguing effects which can be merged depending on the selected drug. Chemotherapy represents also the most common therapy used in clinics to treat cancer but the lack of specificity towards tumor masses can cause serious side effects in patients due to the high toxicity of the administered anticancer drugs.[259, 264-266] Moreover, the toxic feature of the drugs restricts the dose that can be administered to the patient and, together with the lack of drug specificity, decreases the effectiveness of the treatments.[267-269] The use of nanomaterials in oncology has proved to be an important tool to improve the action of traditional chemotherapy agents in terms of specificity, delivery, safety and bioavailability.[270] The increase in the efficacy of chemotherapy associated with the use of MHT is known as thermo-chemo-sensitization.[264, 271-273] There are several mechanisms involved in the boosted drug activities by MHT; among them, the heat increases the drug diffusion at the tumor enabling a better spreading of the drug at the tumor site.[259, 264, 268, 274, 275] This is mainly due to the increase in permeability and perfusion of the tumor microvasculature by localized heat under MHT exposure on one side, and by the enhanced permeability of tumor cell membrane accompanied by the inhibition of cellular DNA repairing mechanisms at therapeutic temperature (43-47°C), which are both important effects to increase drug spreading, cell uptake and potentiated drug action.[259, 264, 268, 274, 275] On the other end, exploiting the synergic effect of MHT and localized chemotherapy may represent a key solution to decrease the therapeutic temperature (41-43°C) needed to kill tumor cells, thus reducing the effective MNPs dose that would be required at the tumor for MHT.

7.2 Relevant *in vivo* studies on the combination of chemotherapy and magnetic hyperthermia: in the field of materials chemistry and pharmacological science there is an intensive research activity to develop advanced MNP-based platforms aiming not only to combine the benefit of MNPs as heat mediators and chemotherapeutic agents but also to design smart magnetic nanoplatforms in which chemotherapy can be loaded and released in a controlled and more specific manner.[267, 276-278]

To actuate the selective release of drug on demand during the MHT, most studies exploit the stimuli-responsive chemistry showing thermo- and/or pH-responsive material features. Indeed, the heat generated during MHT, represents an external stimulus that can trigger the drug release based on thermal-induced mechanisms. On the other hand, the unique tumor mass condition offers a peculiar microenvironment in which the controlled release can be promoted by different intratumoral stimuli such as the acidic pH, or the hypoxic and pro-oxidant state.[279-284] While the research of smart stimuli-responsive magnetic materials has advanced more in the direction of heat-mediated drug delivery, fewer examples are available on MNP materials designed for combining MHT with intratumoral-stimuli release mechanism (Figure 12)**.** For the latter case, several groups have developed magnetic-based nanosystems showing pH-responsive features for smart drug delivery, however, the MHT was not tested in those studies.[285-291] Among the few studies demonstrating a pH-responsive platform in which the *in vivo* MH was performed with the pH-mediated release was reported by Kim's group (Figure 12)[292] hydrophobic IONPs were decorated with poly(2-hydroxy ethyl methacrylate-*co*-dopamine methacrylamide) *via* a ligand exchange process. The presence of catechol on IONPs enables the binding of bortezomib (BTZ) *via* pH-sensitive diol-boronic acid. Upon MH treatment (3 cycles, 12.57 $kA.m^{-1}$ and 293 kHz), a clear delay of tumor growth (SCC7 cell line) was achieved although a complete tumor suppression was not achieved.

The nanoplatforms enabling heat-mediated drug release rely on two main mechanisms. A first class consists of MNPs functionalized with types of coatings that allow a thermally sensitive interaction

between the drug and the coating and the heat generated by MNPs can be exploited to disturb such drug-material interactions inducing drug release by diffusion. The second class of MNPs involves the gating process, in which thermal-sensitive materials are used to encapsulate/block drug molecules within the coating/shell on MNPs. Once the MHT heat is generated, chemical change or configuration change of such capping thermal sensitive materials with the further release of the drug molecules. Inspired by these two concepts, several strategies have been approached and numerous types of MNP-based nanoplatform showing unprecedented properties have been developed.

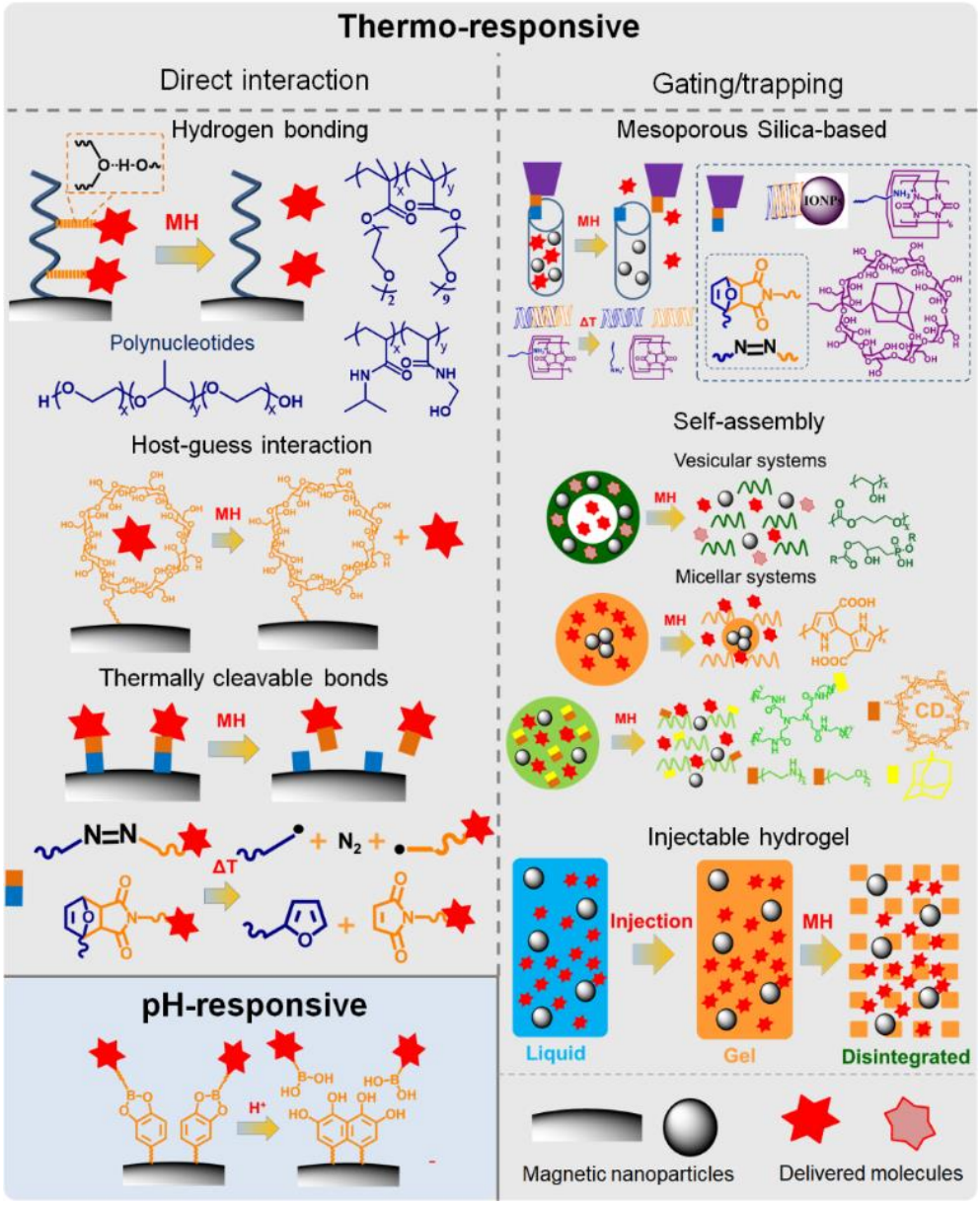

Figure 12. Scheme of different types of chemistry for drug loading and release mechanisms and the material configurations that have been exploited so far to combine magnetic hyperthermia and chemotherapy using single magnetic nanovectors.

7.2a Systems based on direct thermal-sensitive interaction between drugs and MNPs

To this class of materials belongs MNPs combined with thermo-responsive polymers (TR-polymers), a special class of polymer macromolecules which feature conformational and physical changes in response to variation in the surrounding temperature.[288, 293, 294] Nanoplatforms composed of polymers exhibiting a lower critical solution temperature (LCST) and MNPs are the most intensively studied.[288, 295] These polymers are capable of forming hydrogen bonds with water or hydrophilic drug molecules due to the existence of several hydrogen donor and acceptor moieties. These interactions are exploited to load the desirable molecules within the polymer matrix.[288, 295] Once the temperatures rise higher than the LCST, the networks of hydrogen bonds are disturbed, inducing mechanical polymer contractions with consequent cargo release. The primitive studies were focused on the nanohybrids based on poly(ethylene oxide-*block*-propylene oxide-*block*-ethylene oxide) (PEO-*b*-PPO-*b*-PEO), also commercially known as Pluronic, poly(*N*-isopropyl acrylamide) (PNIPAm) and its derivatives.[288] Despite several proof of concept studies, none of these MNPs were tested *in vivo* in preclinical- studies for combining MH and chemotherapy. [296, 297] Apart from PNIPAm and Pluronics polymers, oligo ethylene glycol methyl ether methacrylate (POEGMA) based-polymers have a tunable LCST temperature reaching also the MHT therapeutic temperature range (41-47 °C).[298, 299] Unlike PNIPAm, LCST of POEGMA are more stable as it negligibly depends on the molar masses.[299] Furthermore, POEGMA exhibits excellent biocompatibility thanks to PEG pendants along the methacrylate backbone.[299] Pellegrino's group developed surface functionalization of magnetite nanocubes with POEGMA and the thermo-responsive magnetic nanocubes (TR-cubes) had unprecedented performance in SAR under MHT clinical conditions (H=11 kA×m^{-1}, *f*=105 kHz).[300] In addition, these TR-cubes were able to load and DOXO release as an antitumoral drug (Figure 13a). The efficacy of the heat-mediated drug release, at much lower dose of DOXO, in combination to the heat damage of MHT, was also demonstrated *in vivo*, on mice transplanted with A431 epidermoid cancer cells: indeed, the group that received the dual therapy was the only one that did not show tumor recurrence. Moreover, the clearance of TR-cubes *via* kidney excretion, as shown by MRI studies, made this platform promising for local and systemic delivery. The same system was also found to be efficiently eradicate quiescent colorectal cancer stem cells in an ex vivo model.[301]

Polynucleotides, known to contain numerous hydrogen donors and acceptors, are another interesting class of materials to construct smart heat-triggered drug delivery systems. Yeh's group functionalized Fe_3O_4 nanocrystals surface with polynucleotide (5'-AAAAAAAAAAAAAAA-3', A15) and bisamino PEG, subsequently (Figure 13a).[302] The exposed amine group enables the functionalization of this nanosystem with anti-HER2 antibody to bestow their tumor targeting capability. In this study, 5-fluorouracil (5-FU) was used as chemotherapy. Interestingly, following the systemic multiple injections on C3H/HeN mice transplanted with MBT-2 bladder cancer cells, a sufficient amount of magnetic materials accumulated at the tumor and enabled to reach a therapeutic temperature (42 ^{o}C at the skin) during MH treatment. Although this is the only example in which a therapeutic temperature can be reached during MH treatment following intravenously injection administration, MHT conditions were set out of the biological limit (H=33 kA.m^{-1}, *f*=1.3 MHz).

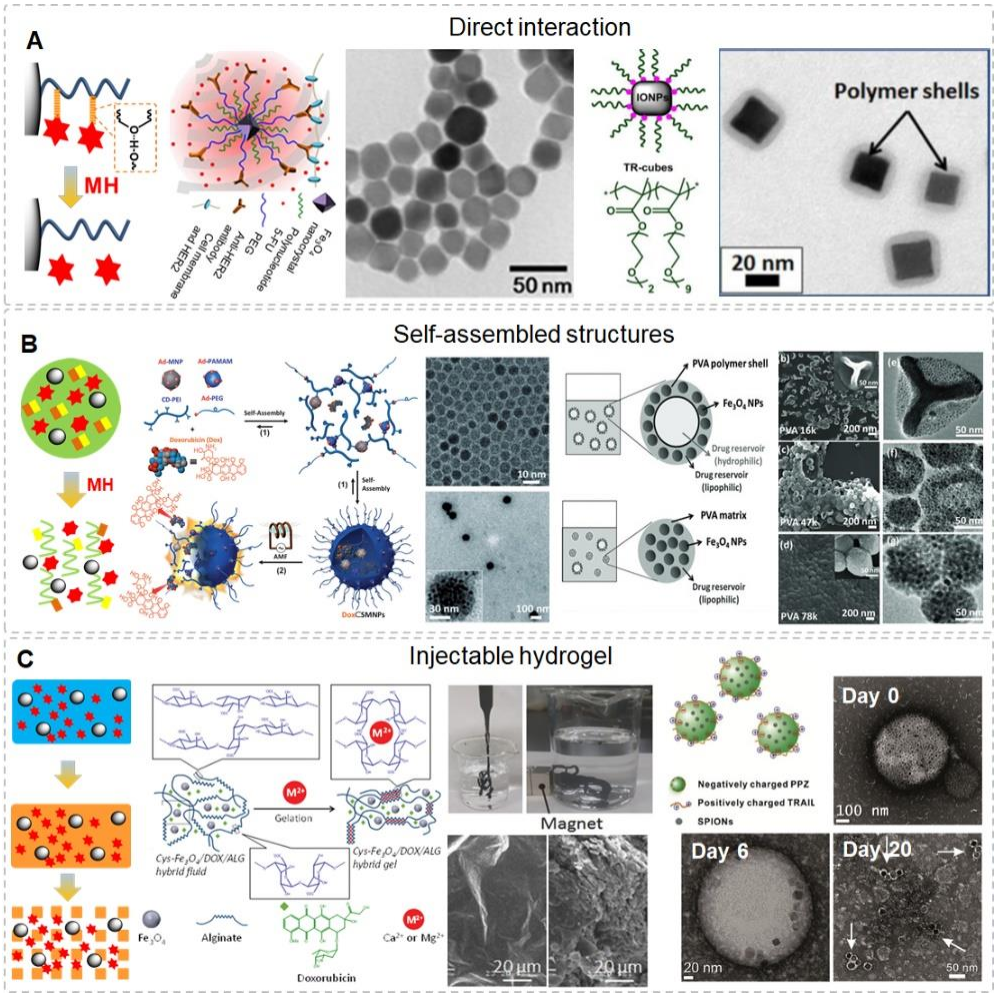

Figure 13. Examples of MNPs for combination of MHT and chemotherapy exploiting thermal-sensitive chemistry.(a) MNPs of iron oxide functionalized with polypeptide and targeting moieties for 5-fluorouracil delivery (Reprinted with permission from[303], Copyright © 2013, by ACS publication) and LCST polymer functionalized IONCs for DOXO delivery (reprinted with permission from [300], Copyright© 2019, by ACS publication); (b) MNP-based platform using host-guest interaction to selectively deliver DOXO and MNPs to tumor exploiting EPR effect (reprinted with permission from[304], Copyright © 2013, by Wiley Online Library) and polymer vesicles encapsulating MNPs, DOXO and paclitaxel (PTX) spontaneously (reprinted with permission from[305] Copyright © 2012, by Wiley Online Library) and (c) examples of gelation approach, induced by the coordination chemistry between alginate and Mg^{2+}/Ca^{2+} cations to trap MNPs and drugs at the tumor (reprinted with permission from[306], Copyright © 2016, by Wiley Online Library) and the magnetic injectable hydrogel based on polyphosphazene (reprinted with permission from[307], Copyright © 2017, Elsevier).

Host-guest chemistry, in which the drug molecule forms the complex with specific functional group on particles surface by the forces originated from unique chemical structural interaction, is also a favorable strategy to achieve MH trigger drug delivery. In this direction, MNPs surface is functionalized with cyclic macromolecules as the host and the drug as guest molecules are linked *via* specific structural interaction by forces (or docking effect) rather than other types of chemical bonds. Yogo's group exploited this chemistry by modifying the surface of SPIONs with β-cyclodextrin (host) and tamoxifen, an anticancer

drug used to treat breast cancer, as guest molecule can be loaded. The release was induced by exposing nanoparticles solution to MHT reaching a temperature of 43 °C.[308] However, this approach has not been realized for *in vitro* model yet.

In all of the above-mentioned studies, the release of drug molecules is triggered by a macroscopic increase of temperature. In practical conditions, the possibility to accumulate a sufficient amount of MNPs in the tumor for an efficient MH treatment respecting the clinical conditions *via* systemic delivery remains a critical challenge.[288] Therefore, those systems may suit only the local treatment when a suitable (high dose) of MNP-platforms can be deposited intratumorally. On the other hand, in some particular systems, it was also demonstrated that even the local heat at the surface of MNPs upon MH treatment was sufficient to induce the transformation of thermo-sensitive materials thereby providing an on-demand drug release feature. This approach has been realized *in vitro* model by Fontaine's and Rinaldi's group, in which the conjugating of drug molecules close to MNPs surface *via* thermo-labile linker occurred by Diels-Alders adduct formation while the case of diazo linkage was first reported by Pellegrino's group [303, 309]. In the most advanced study, Cheon's group bonded geldanamycin, an inhibitor for heat shock protein (Hsp), to Zn-doped Fe_3O_4 MNPs *via* diazo bonds to yield a magnetic thermo-responsive nanosystem (RAIN) (Figure 13c).[165] The release of geldanamycin, triggered by MH to eliminate the protective function of Hsp and thus making cancer cells more prone to temperature. This release, in turn, resulted in a more efficacy of MH treatment and helps to combat the hyperthermia-resistant cancer cells. In this case, the macroscopic temperature reached (43°C) was far lower than cleaving temperature of this diazo bond and therefore, it could be assumed that a very high local temperature at the particle surface triggered the release. Even though a successful treatment can be achieved in mice xenografted with MDA-MB-231 breast cancer cells using RAIN, the high condition required for MH treatment (500 kHz, 37.4 $kA.m^{-1}$) might hinder this system from being used in clinical trials.

7.3. System based on gating/trapping process Despite showing several promising performances, the platforms utilizing direct thermo-sensitive interaction between drug and MNPs lack the possibility to deliver hydrophobic drugs and macromolecules such as protein, enzyme and nucleic acid. Moreover, the chemical modification of the chemotherapeutic agent to be attached to the thermo-sensitive linker gives rise to concerns about drug pharmacological properties. To overcome these issues, magnetic nanosystems based on gating/trapping processes represent promising alternatives. Three main types of materials have been combined with MNPs to act as a hosting template for the drug: i) the platform based on mesoporous silica ($mSiO_2$); ii) self-assembled polymer/phospholipid platform; and iii) the injectable hydrogels.

7.3a. Mesoporous silica ($mSiO_2$) are used to coat MNPs providing a tunable porous structure capable of hosting a variety of low molar mass active molecules with a very high loading capacity.[310, 311] Even though the MNPs functionalized with $mSiO_2$ themselves can be used as drug carriers due to the non-specific interaction and the release can be triggered following heat-induced mechanism, the use of surface passivating moieties enable to achieve a high degree of controlled drug release. In this approach, the pores and the surface of $mSiO_2$ are tethered with bulky functionality *via* thermally cleavable bond/sensitive complex which can suppress the non-specific release.[312-316] Since the first example reported by Zink's group in which the authors took advantage of the host-guest chemistry between N-(6-N-Aminohexyl)aminomethyltriethoxysilane as the thread and cucurbit[6]urilas the cork for the gating process, several promising examples have followed.[313, 316-320] Adamantine/β-cyclodextrin complex represents the most conventional cork while thermally cleavable bond such as Diels-Alder adduct and diazo bonds have been used to link the corks to $mSiO_2$ surface.[312, 315]

Along with using bulky host-guest complex, 'nano-valve' molecules were used to passivate the $mSiO_2$ porous. Vallet-Regí's group exploited MNPs as the cork and double-stranded DNA as the thermally cleavable linkage.[313] In general, the systems based on $mSiO_2$ offer a spatial, temporal and dose control of drug release which is fascinating from the pharmacological point of view and make these systems promising for use in combined MH and chemotherapy. However, despite being extensively developed, these systems based on $mSiO_2$ have been only tested *in vitro*, leaving room for further investigations.

7.3b Self-assembly of Thermosensitive Magnetic liposomes. Liposomic nanoformulations are, so far, the only platforms approved and used in the clinic.[321-323] Due to their vesicular structure, liposomes are capable to load either hydrophobic or hydrophilic molecules thus making them versatile platforms for applications in drug delivery. Liposome membranes, at the same time, due to their lipid composition are intrinsically thermo-responsive and, therefore, can be disrupted using a pretty mild temperature(42-44 °C). [324, 325] Embedding MNPs in lipidic structures to yield the so-called thermosensitive magneto-liposomes (TMLs) is an interesting approach to trigger, by heat, the release of loaded molecules (Table 7). [326, 327] Among the different lipids and surfactants available for the preparation of thermosensitive magnetic liposomes (TMLs), the most common once which allow to achive a a phase transition temperature slightly above 40 °C, are 1,2-dipalmitoyl-sn-glycero-3-phosphocholine (DPPC), Distearoylphosphatidylcholine (DSPC), 1,2-diacyl-SN-glycero-3-phosphoethanolamine-N-[methoxy(poly(ethyleneglycol))-2000] (DSPE-$MPEG_{2000}$), 1,2-distearoyl-*sn*-glycero-3-phosphoethanolamine *N* [carbonyl-methoxy (polyethylene glycol)-2000] (DSPE-PEG_{2000}), dimethyldioctadecyl ammonium bromide (DDAB), 1-stearoyl-2-hydroxy-sn-glycero-3-phosphocholine (MSPC), cationic lipids stearylamine (SA), and cholesterol (CH). [328-330]

TABLE 7. THERMO-SENSITIVE MAGNETIC LYPOSOMES IN CANCER THERAPY

LIPID BILAYER COMPOSITION	**Nanoparticle composition**	**Drug**	**Targeting**	**Hyperthermia**	**Stage of the study**	**Ref.**	**Year**
DPPC/CH	Fe_3O_4	Gemcitabine	N.A.	30 kAm^{-1}, 356 kHz	*In vitro*	[330]	2016
DPPC/DSPC/	Fe_3O_4	Doxorubicin, m-THPC (PDT)	N.A.	13.5 kAm^{-1}, 375 kHz	*In vitro*	[331]	2016
DPPC/CH/DSPE-PEG_{2000}	Fe_3O_4	Curcumin	N.A.	15 kV, 50-100 kHz	*In vitro*	[325]	2017
DPPC/CH/DSPE-PEG_{2000}	Fe_2O_3/Fe_3O_4	N.A.	N.A.	10-160 kAm^{-1}, 30-3000 kHz	*In vitro*	[332]	2019
DPPC/CH/DDAB	Fe_3O_4	N.A.	N.A.	52 kHz	*In vitro*	[328]	2020
DPPC/CH/SA/DSPE-$MPEG_{2000}$/DSPE-PEG_{2000}	Fe_3O_4	Doxorubicin	Methotrexate	20 kAm^{-1}, 500 kHz	*In vivo*	[333]	2016
DPPC/MSPC/DSPE-PEG_{2000}-NH_2	Fe_3O_4	Doxorubicin	CPPs	10 kAm^{-1}, 423 kHz	*In vivo*	[334]	2016
DSPC/CH	$La_{0.75}Sr_{0.25}MnO_3$ and Fe_3O_4	Paclitaxel	N.A.	27.9 kAm^{-1}, 250 kHz	*In vivo*	[335]	2017
DPPC/CH/DSPE-PEG_{2000}	Fe_3O_4	Doxorubicin	N.A.	30 kAm^{-1}, 3.5 MHz	*In vivo*	[336]	2018
DPPC/CHOLESTEROL/DSPE-PEG_{2000}-NH_2	Fe_3O_4	Irinotecan	Cetuximab	60 A, 96 kHz	*In vivo*	[337]	2019

During the past decades, parameters like the local confinement of the encapsulated magnetic nanoparticle, the size and composition of the liposomic formulation and MNPs have been tuned to achieve the most efficientchemotherapy and hyperthermia synergic effects. [326, 332, 338] [329, 331, 333]

Although magnetic liposomes and their role in cancer therapy has been extensively investigated in other reviews, [324, 339] we here stress those works in which TMLs formulations have been used for MHT application in synergy with other strategies to improve their therapeutic potential. Babincová et al. synthesized TMLs composed of DPPC/CH/DSPE-PEG_{2000}, encapsulating iron oxide magnetic nanoparticles and loaded with doxorubicin [336] *In vitro* evaluation revealed that under AMF toxicity further increased when doxorubicin was present in the formulation, due to the efficient hyperthermia-mediated drug release. To further validate these findings, *In vivo* study was conducted on a glioma mouse model exposed to MHT (3.5 MHz, 30 kAm^{-1}) M two times per week for a total of 28 days). Under these conditions, only TMLs formulation of doxorubicin was able to induce complete tumor regression in comparison to the control group not exposed to AMF and the group treated with only the free drug. To note that the value of frequency used was very high and out of the safety range possibly because the MNPs employed were not optimized for MHT. Gogoi et al., developed magnetic liposomes composed of DSPC:CH, able to encapsulate a dextran-coated suspension of lanthanum strontium manganate ($La_{0.75}Sr_{0.25}MnOf_3$, LSMO) and Fe_3O_4 nanoparticles for self-regulating hyperthermia.[335] By using a fine balance between nanoparticles' ratios, the authors were able to control the temperature reached by the liposomes under AMF, thus reducing overheating to healthy tissues adjacent to the tumor.

In order to achieve thermochemotherapy, PTX drug was also loaded into the liposomic formulation together with the nanoparticles' combination. Hyperthermia was performed *in vivo* using an AMF (250 kHz, 27.9 kA/m every 3 days) without exceeding the temperature of 43 °CThe combined treatment (MHT and chemotherapy) was more efficient than the free drug and the drug-loaded liposome in absence of hyperthermia in reducing tumor growth on a fibrosarcoma mouse model after double or triple TML dose injection, indicating the superior therapeutic performance of TMLs in presence of magnetic stimulation.

Using more complex systems, different groups have also exploited TMLs for targeted MHT and drug delivery to increase the therapeutic efficiency.

Guo et al. synthesized a TMLs formulation based on DPPC, CH, SA, DSPE-$MPEG_{2000}$ and DSPE-PEG_{2000} and subsequently functionalized the liposomes shell with methotrexate, able to target folate receptor overexpressed on the surface of different types cancer cells.[333]

Further *In vivo* study on mice injected subcutaneously with HeLa cells demonstrated that hyperthermia induced by a combination of MHT stimulation (20 kAm^{-1}, 500 kHz) and near infrared laser irradiation (808 nm 0.8 W/cm^2) was efficiently able to reduce the off-target side effects in comparison to the treatment with the free doxorubicin due to the active cancer cells targeting and trigger doxorubicin release, to increase the specific cytotoxic effect at the tumor site, . Importantly, the thermochemotherapy effect was significantly greater in DUAL thermal therapy-modality (photo-ablation+ magnetic actuation) demonstrating the suitability of TMLs for synergistic multitherapy of cancer.

Lin et al. developed TMLs composed of DPPC and MSPC with cell penetrating peptides (CPPs, peptide sequence: CGRRMKWKK) linked on the TML surface and able to encapsulate doxorubicin.[334]

In vivo study in mice bearing MCF-7 tumor xenografts showed that the liposomic formulation was effectively able to increase the temperature at the tumor site up to 43 °C under AMF. This was followed by increased specific accumulation of the drug and delayed disease progression, with respect to the group treated with the free doxorubicin and with the TMLs not exposed to hyperthermia.

Overall, taking into account the successful application of TMLs in several preclinical study, some considerations about their limitations and future challenges can be made. Given a pretty thin lyphofilic layer of liposomes (< 4 nm), the loading of MNPs with a relatively large size (ca. 15-20 nm for IONPs), which generally provides a better heating capacity, is challenging within the lipophilic double layer. In addition, owing to high critical micellar concentration (CMC), liposomes are less stable once diluted with an excess amount of media and this issue might become even more problematic in the case of magneto-liposomes. In this regard, Alavizadeh et al. reported that the *in vivo* stability of thermosensitive liposomes

was greatly affected by the chosen lipid composition.[340] While the *in vivo* stability of liposomes composed by DPPC and CH was significantly affectingdrug leakage and undesired membrane breaks, the incorporation of HSPC (hydro soy PC L-α-phosphatidylcholine) in the liposome bilayers increased the transition temperature of the lipid matrix and significantly prolonged the blood circulation of the encapsulated drug cisplatin, reducing the side effects and off-target toxicity. Even though in this latter study, the MNPs were not included, this work highlights the importance of the choice of liposomes composition for a better design of lyposomal formulations for *in vivo* applications.

7.3c. Magnetic polymer assemblies.

In comparison to liposomes, polymersomes also feature an amphiphilic vesicular nanostructure comprised of a thick hydrophobic membrane and hydrophilic lumen.[341-343] However, having a very low critical micelle concentration, polymersomes are much more thermodynamically stable.[341, 342] In addition, the size and the surface properties of polymersomes can be tailored to meet the demand of specific needs in nanomedicine. Inspired by such features, Lecommandoux's group was among the first to demonstrate the feasibility of magnetic thermo-sensitive polymersome based on poly(trimethylene carbonate)-*block*-poly(L-glutamic acid) (PTMC-*b*-PGA) copolymer for *in vitro* applications.[344, 345] Up to now, the most advanced magnetic polymersomes structure was reported by Chen's group.[305] Using poly(vinyl alcohol) with optimal molar mass and a single step emulsifying process, novel magnetic polymersome-like structure (capsule) in which the membrane is packed with hydrophobic iron oxide MNPs and PTX while the hydrophilic DOXO resided in the lumen were fabricated (Figure 13b).[305] The surface of the capsule was functionalized with a peptide (IVO24) which enabled the targeting of the system to breast cancer cells (MCF-7) as demonstrated *in vivo*. In addition, the capability of this nanoplatform to release PTX and DOXO during a very mild MH treatment (H=8 kA.m^{-1}, *f*=50 kHz) resulted in an excellent *in vivo* therapeutic efficacy as a complete eradication of tumor was achieved.[305] This is the first platform which can co-deliver hydrophilic and hydrophobic drugs exploiting the MH-triggered release feature. This fascinating nano-platform may pave the way to improve cancer treatment, holding the promise of use in clinical applications.

Other self-assembled polymeric nanostructures were obtained using host-guest chemistry. Cheon's group, for instance, developed a self-assembled nanostructure made of branched poly(ethylene imine) bearing β-cyclodextrin (CD-PEI) and adamantane functionalized – MNPs (Zn-doped Fe_3O_4 NCs, Ad-MNPs) and polyamidoamine dendrimers (Ad-PAMAM) (Figure 13b).[304] Due to the host-guest interaction between Ad and CD, these building blocks underwent the self-assembly and *in situ* trapping DOXO within its polymer matrix (DOXO<SMNPs). MH treatment, in this case, triggered a local heat to disturb Ad-CD motifs, thus inducing the disassembling of these nanostructures and the DOXO release. Interestingly, nanoplatforms featuring an optimal size of ca. 70 nm were able to preferentially home in on the tumor after 36 h of intravenous injection.[304] A MHT treatment applied at 36 h significantly suppressed the tumor growth, but recurrence of the tumor occurred after 8 days. To improve the efficacy, a second material injection was performed at day 7 followed by another MHT-treatment after additional 36 h of accumulation. In this case, a nearly complete eradication of the tumor was achieved at day 15.[304] Even though showing very interesting and promising results, rather harsh MHT conditions (H=37.4 kA×m^{-1}, *f*=500 kHz) might hinder this system from being subjected to further investigation in clinical models.

Another approach to exploit the disassembling of nanostructures during MH treatment is to trap MNPs and drug molecules in a polymer matrix having a glass transition temperature (T_g) close to MHT therapeutic temperature. At low temperature (<T_g), the polymer matrix remains a compact and rigid network to pack MNPs and drug molecules. At temperature higher than T_g promoted by MNPs under

MHT, a more flexible and less rigid polymer matrix favors the drug release. For such MNP based platform, biocompatible and biodegradable poly(lactide-*co*-glycolide) (PLGA) is an interesting candidate since its T_g can be easily tuned by varying the ratio between lactide and glycolide to meet the MHT treatment.[346, 347] Several systems based on these materials have successfully validated *in vitro* tested on different cancer cell lines, however, most of them are lacking *in vivo* preclinical studies.[84, 348] So far, the only system based on T_g polymer showing a promising *in vivo* performance was reported by Hayashi's group.[349] The authors used an *in situ* oxidative polymerization to enwrap Fe^{3+} and Fe^{2+} ions together with DOXO within a poly(pyrrole carboxylic acid) matrix and the mixture was next treated with N_2H_4 to trigger the formation of magnetic nanoclusters containing Fe_3O_4 NCs.[349] To provide targeting capability and stability in physiological conditions, the surface of this platform was grafted with bisamino PEG which allowed a post-modification with folic acid as targeting moiety. Having a T_g of 44 °C, the poly(pyrrole carboxylic acid) matrix becomes less rigid when a harmless AMF (8 $kA.m^{-1}$, 230 kHz) was applied to trigger the temperature increase. This system was successfully applied to treat multiple melanoma in mice xenografted model thanks to a combinatorial effect between MHT (44-45 °C) and chemotherapy due to DOXO release.[349]

7.3d. Injectable hydrogel. Although hydrogel do not belong to a specific types of nanoformulation, injectable/implantable hydrogel represents an interesting class of materials suitably for local treatment. MNPs and chemotherapy are dispersed in a solution that eventually undergoes a drastic change in physical-chemical properties from liquid suspension into a hydrated insoluble state (gelation) upon the injection. In some cases, the gel is first prepared, followed by the subcutaneously implantation at the tumor site. The gel matrix blocks the drug molecules and MNPs within the hydrogel networks and restricts the drainage of MNPs out of the tumor, making the system ideal for a durable and multiple MHT-treatment. Different types of hydrogel have been aimed for the implantation including polymers (PLGA, polysaccharides, poly[glycinamide acrylamide] and poly[phosphazenes]), α-cyclodextrin, peptides, and lipogels.[350-357] Among those, materials made of polymers and α-cyclodextrin have shown a great potential in combining MHT and chemotherapy even in *in vivo* model[288, 350, 354] while the ones based on peptides and lipogels are in their early stage of discovery and are mostly used sorely for MHT alone.[350, 352, 356]

PLGA is the one of the mosted used.[358-361] Zheng's group reported a mixture of PLGA, DOXO and Fe powder dissolved in N-methyl pyrrolidone to form a homogenous ferrofluid which, upon injection formed a sort of implanted gel (Figure 13). Despite showing *in vivo* proof of DOXO release and tumor growth delay, the author also reported that no temperature change at the tumor, during the MHT treatment could be detected.[360] Having an unique upper critical solution temperature (UCST) feature, poly(glycinamide acrylamide) (PNAGA) is also an interesting candidate to prepare hydrogel.[362-364] Recently, Chen's group developed a magnetic composite made of PNAGA, Fe_3O_4 NPs grafted graphene oxide (GO) as well as doxorubicin (DOXO) loaded and polyester (PE) capped MSNs.[363] This material platform shows unique triple-responsiveness to NIR laser, esterase and MHT which offers a multi-stimuli degree of control of DOXO release. Although the in vivo application was performed to combine photothermal and chemotherapy release, this materials platform is an interesting candidate for combined MHT and chemotherapy *in vivo* under AMF.Song's group also developed an injectable system based on poly(phosphazene) (PPZ) to combine MH and chemotherapy.[307, 365] In this system, PEGylated $Zn_{0.47}Mn_{0.}$[53] Fe_2O_4 NCs and tumor necrosis factor (TNF)-related apoptosis-inducing ligand (TRAIL) were used to form a homogeneous mixture in PPZ polymer solution. Upon tumor injection, PPZ underwent a gelation process at 37 °C and once MHT was applied, the gel reached 43 °C and slowly dissociated.[365] Multiple MHT treatments (4 cycles) were applied enabling a sustained release of loaded TRAIL and an in vivo efficacy

study was successfully demonstrated on mice bearing xenograft brain tumor (U87 cells) under clinically safe field conditions (13.3 $kA.m^{-1}$ and 366 kHz) with no sign of nanoplatform toxicity (the PPZ is indeed biocompatible and biodegradable).[307]

In alternative to synthetic polymers, natural abundant polysaccharides/oligosaccharides also represent interesting materials to fabricate magnetohydrogel. Thanks to its carbohydrate backbone, polysaccharides can easily form hydrogel and the mechanical and chemical traits of the gels can be modulated by a simple modification of polymer structure. Among those, alginate is a representative example of hydrogel material: the numerous carboxylic acid groups of alginate can undergo gelation via intermolecular crosslinking once being exposed to Ca^{2+} and Mg^{2+} cations abundant in human body fluid.[306, 366] Le Visage's group[366] was the first to demonstrate the feasibility of alginate-MNPs platforms for combining MH and heat-triggered release of DOXO but the first proof of concept in mice model bearing xenograft HGC-27 gastric tumor was provided by Hayashi and coworkers (Figure 13c).[306] In this study, the authors performed the subcutaneous injection of a hybrid fluid containing cysteine-modified Fe_3O4 NCs, DOXO and alginate which quickly transformed into a gel within the tumor. A clinical-tolerant MH treatment (8 $kA.m^{-1}$, 217 kHz) was then applied and a skin temperature of 38 ^oC was reached during AMF. The heat generated also induced the contractions of alginate-based hydrogel leading to the squeezing out of loaded DOXO. Eventually, the tumor was completely ablated which cannot be obtained when using MHT or DOXO alone.[306] Along with a very high biocompatibility, this nanosystem holds promise for use as a smart device to combine MH and chemotherapy. Besides alginate, chitosan is also a material of great interest for such application. Unlike alginate (AL), the use of chitosan requires the need of crosslinker to improve the mechanical and rheological properties of the resulting gels. In a pioneer study, Zhao group used bis-benzaldehyde PEG as well as Fe3O4 functionalized with PEG-benzaldehyde to from imine bonds between glycol CS chains, thus creating the hydrogel matrix.[367] Chemotherapies were introduced by adding DOXO and PTX loaded PLGA microparticles into CS solution prior to the addition of crosslinkers. It was shown that upon the intratumoral injection with this hydrogel formulation, the temperature at the tumor when using a mice xenografte MDA-MB-231 triple negative breast cancer, could increase to 48 ^oC under exposure to MHT (19.99 $kA.m^{-1}$ and 282 kHz), providing a synergic antitumor activity due to DOXO and PTX drugs release. Later, Fan's group adapted this same approach to prepare CS-based hydrogel encapsulating ferromagnetic vortex-domain iron oxide (FVIOs) and DOXO, aiming at preventing tumor recurrence by implanting the hydrogel after the tumor resection in breast cancer *in vivo* model.[368] Remarkably, the implantation of such magnetic hydrogel along with the subsequently exposure to an AMF reaching 44°C (17.5 kA/m and 495 kHz) avoid ed the tumor growth up to 21 days while in contrast, a drastic tumor regrowth was recorded in the other control groups (after 7 days). More recently, Yuan's group proposed the application of benzaldehyde functionalized pullulan (another type of polysaccharide) as a crosslinker for preparing the hydrogel.[369] In this case, $Mn_{0.6}Zn_{0.4}Fe_2O_4$ NPs coated with mesoporous silica were used as the magnetic component and DOXO was the chemotherapy of interest. The magnetic hydrogel displayed a SAR as high as 642.6 W.g-1 (26.1 kA/m and 160 kHz) along with a synergistic effect between MHT, chemo- and chemodynamic-therapy. . The injection of hydrogel on a breast tumor (4T1) xenograft model offered the possibility to achieve an ablation temperature of 50.4 ^oC at the tumor under an AMF (26.1 kA/m and 160 kHz) Interestingly, he implanted hydrogel was able to heat up the tumor to a temperature as high as 44.5 ^oC even after 7 days from the implantation. The complete tumor shrinkage was obtained only in group injected with the hydrogel and treated with MHT.

Zheng's group prepared hydrogel made of hydorypropylmethyl cellulose (HPMC), Fe_3O_4 NPs (sphere, 200 nm) and DOXO then used to treat 4T1 breast cancer in a xenograft model.[370] The release of DOXO could be triggered either by pH or MHT and the concomitant exposure to MHT prevented the tumor recurrence unti it was monitored (up to 21 days). In another approach, Zhang and coworkers exploited a unique supramolecular interaction between PEGylated Fe_3O_4 NPs (polyhedron, 35 nm) and α-cyclodextrin to induce the formation of magnetic hydrogel that can encapsulate DOXO, PTX and NIR dye (Cy7) in a one-pot preparation.[371] The resulting magnetic hydrogel featured an outstanding SAR of 1334 W.g-1 (1.8 $kA.m^{-1}$ and 410 kHz The temperature at the post-surgery cavity reached 45 ^oC during MHT (1.8 kA.m-1 and 410 kHz) and it was able not only to induced a hyperthermia condition but also enabled the gel to melt and spread, thus filling the tumor cavity (4T1 breast cancer cells). Eventually, the synergistic effectsof MHT andchemotherapies resulted in an 100% animal survival rate after 60 days without any sign of tumor relapse. Finally, in a very recent study, hyaluronic acid has been also used as polymer matrix to develop magnetic hydrogels.[372] In this study, HA was functionalized with catechol to chelate Fe_3O_4 NPs surfacethus resulting in the formation of hydrogel with Fe_3O_4 MNPs acting as the crosslinker. DOXO was simply added to the iarulonic solution before introducing Fe_3O_4 MNPs. This gel system displayed a good performance in inhibiting the A375 tumor growth in mice xenograft model only when an AMF (10 A and 1478 kHz) although the author did not reported the temperature rise at tumor.

7.4. Intrinsic toxicity of MNPs. Despite the use of standard chemotherapeutic agents, some MNP compositions contain ions that are intrinsically toxic and can exert their cytotoxic action which could be sum to the heat damage effects. The challenge is to control the degradation of those MNPs and thus the release of the toxic ions only at the tumor with enhanced effects under MHT to control in remote the cytotoxicity. Only few in vivo preclinical studies have shown the efficacy of those potentially toxic nanoparticles in MH treatments. $CoFe_2O_4$@$MnFe_2O_4$ were intratumorally injected in a xenograft tumor model in nude mice (0.075 mg) and AMFs of *f*=500 kHz and H=37.3 kA/m for 10 min led to considerable tumor inhibition rate.[63] However, no data on the temperature achieved at the tumor site was reported. In a very recent study, $CoFe_2O_4$@$MnFe_2O_4$ NPS were used for effective MHT-induced thermal ablation of primary and metastatic tumors in combination with checkpoint blockade immunotherapy.[373] Authors showed that after an intratumoral injection (0.25 mg) of $CoFe_2O_4$@$MnFe_2O_4$ nanoparticles in a primary tumor and AMF application of H=1.4 kA/m (at not defined *f*), the temperature at the tumor could reach 50 °C and was kept constant for 10 min. Authors showed a complete eradication of the primary tumor and distant tumors (metastases) by applying MHT at the primary tumor in combination with immunotherapy. In a more recent *in vivo* efficacy study, Pellegrino et al. have investigated the MHT toxicity of $Co_xFe_{3-x}O_y$ nanocubes showing an unprecedented synergistic effect originating from unique alignment of nanocubes into chain-like assembles under mild MHT which likely induced mechanical damage. This effect was combined to the intrinsic toxicity of Co ions, released under tumor micro environment and at higher dose under MHT, which brought to a complete elimination of solid tumor *in vivo* upon intratumoral injection[167] and only for the animal group that underwent MHT.

8. Magnetic Hyperthermia combined with light-based therapy

8.1 Rationale to combine Photothermal Therapy (PTT) with Magnetic Hyperthermia. MHT offers, in principle, the great advantage to thermally ablate tumors that are very deep in the body as it is possible to excite MNPs with an alternating magnetic field with no limitation in penetration through body tissues. However, the presently used MNPs suffer from low power absorption efficiency. In order to generate more heat, either more powerful magnetic fields need to be applied, which is not a feasible route for clinical application or relatively large dosage of nanoparticles needs to be deposited at the target site.[374, 375] Alternatively, some other physical stimuli such as light can be exploited to produce heat. This form of treatment, where light is exploited to raise the temperature, is call photothermal (PTT) therapy. When PTT material absorbs light, the electrons are excited from a ground to an excited state and the relaxation could occurs by many processes, including non-radiative process with the electron energy release under the form of heat. These light absorbing materials can be chromophore molecules containing cyanine, pthalocyanine or rhodamine groups,[376] or can be nanoparticles which can absorb light through a Surface Plasmon Resonance phenomenon due to coherent oscillations of the metal conduction band electrons in strong resonance with the frequencies of light.[377, 378] These plasmonic materials include metals (Au, Ag, Pd) or chalcogenides ($Cu_{2-x}E$, E = S, Se, Te), which can absorb near infrared (NIR) light in a broad range (from 650 nm to 950 nm) and dissipate heat.[379-382] This NIR light is minimally absorbed by the tissues and thus will cause minimum scattering leading to an optimum heat conversion in the presence of the photothermal materials. Due to its chemical stability and rich surface chemistry, gold (Au) has been the material of choice amongst the many available plasmonic metals.[380]. Recent clinical trials in prostate cancer patients have started that involve gold-silica nanostructures. The initial trials are to assess the biosafety of these nanostructures and the results render the nanoparticles safe for use in men with prostate cancer.[383]

In spite of such attractive features, PTT hyperthermia agent is limited by deep tissue heating due to the penetration of NIR light of only 5-10 mm.[384] Thus, the idea of fusing plasmonic materials with MNPs to generate magneto-plasmonic platforms sounds an attractive strategy to study and understand the reciprocal effects of MHT on PTT. Combination may enable to reduce the dose of both types of materials thus bypassing the accumulation problems of the right dose of MNPs or minimizing the toxicity issues of plasmonic materials.

8.2 Relevant *in vivo* studies on the combination of photothermal therapy and magnetic hyperthermia. A general scheme adopted to combine MHT with PTT requires, after administration of MNPs, often by intratumoral deposition, the simultaneous irradiation of the tumor area with light by means of NIR laser and at the same time the exposure to the time varying magnetic field (Figure 14a). This is because the simultaneous combination of MHT + laser can produce a significant increase in tissue temperature beyond that produced by the two treatments individually. Some of the key examples for combining these two heating modes in preclinical study are outlined here. Espinosa *et al.*, designed a nanoparticle system where they combined biocompatible and high MHT performing multi-core iron oxide nanoflowers, whose surface was decorated with gold-branched nanostructures.[170] The combination of magnetic and plasmonic properties in a single nanoassembly enhanced the heat generation at the tumor site (Figure 14b). Maghemite multi-core shape nanoparticles were synthesized by polyol process and gold was seeded onto the surface in the presence of polyvinylpyrrolidone (PVP). The resulting 30 nm nanostructures were intratumorally injected in PC3 xenografts and immediately followed by magnetic hyperthermia treatment

(100 kHz, 19.8 kA·m^{-1}) and laser irradiation (680 nm, 0.3 W·cm^{-2}) for 5 min each. Individual modes of heating lead to an increase of only about 9-10 °C whereas in the combination the increase in the temperature was of 20 °C within 2 min. Due to enhanced bioretention of nanohybrids in the tumor region, 80% of the heating was maintained even after 2 days of the injections. Lu *et al.* opted to use core-shell Fe_3O_4@Au particles, which had the drug cetuximab adsorbed on them.[385] Fe_3O_4 MNPs were prepared by chemical coprecipitation methods and the gold shell was deposited on the MNPs by the reduction of Au^{3+} ions on the core particle surface. Next, an FDA-approved chemotherapeutic antibody Cetuximab (C225) was physically adsorbed on the Fe_3O_4@Au core-shell particles. Subcutaneous tumor model of U251 glioma cells was used to evaluate the therapeutic efficacy the nanocomposites. Fe_3O_4@Au-C225 were peritumorally injected in the mice and they were exposed to three cycles of AMF (230 kHz, 30 A) and three irradiations with NIR laser light (635 nm, 0.3 W·cm^{-2}) for 30 min each at the interval of 24h between each application. Compared to the control group and the individual therapy groups, the tumor growth was significantly halted by the Fe_3O_4@Au-C225 mediated combined hyperthermia (Figure 14c). Remarkably, the high affinity of C225 towards EGFR receptor of cancer cells ensured a higher cell uptake of MNP-based platform and, also the antiglioma effects of C225 itself increased the efficacy of Fe_3O_4@Au-C225 in tumor size reduction. This work represents therefore an example of the emergence of trimodal therapy to potentiate MHT and PTT ablation of tumor with antibody therapy. Although gold-based nanomaterials continue to be developed, gold being very biopersistant tends to remain in the body for a longer duration. Iron oxide nanoparticles have been previously also tested for photothermal therapy, however intense laser irradiation was used (2−5 W/cm^2), which renders them useless for clinical translation.[150, 386, 387] In the search of a safe and biocompatible magnetoplasmonic agent, Espinosa et al. utilized previously developed iron oxide nanocubes[72] that held good heating efficiency at compatible clinical doses of low iron concentration (0.25 M) and acceptable laser power (0.3 W·cm^{-2}).[150] The 20 nm iron oxide nanocubes coated with gallol-PEG were intratumorally injected into mice with subcutaneous A431 tumor and followed by three times simultaneous magnetic hyperthermia treatment (110 kHz, 9.5 kA·m^{-1}) and laser irradiation (680 nm, 0.3 W·cm^{-2}) for 10 min with an interval of 24 h between each treatment. Any single heating mode could elevate the tumor temperature to 40°C but the dual heating mode could bring the temperature to as high as 50°C with the efficiency almost doubled (Figure 14d).

Apart from using gold as a plasmonic agent, several organic dyes can also be employed to function as photothermal agents in a single nano-platform with MNPs. Recently, Yan *et. al*. developed a multifunctional nanoplatform that consisted of MNPs, plasmonic organic material (poly(3,4 ethylenedioxythiophere):poly(4-styrenesulfonate), PES), NIR dye (Cyanine 7, cy 7) for imaging and a tumor targeting agent (2-deoxyglucose, 2-DG) (Figure 14e).[388] Iron oxide nanoparticles were synthesized by solvthermal method and PES was added by an *in-situ* surface oxidative polymerization technique, followed by a layer-by-layer polymer coating method to finally enable functionalization by Cy7 and 2-DG. These 94 nm nanostructures were intravenously injected in MCF-7 tumor bearing nude mice and after 24 h, the mice were exposed to AMF (f=200 kHz, H=38 kA·m^{-1}) for 10 min followed by laser (808 nm, 0.75 W·cm^{-2}) for 10 min. The tumoral temperature reached 44°C when a single mode of heating was used however much enhanced heating (55°C) was observed under the dual heating. The tumor volumes in individual heating modes were partially destroyed as compared to the control groups, while for the photo-magnetic group, the tumors were completely burnt. Additionally, due to the presence of NIR dye and MNPs, the therapy response and the tumor growth was also monitored by photoacoustic imaging and magnetic resonance imaging respectively. This work represents a key advancement for development of targeted dual therapy nanoplatform.

Biological windows for laser irradiation are the wavelengths at which the tissues become transparent due to reduction in water absorption as well as reduced scattering.[389] NIR-I biological window (650 nm to 980 nm) has been most extensively studied, however, newer generation of nanomaterials are being developed that absorb light in NIR-II (1000 nm to 1350 nm) or NIR-III (1550 nm to 1870 nm) window too.[390] NIR-II and NIR-III spectra offer much higher tissue transparency as well as much less light scattering when compared to NIR-I window thus allowing the light to reach much further below the surface of the skin. Heavy metal chalcogenides like CdS, PbS or AgS are the most commonly found NIR-II PTT agents but they also come with biocompatibility issues.[391, 392] Yang *et. al*. developed a silica nanoplatfom containing PbS/CdS QDs for NIR excitation in the second biological window and Fe_3O_4 NP for magnetic hyperthermia.[393] They demonstrated drug release (doxorubicin) by increasing the temperature of the system by simultaneous NIR laser irradiation (1.3 $W.cm^{-2}$) and magnetic field excitation (5 $kA{\cdot}m^{-1}$ at 150 kHz). The use of much higher laser power and non-biocompatible PbS/CdS QDs make it difficult for in vivo tests and subsequent clinical translation. However, this work shows potential of combining NIR-II PTT agents and MNPs for efficient and deep heat generation for cancer therapy.

8.3 Rationale to combine Photodynamic Therapy (PDT) with Magnetic Hyperthermia. Alternatively, another therapy, which makes use of light is named Photodynamic therapy (PDT) which involves cell destruction caused by the generation of toxic singlet oxygen and/or other free radicals that are produced from a sequence of photochemical and photobiological processes. These processes are initiated by the reaction of a photosensitizer (PS) with tissue oxygen upon exposure to a specific wavelength of light.[394-396] Porphyrin based photosensitisers have found the space in clinical applications because of their higher retention in cancerous tissues and due to the high quantum yields of singlet oxygen produced. The Photofrin®,[397, 398] a porphyrin based photosensitiser, has been approved for clinic trials by FDA for the treatment of multiple varieties of cancer. A major drawback of PDT is that the photosensitizing drug stays in the body for a long time, rendering the patient to be highly sensitive to light.[394] It was demonstrated that during hyperthermia, the rate of production of intracellular ROS production reportedly increases,[399, 400] so a combination of PS with MHT could lead to enhanced production of ROS at cancer sites with relatively lower concentrations of photosensitizer.

8.4 Relevant *in vivo* studies on the combination of photodynamic therapy and magnetic hyperthermia. The usual strategy to achieve dual MHT and PDT is to combine MNPs with a photosensitizer in a magnetic-based platform and, upon injection of the material, to activate it by simultaneous irradiation of the tumor region with a laser light and the AMF (Figure 14f). Di Corato *et al.* developed for instance a liposome based nanoplatform which incorporated IONPs for MHT and m-THPC (m-Tetrahydroxyphenylchlorin), a clinically approved photosensitizer drug.[14] The IONPs produced by coprecipitation methods, were located in the aqueous core of the resulting 150 nm liposomes while the photosensitizer molecules were entrapped within the lipidic bilayer. For the dual therapy evaluation, the liposomes were intratumorally injected in SKOV3 xenografts, and exposed to MHT treatment (H=23.8 $kA{\cdot}m^{-1}$ at f=111 kHz) for 30 min and also irradiated at 650 nm (laser power of 100 $mW{\cdot}cm^{-2}$) for 100 s. At the tumor region an increment of 10°C in comparison to the surrounding skin was reached within a few minutes from the switching on of the magnetic field. A complete tumor regression was achieved with this dual therapy as compared to individual groups (Figure 14g). Kim *et al*. instead, developed multifunctional nanoparticles where the core was composed of SPIONs (MNP10) and the surface was decorated with hyaluronic acid (HA) conjugated to a photosensitizer, Pheophorbide-a (PheoA).[401] 10 nm IONPs, synthesized by coprecipitation, were mixed with PheoA conjugated acetylated hyaluronic acid (AHP) under sonication, to yield 100 nm MNPs

(named AHP@MNP10). Here, dual-binding hydrophobic and electrostatic interactions ensure the coating on the modified AHP to the IONPs. Hyaluronic acid (HA) was also exploited as an active tumor-targeting moiety due to its specific binding to CD44 which is overexpressed in cancerous cells. This nanosystem managed to achieve 42°C within 5 min of heating under ambient magnetic hyperthermia conditions (112 kHz at 19.9 kA·m^{-1}), while singlet oxygen production under laser irradiation efficiency was detected by a fluorescent assay. K1735 tumor bearing mice were injected with AHP@MNP10 intravenously and after 6 h, the tumor regions were irradiated with laser at 671 nm (200 mW·cm^{-2}) for 500 s and MHT was applied (f=112 kHz at H=19.9 kA·m^{-1}) for 30 min. Only for the animal group receiving the combined treatment the significant tumor growth inhibition as compared to monotherapy or control groups (Figure 14h).

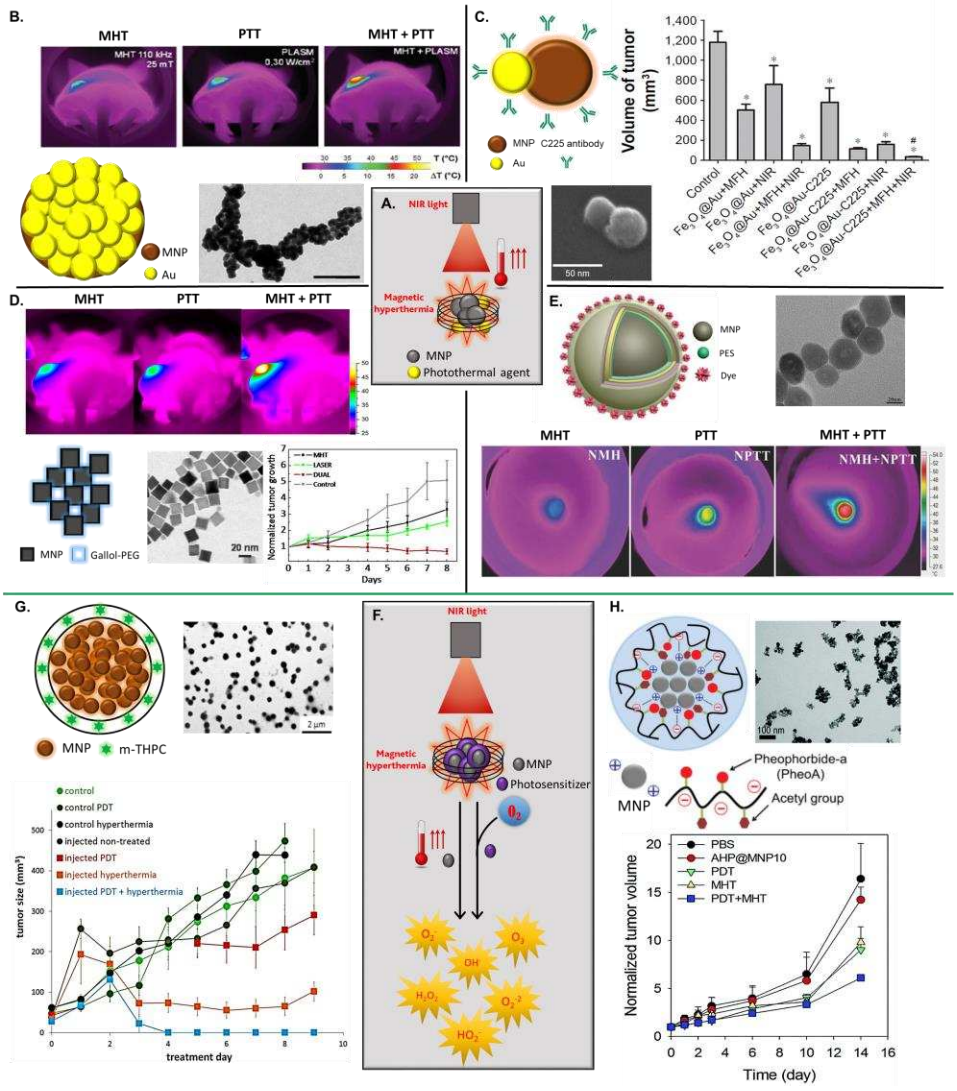

Figure 14 a) A general scheme illustrating the synergetic heat increase due to magnetic hyperthermia and photothermal therapy. b). Magnetoplasmonic nanohybrids composed of iron oxide core and branched gold shell enable to combine MHT and PTT (reprinted with permission from[170], Copyright © 2015, by RSC). Tumor regression can be observed within 5 days of treatment. c) Cetuximab (C225)-encapsulated core-shell Fe_3O_4@Au magneto-plasmonic nanoparticles injected peritumoraly into the tumor region of mice enables a combination of MHT, chemotherapy and PTT, thus causing an enhanced tumor death at the end

of the study (reprinted with permission from [385], Copyright © 2018, by Dovepress). d) Iron oxide nanocubes show dual MHT and PTT potential and allow to increase the heat on target tissue by 2 to 5 fold in dual mode as compared to single modal heating (reprinted with permission from[150], Copyright © 2016, by ACS publication). e) Multifunctional MNP@PES-Cy7/2-DG, upon intravenous injections, accumulate in the tumor region and thereafter significantly reduce the tumor volume under dual MHT and PTT (reprinted with permission from[333], Copyright © 2018, by Elsevier). f) A general scheme illustrating the formation of ROS due to magnetic hyperthermia and photodynamic therapy. g) Magnetic liposomes containing IONPs in the aqueous core and the photosensitizer payload in the hydrophobic lipid bilayer. The dual effects of heat generation by IONPs under MHT and ROS production under PDT therapy, delay more efficiently the tumor growth in a significant way already at 10-day treatment period (reprinted with permission from[14], Copyright © 2015, ACS publication). h) Multifunctional MNPs (AHP@MNPs), composed of Fe_3O_4 nanoparticles and photosensitizer conjugated by means of a modified hyaluronic acid (AHP), can selectively target K1735 tumors *via* CD44 receptor-mediated endocytosis, and also demonstrate enhanced tumor therapy through combination of photodynamic and magnetic hyperthermia treatment (reprinted with permission from[401], Copyright © 2016, by RSC publication).

9. Magnetic Hyperthermia + Immunotherapy

9.1 Rationale to combine immunotherapy with MHT. Cancer immunotherapy aims at stimulating or restoring the ability of the immune system to fight tumor.[402, 403] Some malignant cells are able to evade the tumor surveillance of the immune system by manipulating their own characteristics as well as the features of the tumor niche. Indeed, the infiltration of immune cells adds an active component in the tumor microenvironment, which can trigger the recruitment of both the innate and/or the adaptive immune system cells resulting in a concerted tumor suppression action.[404] In particular, the innate immune system, including dendritic cells (DCs), natural killer cells (NK), macrophages, neutrophils, eosinophils, basophils and mast cells, act as the first line of defense against foreign/malignant cells and do not require prior stimulation by antigens.[405] Instead, the adaptive immune system, including B lymphocytes, CD4+ T lymphocytes, CD8+ T lymphocytes (CTLs), requires the formal presentation by antigen-presenting cells (APCs) for its activation, generating then antigen-specific T-cells or B-cell lymphocytes active against malignant cells.[405]

Pioneering work of Dr. Coley in the 1890s have established a clear connection between body temperature increase (*i.e.* fever) and the response of the immune system to tumor cells.[406-408] Indeed, heat (generated by whatever exogenous or endogenous source) directly activates the intratumoral immune cells, increases the production of interleukins and promotes the trafficking of immune cells between tumors and lymph nodes by inducing the vasodilatation of the blood vessels surrounding the tumor mass.[406-408] Furthermore, tumor cells exposed to hyperthermia release or present on the cell surface the so-called damage-associated molecular patterns (DAMPs) type of antigens, which in turn, can be recognized by the tumor associated dendritic cells (TADCs) and the tumor associated macrophages (TAMs).[409, 410] Among DAMPs, heat shock proteins (HSPs) released from necrotic cells exposed to hyperthermia induce the maturation of DCs into antigen presenting cells (APC), which in turn initiates the signaling cascade that leads to the activation of other components of the immune system such as Natural Killer cells (NKT-cells) and T-Lymphocytes (T-cells) (Figure 15).[411, 412] Furthermore, among DAMPs, also calreticulin proteins represent potent immunostimulatory proteins released intra- and extracellularly in

response to apoptotic stress conditions:[413] when calreticulin binds specifically to a lipoprotein receptor on TADCs surface, an important phagocytic signal is triggered, stimulating TADCs maturation in APCs.[414]

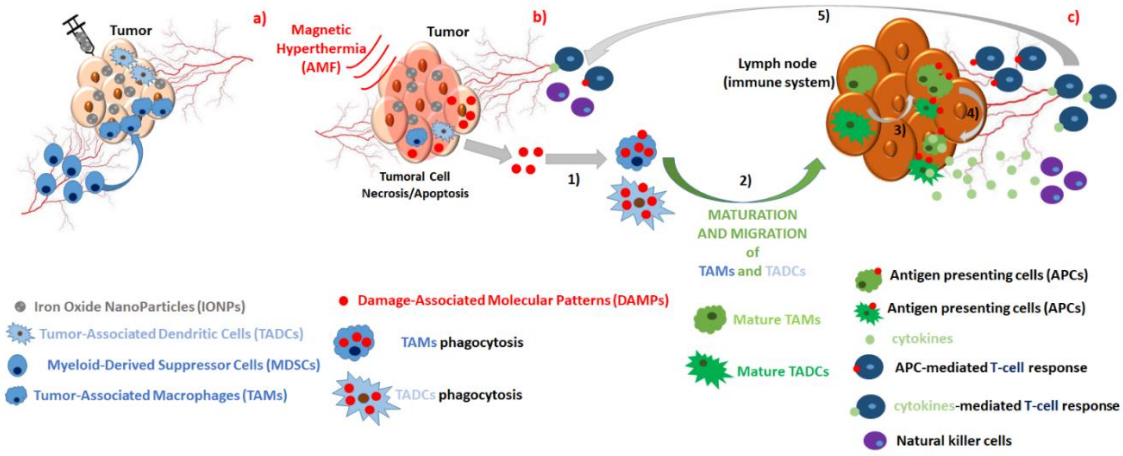

Figure 15. MNPs-mediated thermo-immunotherapy. a) Intratumoral Injection of MNPs (IONPs) promotes the recruitment of Tumor-infiltrating immune cells (TADCs, MDSCs, TAMs cells). b) Upon MHT treatment, the heat-cell damage induces cell death *via* necrosis or apoptosis, promoting the release of DAMPs molecules, which are phagocytosed or recognized and processed by TAMs and TADCs cells at the tumor. Further TAMs and TADCs migration from the tumor to the lymph nodes of the immune system proceed with maturation of those cells. c) Next, mature TAMs and TADCs switch their phenotype into antigen presenting cells (APCs). In turn, the mature APCs can produce inflammatory cytokines, activating the innate immune system response (T-cell response). In another way, APCs present tumor antigens to activate the response of NK cells and adaptive immune system cells. The same mechanism applies for any other thermal therapy which uses any other heat mediators or strategies to increase the temperature.

Currently, two clinical trials (NCT03757858 and NCT03393858) have combined immunotherapy and hyperthermia treatment at phase I/II validation but neither of them involves the use of MNPs for actuation by AMF.[415] The use of MNPs along with MHT stimulation in combination with immunotherapy has emerged during the last two decades as a promising approach for providing more specificity to the treatment (so-called thermos-immunotherapy), due to the possibility to increase the temperature only at the tumor target site, thus promoting a more efficient heat release and a local immune system stimulation.[416]

Notably, in one of the first MHT studies for the treatment of Gbm patients,[417] it was found that following the intratumoral injection of MNPs, patients exposed to MHT at a therapeutic temperature of 49.5 °C, presented a larger number of macrophages at the tumor with respect to patients that received the intratumoral injection with MNPs but were not exposed to AMFs. The evidence of activation of immune response by MHT on patients has been subsequently supported by several studies in animal models.[418-420] These studies not only proved that the treatment of a primary tumor with MHT could induce inhibition of tumor growth at a distant tumor (abscopal effect), but also provided insights on the intrinsic molecular mechanisms involved in the immune system activation by MHT application (Figure 15).

More recent studies have also highlighted the action of SPIONs *per se* (without MHT application), to inhibit the tumor growth by inducing a pro-inflammatory macrophage polarization.[421] This immunomodulator action could be further enhanced depending on the type of the nanoparticle surface coating.[421]

Based on these evidences, the use of MNPs as nanoplatforms for combining MHT and immunotherapy has been on the rise in the very last years. Among the different mechanisms that have been exploited for the activation of the immune system in combination with MHT, four main strategies have been identified and there will be described in the next paragraph (Figure 16).[416]

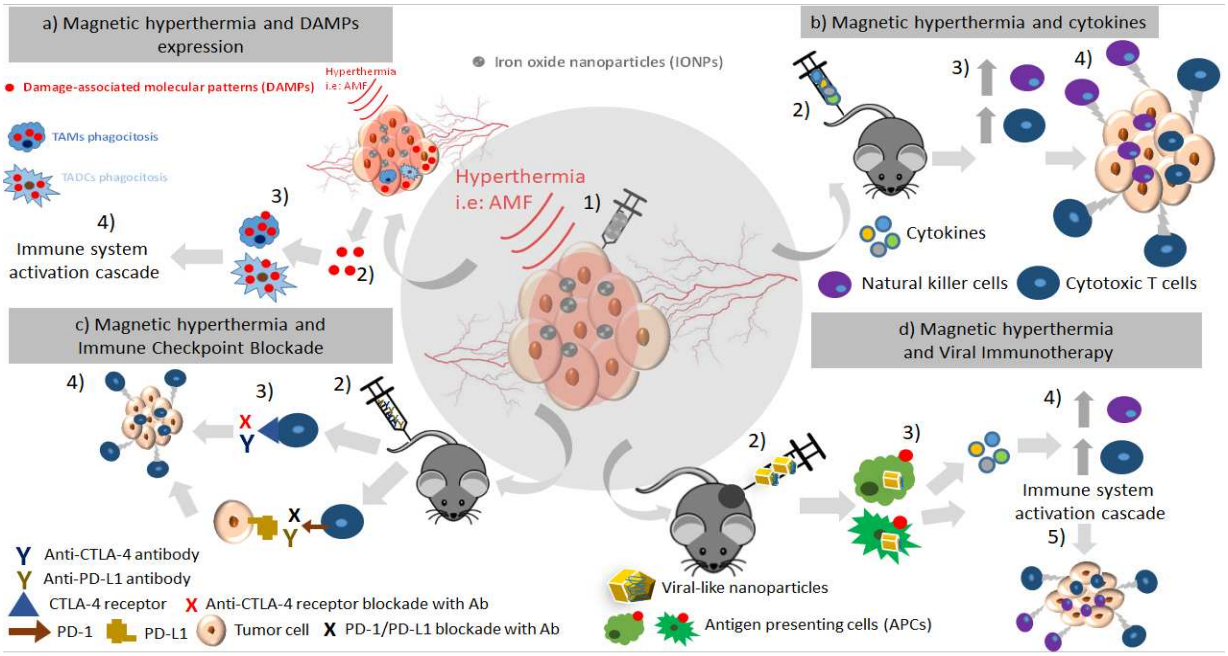

Figure 16. Summary of strategies to combine MHT and immunotherapy based on a) DAMPs expression; b) immunostimulators, c) immuno check point blockade and d) cancer vaccines.

9.2 Relevant *in vivo* studies for the combination of immunotherapy with MHT.

9.2a Magnetic hyperthermia and DAMPs expression Among DAMPs, heat shock proteins (HSPs) are a family of proteins produced by cells in response to stress conditions.[422, 423] The expression of HSPs on cancer cells has been implicated in mediating resistance to cytotoxic effects of hyperthermia [424] and supporting, at the same time, the malignant phenotype of cancer cells not only affecting cell survival, but also participating in angiogenesis, invasion, metastasis and immortalization mechanisms.[425] On the other hand, the immune system has evolved to take advantage of the expression of HSPs recognized as 'danger signals' for generating a sustained immune response.[426] Indeed, HSPs released from necrotic cells, activate immature dendritic cells (DCs) by their recognition, inducing them to transform into mature dendritic cells or antigen presenting cells (APCs) thus activating the cascade immune response as described above.[427]

Taking advantage of the HSPs recognition by immune system, Sato *et al*.[428] exploited MHT as a remote physical stimulus and induce the HSPs expression by cancer cells. For this purpose, silane-coated Fe_3O_4 nanoparticles (10 nm), were functionalized with N-propionyl-4-S-cysteaminylphenol, a melanogenesis substrate that enhances internalization by melanoma cells. Upon intratumoral injection of MNPs on a xenograft tumor model (B16-OVA cell line) the MHT treatment (118 kHz and 30.6 $kA \cdot m^{-1}$ for 30 minutes) enabled to maintain a tumor temperature of 43°C. Next, as a consequence of tumor cell necrosis and HSPs expression, the DCs activation was verified and tumor growth volume suggested a complete cure for mice exposed to MHT. Notably, by re-inoculating the cured mice subcutaneously with B16-OVA cells on the opposite flank, no secondary tumors were regrowing. By observing this abscopal

effect, the authors concluded that targeting-MHT might be effective not only for primary melanoma treatment but also for the treatment of distant metastasis thanks to induction of systemic antimelanoma immune responses mediated by specific anti-tumor- cytotoxic T lymphocytes production.[429]

In another study the expression of HSPs MHT-mediated was combined with the expression of HSP70 mediated by gene therapy.[430] For this purpose, a plasmid carrying human-inducible HSP70 cDNA was used to transfect cancer cells in a xenograft melanoma tumor model (B16 cell line), using *in situ* lipofection. Cell transfection was followed by intratumoral injection of 10 nm Fe_3O_4 nanoparticles coated by cationic liposomes (a lipid mixture consisting of N-(a-trimethylammonioacetyl)-didodecyl-d-glutamate chloride, dilauroylphosphatidyl-choline, and dioleoylphosphatidyl-ethanolamine). Tumor free cured mice and prolonged animal survival were found only in the animal group that besides plasmid and MNPs injection, received also the MHT (118 kHz and 30.6 kA/m) treatment, reaching a therapeutic temperature of 43°C. The over-expression of HSP70 and the immune response activation were the main factors involved in the complete tumor regression. In line with these findings, Tanaka *et al*.[431] used similar MNPs-cationic liposome, exploited the injection of immature DC cells after MHT treatment (118 kHz frequency and a field of 30.6 kA/m), as intermediate cells of the immune system to re-awake the immune response cascade. Interestingly, for mice exposed to MHT and intratumoral injection of immature DC cells, an increase of the activity of cytotoxic lymphocytes and natural killer cells was observed, which could be clearly correlated to the DCs activation mediated by HSP of necrotic tumoral cells upon MHT heat exposure.

Contrary to the HSP70 overexpression strategy, another group exploited gene therapy to downregulate HSP70. [272] An ovarian orthotopic tumor model (HeyA8 or A2780cp20 cell lines) was intraperitoneally injected with liposomes loaded with siRNA against HSPA6, which encodes for Hsp70 protein. Subsequently, magnetic nanoliposomes (based on 1,2-dioleoyl-sn-glycero-3-phosphatidylcholine and dextran-coated iron oxide MNPs) were used to perform MHT treatment, reaching a temperature of 43°C at the tumor. The treatment group where the downregulation of Hsp70 was combined with MHT had the most significant tumor regression. The efficacy of the treatment was ascribed to the lack of Hsp70 protein (a "shield" effects against thermal stress) that increased the tumor vulnerability to heat and the consequent immune cascade. Furthermore, in a different study the role calreticulin as DAMP agent was evaluated in combination with MHT. Here, Beola *et al*[414] . intratumorally injected oleic acid-coated iron oxide nanoparticles (11 nm, 0.15 mg Fe/tumor) in a xenograft pancreatic tumor model (MIA PaCa-2 cells) and apply MHT treatment(196 kHz; 26 kA/m). The authors reported that calreticulin release was significantly enhanced in tumor cells that received MNPs and were exposed to MHT, and was able to trigger DCs maturation and cytotoxic T-lymphocyte activation.

9.2b Cytokines and MHT. Cytokines are a class of proteins functioning as signaling molecules to mediate and regulate immunity and inflammation by increasing the activity of cytotoxic T lymphocytes. Interferon (IFN) based family, tumor necrosis factors, colony stimulating factors and interleukins (IL) such as IL-2, IFN-α, IFN-β and occasionally IFN-γ, IL-6, IL-12, belong to cytokines used in anti-cancer treatment.[432] Clinical trials using cytokines as immunotherapeutics failed to meet the expectations raised in preclinical studies due to some critical limitations such as the short half-life of most cytokines and the consequent narrow therapeutic windows with only modest anti-tumor efficacy.[433] Inspite of their scarce efficacy as monotherapy, the combination of cytokines with other therapeutic modalities (i.e. MHT) may represent a more effective strategy. Ito *et al.* [434] combined MHT with immuno-stimulation choosing interleukin-2 (IL-2) as a potent stimulator of lymphocyte proliferation while augmenting the activity of cytotoxic T lymphocytes.[435] For this purpose, magnetite cationic liposomes based on Fe_3O_4 nanoparticles

(10 nm) were intratumorally injected in a xenograft melanoma mouse model (B16 cell line), followed by the intratumoral administration of either IL-2 or GM-CSF and subsequent exposure to MHT (*f*=118 kHz and H= 30.6 kA·m^{-1} for 30 minutes at 43 °C).[430] It was demonstrated that IL-2 and granulocyte-macrophage colony-stimulating factor (GM-CSF) act as cytokines after having applied MHT.[434] In addition, a complete tumor regression was observed in those mice receiving MHT after the injection of MNPs and immunomodulators (either IL-2 or GM-CSF). Enhancement of APCs, namely the H-2 antigen, on B16 melanoma cells, was correlated to the enhancement of the cytotoxic T-lymphocyte response. Furthermore, the GM-CSF cytokine played an important role in the maturation and function of APCs, and proved also to be a powerful immunostimulant after MHT.[436] Along with the choice of frequency, amplitude and time parameters for an efficient MHT, also the temperature at which the treatment is performed represents a relevant factor to consider in terms of immunostimulation. Toraya-Brown *et al*. demonstrated that local hyperthermia at 43 °C (*f*= 167.5 kHz, H = 35.8-43.7 kA.m^{-1} for 30 minutes), was able to activate DCs and CD8+ T cells and conferred resistance to tumor rechallenge in melanoma mouse model treated with starch-coated IONPs.[437] The same therapeutic effect could not be obtained when a MHT treatment at 45 °C was performed. This was due to the heat-deactivation of antigens, chemokines and cytokines that mediate the immune system response. On the other hand, the use of a specific temperature to trigger the effect of immunomodulatory substances can further enahnce local immune-response. Alphandéry *et al.* for instance, observed the recruitment of neutrophils at glioma tumor mass when treating the tumor with magnetosomes chains (i.e. magnetic iron oxide nanoparticles produced by magnetobacteria) associated to endotoxin, an immune-stimulating substance. The endotoxin release from the magnetosome surface under MHT, could widely diffuse at the tumor site stimulating the neutrophils to infiltrate the tumor. On the contrary, the sole presence of magnetosomes - endotoxin (in absence of MHT) was not as efficient to induce infiltration of the immune cells, thus underlying the crucial role of external AMF as a tool to locally induce immune response.[438]

9.2c) Immune Checkpoint Blockade and MHT. Immune checkpoint inhibitors are a class of drug that blocks proteins called checkpoints, which are expressed on the surface of some types of immune system cells, such as T cells and, in some cases, on some cancer cells. On immune cells, these checkpoints have the physiological action to self-tune immune responses (preventing the boost of immunoaction in healthy conditions). Instead in a pathological condition, they help T cells to kill cancer cells thus generating a durable tumor reduction and long-standing tumor immunity.[432] Tumor cells, on the other hand, may evade immune recognition directly by downregulating or upregulating features that make them vulnerable to inhibitory receptors such as PD-1 and CTLA-4.[439] Immune Checkpoint Blockade therapy is based on, first, the identification of biomarkers of immune checkpoint blockade and later on the use of antibody therapy with blockade antibodies (i.e. anti-PD-1/anti-PD-L1, anti-CTLA4) to either unleash the immune system or to render the tumor cells more vulnerable to the immune-response.

CTLA-4 is a receptor expressed on CD4+ T cell surface that inhibits T cell functions.[440] Indeed it mediates immunosuppression through the binding to a co-stimulatory ligand (CD28), reducing T cell immune signaling (avoiding autoimmune diseases). The development of specific anti-CTLA4 antibodies could activate T cell response against the tumor, inhibiting the immunosuppression action of cancer.[440] Chao *et al.*,[441] proposed a combined strategy based on MHT and immune checkpoint blockade based on the administration of antibodies anti-CTLA-4 receptor. For this study, iron oxide nanoparticles (30-50 nm) coated with polyethylene glycol/dopamine were co-encapsulated into poly(lactic-co-glycolic) acid capsules with Imiquimod, an immune adjuvant that can locally recruit DCs. The intratumoral injection of magnetic nanocapsules and the MHT treatment (Hf = 1.2 × 10^9 A m^{-1}s^{-1}, reaching a temperature of 50−52

°C), was followed by a systemic injection of (anti-CTLA4) checkpoint blockade antibodies, resulting in a systemic therapeutic response with a complete primary tumor regression only when treated with MHT. Moreover, the decrease in the tumoral volume of the contra-lateral tumor flank clearly indicated the tumor inhibition of distant metastasis (abscopal effect) which was attributed to a robust immune memory effect that enable recognition and destructions of the distant tumor.

In a more complex study, Wang *et al*.[442] successfully exploited the combination of dual thermotherapy based on MHT and PDT with immunotherapy based on Immune Checkpoint Blockade inhibitors for the same target CTL-4. For this study, Janus structure-like nano-bullets with an head consisting of spherical Fe_3O_4 coated with mesoporous silica and a body structure made of disulfide-bridged mesoporous silica framework (250 nm × 100 nm) was developed. The chlorine e6 (Ce6), a widely used photosensitizer in PDT, was encapsulated into the mesoporous silica which was designed to degrade in acidic and reductive environment, thus tuning the release of Ce6 photosensitizer intracellularly. In order to check the effectiveness of the combined therapy, an orthotropic 4T1 (breast cancer) mouse model was developed and Janus nano-bullets were intravenously injected in multiple injections, followed by a treatment of MHT (25.8 $kA.m^{-1}$, 262 kHz, 20 min) and laser irradiation (660 nm, 0.15 Wcm^{-2}, 10 min). Moreover, every 4 days, intraperitoneal injection of CTLA-4 antibodies was ensured. The combined treatment (MHT+PDT+Anti-CTLD-4 antibody) was markedly better than either of the individual treatments (only MHT or only laser) to completely eradicate the primary tumor and, also, to prevent the metastasis development. Indeed, the hyperthermia-induced immunogenic cell death signals (both for MHT and PDT) facilitated the DCs maturation, while the anti-CTLA-4 antibodies enhanced the cytotoxic response of T lymphocytes.

PD-1 is another checkpoint protein present on immune cells T cells, acting as a “switch off” signal that prevents T cells from attacking healthy cells in the body (auto-immune response). When PD-1 binds to the corresponding ligand, PD-L1, it sends an instruction to T cells in order to avoid T cells attacking the target cell. Some cancer cells have evolved to present large amounts of PD-L1 molecules, which helps them hide from an immune attack. Anti-PD-L1 antibodies by binding to T cells can block the binding between PD-1 on T cells and PD-L1 on cancer cells, making tumoral cells susceptible again to immune attack.[443]

Liu *et al*.,[443] exploited intratumoral injection of PEGylated vortex-domain iron oxide nano-rings (∼150.9 nm) for MHT (at f = 365 kHz, H not reported, multiple cycles every 2 days) on an orthotopic 4T1 breast tumor. Next, anti-PD-L1 antibody was intraperitoneally injected on alternate days. It was observed that mild thermotherapy eradicated the primary tumors treated due to the heat damage while at the same time by sensitizing tumors to the PD-L1 checkpoint blockade promoted an 88% increase of cytotoxic CD8+ T lymphocyte infiltration in distant tumors and triggered immunotherapy. The authors proved that the combination treatment also inhibited the immunosuppressive response of the tumor, as evidenced by a significant down-regulation of myeloid-derived suppressor cells, which mainly, suppress antitumoral T cell. Moreover, by generating systemic antitumor immunity overtime, the authors concluded that the combination treatment prevented distant tumor progression in an abscopal tumor model.

More recently Hu *et al*.,[373] in a bilateral murine model of 4T1 breast cancer, intratumorally administered $CoFe_2O_4$@$MnFe_2O_4$ nanoparticles for treatment with AMF (f not reported, 1.35 kA/m to reach 50 °C). For the tumor immunotherapy, α-PD-L1 antibodies were intravenously injected on successive days after MHT primary tumor treatment. Authors concluded that MHT ablation of primary tumors could generate tumor-associated antigens that initiate the DC cascade and cytotoxic T cells while the α-PD-L1 treatment, effectively prevents the tumoral immune suppression microenvironment for T

cells and thus significantly increases the number of infiltrating T cells in distant tumors promoting an effective inhibition of metastatic tumors.

9.2d) Viral immunotherapy and magnetic hyperthermia Viral immunotherapy, which comprises retroviral vectors, adeno-associated viral vectors, recombinant vaccinia viruses and oncolytic viruses may represent a valid alternative immunotherapy method.[444] Indeed, the possibility to modify the viral surface with tumor-homing molecules, together with the delivery of the desired coding sequences for immunotherapy purposes, constitute the main advantages of viral vectors as therapeutic delivery vehicles.[445] By replacing or inactivating the viral genetic material, viral vectors may be armed with genes able to enhance immunogenicity, such as tumor antigens or co-stimulatory effectors, and may be used to induce systemic antitumor immunity via innate immune system pathway like STING-Batf3 axis.[446] To further enhance the immune response, the protein shell of the VLP can be further engineered to incorporate the expression of specific proteins, such as APCs proteins that further help to trigger the immune response.[447] To combine MHT and viral immunotherapy, Hoopes *et al*.[447] treated a spontaneous canine tumor model with a two-injections approach where first commercially available iron oxide MNPs (40 nm in core size), coated with a shell of hydroxyethyl starch or dextran, were intratumorally administered to perform MHT, followed by injection of virus-like particles (VLPs). [447] VLPs derived from inactivated virus where engineered in order to express viral proteases and VP60 capsid proteins. In detail, MNPs (corresponding to 140 ug Fe) were intratumorally injected and exposed to MHT (f= 150 kHz and H= 400 Oe) in order to reach a temperature of 43 °C.. The subsequent intratumoral injection of VLPs (28 nm,100 μg/200 mm^3 tumor) not only resulted in a significant primary tumor regression but also induced systemic immune reaction, demonstrating abscopal effect. Notwithstanding the promises hold by viral immunotherapy, immune responses to viral vectors may also limit the efficacy of these delivery systems and appropriate dosage schedules, routes of administration and capsid modifications, should be planned to ameliorate their efficacy as well as to increase their safety.[448]

10. Future perspectives

MHT and its combination with other therapeutic modalities hold great promises to significantly advance the field of cancer treatment. Based on the characteristics of the cancer, in the near future, one may be able to select the most appropriate combination of MHT-heat based cures to suit the need of the patient treatment according to a personalized medicine approach. Up to date, at clinically relevant conditions of the MHT treatment, majority of proof-of-concept preclinical studies have proved successful only for local intratumoral therapy of primary tumor. Among the MNP-platform applied intratumorally, the hydrogel-based system is perhaps one of the most interesting candidates as this system shows versatile features to be easily implemented for the delivery of different therapeutic agents rather than chemotherapy as now exploited, with precise control of the dose. On the other hand, there is still much more room for the development of an advanced MHT therapy based on the systemic administration of MNPs, which will enable, in future, to treat metastasized tumors. For this purpose, having magnetic nanosystems that are able to home at the tumor and to enable MHT and other combined therapies in a specific and efficient manner represents still a big challenge to be addressed. In this direction many points need to be pursued: i) the intravenous delivery of the right dose of MNPs for a mild or a harsh MHT at the tumor; ii) the profoundly understandings of the synergistic mechanism using combined treatment and how these mechanisms are correlated to a specific tumor type; iii) the measurement of the temperature of the particles at the tumor as a function of the dose accumulated; iv) the quantification of MNPs at the

metastasized tumor; v) the need of new clinical instrumentation needed to select and localize the AMF treatment thus reducing off-target side effects; vi) the design of MNPs that can slowly degrade and be eliminated by the body with no toxic effects and within a reasonable time frame (months), to enable tumor monitoring with routinely applied clinical MRI techniques.

To accomplish to these needs, some major considerations may be worth to be highlighted to shape the future direction of material design towards such novel therapeutic models.

First, for the **accumulation of the right doses** of nanoparticles for MHT at metastasis new strategies to deliver the right dose of MNPs are required. New opportunities may use of immune-system cells (macrophages, T-cells, NK-cells, dendritic cells) as carrier tools to deliver the MNP-based platform given their spontaneous tendency to circulate, recognize and home at the tumor. Alternatively, the exploitation of asymmetric shape of micro-containersdelivery MNPs may further improve the preferential accumulation of platforms at the specific organs/tumors also represents an interesting approach to pursue. In addition, the design of bio-molecular functionalized MNP that can recognize and selective target the tumor prolonging their permanence at the tumor while avoiding their clearance represents another route. In this same direction, a combined multimodal therapeutic approach may also contribute due to the synergic cytotoxic effects to reduce the dose of MNPs needed to obtain their therapeutic effects. For instance, the use of remote heat triggered chemotherapy/immunotherapy may mediate a more effective localized therapy enabling to reduce side effects while providing distant whole-body protection by enrolling the immune-system cells. In this direction, while very basic proof-of-concept studies have been provided, the design and realization of multitasking MNP-based platform with advanced actuation and response requires still work to do and may provide an unprecedented opportunity for personalizing the medical treatment. In this same direction, also a better exploitation of toxic MNPs compositions associated to the tuning of the MNP degradation kinetic with the controlled release of toxic ions maybe be further exploited in combination with other MHT-mediated phenomena such as the alignment of nanoparticles associated to mechanical damage;[167] the promotion of Fenton reaction for the catalysation of ROS production,[449] the auto-immune response evaluation of some MNP compositions,[421] the reoxygenation of cancer tissue etc.[263] These will be needed to be further investigated for different MNP compositions different from iron oxide.

In this line, in order **to reduce as much as possible the dose of MNPs**, optimal MNPs are needed. In this sense despite the outstanding MHT heat performances reported, just few MNPs maintain such outstanding heat dissipation at magnetic field conditions that are of clinical use for MHT. Moreover, MNPs should preserve this feature not only in aqueous solution but under tumor microenvironment conditions. Therefore, the development of MNPs showing a viscosity-independent and an aggregation-independent MHT-heating capacity should be aimed and characterization studies under these conditions should be standardly implemented to compare with state-of-the-art systems and to select MNP materials for MHT. In this sense, in order to have an optimal heat efficiency at the tumor site, it is interesting the possibility to use MNPs with a dominant Néel (viscosity-independent relaxation mechanism). In alternative, the pre-assembling of MNPs in an optimized fixed configuration, for guarantee a viscous independent SAR behaviour once reaching the tumor area are also novel concepts to be further pursued to exploit to preserve optimal heat release at the tumor site. Lastly, MNPs having a proper size and optimal targeting ligand have demonstrated to accumulate more efficiently at the tumor but in particular, the anchoring *via* ligand-receptor to the tumor associated tissues avoid their clearance as compare to MNPs that do not bear selective tumor targeting molecules.[450] Apart from that, such coating should possess the capability to load a sufficient amount of molecules or nanocrystals that enable different therapeutic model besides

MHT. In particular, for the case of chemotherapy, the coating is expected to enable the loading of bio-macromolecules coupled with the feature of heat-triggered release which is highly desired as it minimized the side effect of loaded drugs. Meanwhile, in the case of RT, the capability of loading radioisotopes could open new vistas for the combinatorial therapies as it would allow to completely remove external physical stimuli (external beam radiation)[451] thus accessing deep-seated tumors and also will enable nuclear imaging thus providing image guidance for targeted magnetic hyperthermia.[452-454] In this respect, the hybrid materials made of polymer and MNPs perhaps stand out as most promising candidate as the structure of polymer can be tailored to meet not only the demand for a stable coating but also the possibility to assemble MNPs and other inorganic nanoparticles to form novel nanostructures showing unprecedented properties in term of MHT and magnetic response. This, in turn, will leverage the performance of the resulting materials. Finally, MNPs at different shapes, such as nanocube, nanostarts, rod-like nanoparticles, may impact not only the MHT heat performance and, in turn, the combinational therapies by requiring less chemotherapeutic drug agents and nanoparticle doses to achieve the same therapeutic index, but they will also impact the biodistribution and clearance of the magnetic core materials.[455] Indeed, as shown for nanocubes,[456] the presence of edges in the nanocubes and nanostars, which are more difficult to polymer coating in contrast to the flat curvature of spherical MNPs, may affected the degradation profiles of the nanocubes under intracellular/intratumoral environment.[456]

Second, from a practical viewpoint, **MHT should rely on robust scale-up approaches** that fulfil the clinic needs in terms of material production and safety while maintaining the quality and features of the same nanoparticles, including the heat dissipation. Although MNPs produced by non-hydrolytic routes have shown unprecedented MHT performances, the large-scale production of efficient MNPs for MHT through this route is less feasible and it has not been demonstrated to date. The development of synthetic pathways merging the best of each non-hydrolytic and hydrolytic approach could be of great interest. These methods should also respect good laboratory practice and quality of the MNP products for human health. Moreover, for the preparation approaches environmental and economical sustainability criteria should be taken into account with the attempt to develop MNP-nanoplatform preparation that are green and economically sustainable (use for instance of drugs molecules that are FDA approved and not anymore under patent protections, use of abundant polymers or physiological liposome compositions when possible, etc.).[159 457] In this direction, liposomes have been so far the most successful nanomedical formulation thanks to their fully compatibility and physiological membrane-like composition, scalability, high drug loading capacity and versatility. However, the challenges pose by the fine synthesis process to obtain stable TMLs for prolonged blood circulation time , capable of inducing mild hyperthermia and cargo release only when activated (*i.e.* preventing any unspecific drug leakage), are still many and need to be addressed. The recent success of the mRNA vaccines based on liposomic formulation developed by Pfizer/Biontech and Moderna, indicates that likely, in the near future, magnetic liposomes will still have even a greater impact in the next pharmaceutical formulation for MHT applications, thus possibly opening new ways to the investigation and application of TMLs in several diseases.

Third, **for the monitoring of the temperature raise** at the tumor, the development of advanced nanotheranostic tools may offer new solutions for an intratumoral measure. In this regards the use of temperature-dependent NIR-species such as metal chalcogenide quantum[462-465] dots or rare-earth metal doped[466, 467] nanoparticles having emission spectra features that are temperature dependent, may represent a NIR-fluorescence tool for the *in vivo* readout of the temperature at the tumor when co-assembled/associated with MNPs. In alternative, some attempts to quantify the temperature in hyperthermia based on a temperature dependent MRI signals of tissue protons have been investigated[468]

but still optimization of the system would require further work and in case of MNPs the interference with the nanoparticle signal may represent a challenge or on the contrary an opportunity. Alternatively, the use of smart software that can help to simulate temperature profiles based on input parameters of MNPs could offer an alternative solution and would require further development.[230]

Fourthly, for the **quantification of MNPs at the tumor**, the emerging MPI modality has shown the potential to quantify the amount of MNPs in the tumor after an injection,[469-471] which would allow controlling the power needed to reach a therapeutic temperature or *vice versa* to decide the temperature of the therapeutic treatment and thus vary the heat power dissipation for a given frequency. In addition, very recent studies have opened to the possibility to use of the MPI gradients for spatial localization of MHT to arbitrarily selected regions. The possibility to focalize MHT treatment addresses a key challenge of conventional magnetic hyperthermia because iron oxide particles systematically tend to accumulate in non-specific organs (e.g., liver and kidneys), which could be damaged under the whole-body application of AMFs.[472, 473]

Finally, for **the need to use MRI diagnostic tools after MHT treatment** to monitor the tumor progression, the use of degradable MNPs that can be slowly eliminated by the body (within few months) would represent an opportunity to still perform MHT/multi-therapeutic action in the first months after MNP injection but then, their clearance would facilitate the monitoring of the tumor developments using standard tools. Also, so far most of the clinical trials were based on the intratumoral administration of MNPs and therefore more studies monitoring the MNPs will be required to assess their accumulation, bio-distribution and excretion upon intravenous injection. Finally, another challenging topic worth to study at the pre-clinical level is the clearance of MNP compositions other than iron oxide, like metallic iron, or Au-iron oxide/Ag-iron oxide heterostructures.

List of abbreviations

Abbreviation	Meaning
2D	Bi-dimensional
2D-MNBs	bi-dimensional Magnetic clusters
3D	Three dimensional
3D-MNBs	three dimensional magnetic nanoclusters
A	Area of Hysteresis Loop
AF	Antiferromagnetic
AMF	Alternating Magnetic Field
APCs	Antigen-presenting cells
Ce6	Chlorine e6
CH	Cholesterol
Chito-FIONs	chitosan oligosaccharide-conjugated ferrimagnetic iron oxide nanoparticles
chitosan-DOPA	chitosan oligosaccharide-conjugated with L-3,4-dihydroxyphenylalanine
CMC	critical micellar concentration
cMNPs	Concentration of magnetic nanoparticles
CoFe	Co-ferrite

CoMn-IONPs	cobalt and manganese doped hexagonal iron oxide nanocrystals
$C_{p,s}$	Heat capacity of the sample
CPPs	Cell penetrating peptides
CT	Computed Tomography
CTLs	CD4+ T lymphocytes, CD8+ T lymphocytes
D	Diameter
DAMPs	Damage-associated molecular patterns
DCs	Dendritic cells
DDAB	dimethyldioctadecyl ammonium bromide
d_H	hydrodynamic size
d_{opt}	Optimal diameter
DOXO	Doxorubicin
DPPC	1,2-dipalmitoyl-sn-glycero-3-phosphocholine
DSPC	Distearoylphosphatidylcholine
DSPE-MPEG2000	1,2-diacyl-SN-glycero-3-phosphoethanolamine-N-[methoxy(poly(ethyleneglycol))-2000]
DSPE-PEG2000	1,2-distearoyl-sn-glycero-3-phosphoethanolamine N [carbonyl-methoxy (polyethylene glycol)-2000]
E_a	Anisotropic Energy
EGFR	epidermal growth factor receptor
EPR	Enhanced passive retention
EPR	Enhanced passive retention
EtOH	Ethanol
f	Frequency
f	Magnetic frequency
f0	Frequency Factor
FDA	Food and Drug Administration
Fe_3O_4	Magnetite nanoparticles
FeO/Fe_3O_4	wüstite-magnetite core-shell
FM	Ferrimagnetic
Gallol-PEG	gallic-functionalized poly(ethylene glycol)
GBM	Glioblastoma Multiforme
GM-CSF	Granulocyte-macrophage colony-stimulating factor
H	Magnetic Field
H_{AC}	Applied alternating magnetic field
H_c	Coercivity
HSPC	hydro soy PC L-α-phosphatidylcholine
HSPs	Heat shock proteins

IFN	Interferon
IL	Interleukins
IL-2	Interleukin-2
ILP	Intrinsic Loss Power
IONCs	iron oxide nanocubes
IONPs	Iron oxide nanoparticles
K	Anisotropy constant
k_b	Boltzmann constant
LRT	Linear Response Theory
LSMO	lanthanum strontium manganate
m	Magnetic Moment
M	Magnetization
M(H)	Magnetic hysteresis
MHT	Magnetic Hyperthermia
MNB	Magnetic Nanobead
$MnFe_2O_4$	Manganese ferrite nanoparticles
MNP	Magnetic Nanoparticle
MPI	Magnetic Particle Imaging
Mr	Remanent Magnetization
MRI	Magnetic Resonance Imaging
Ms	Saturation Magnetization
MSPC	1- stearoyl-2-hydroxy-sn-glycero-3-phosphocholine
N.A.	Not Assessed
ND-PEG-COOH	α-Nitrodopamine-ω-carboxypoly(ethylene glycol)
NIR	Near infrared
NK	Natural killer cells
Oligo-PHA	Oligo polyhydroxyalkanoate
P	Dissipation Power
PA	Palmitic acid
PC18	Poly(maleic anhydride-alt-1-octadecene)
PDT	Photo-dynamic therapy
P_e	Eddy current
PEG 400	Poly(ethylene glycol) 400
PEG−PCL	poly(ethylene glycol)-b-poly(ε-caprolactone
PET	Positron Emission Tomography
PScMA	polystyrene maleic anhydride cumene terminated
PTT	Photo-thermal Therapy
PTX	Paclitaxel
QD	Quantum dot

RT	Radiotherapy
SA	stearylamine
SAR	Specific Absorption Rate
SEC	Size-exclusion cromatography
SiO_2	Silicon dioxide
SLP	Specific Loss Power
SPION	Superparamagnetic Iron Oxide Nanoparticle
T	Temperature
t	Measurement timescale
TADCs	Tumor associated dendritic cells
TAMs	Tumor associated macrophages
T-cells	T-Lymphocytes
TD	Thermal decomposition
TEM	Transmission electron microscopy
TEOS	tetraethyl orthosilicate
TMLs	thermosensitive magnetic liposomes
V	Volume
VLPs	Virus-like particles
ΔT	Temperature increase
η	Viscosity
ρ	Density
τ	effective relaxation
τ_B	Brownian motion
τ_N	Néel relaxation
χ	Susceptibility
χ''	Loss component of susceptibility

Aknowledgments

This review is partially funded by the European Research Council-proof of principle: ERC-POC HYPERCUBE(Contract No. 899661 tp T.P.) and by the AIRC Foundation (AIRC IG-14527 to T.P.).

11. References

1. D. Ortega and Q. A. Pankhurst, *Nanoscience*, 2013, **1**, e88.
2. E. A. Périgo, G. Hemery, O. Sandre, D. Ortega, E. Garaio, F. Plazaola and F. J. Teran, *Appl. Phys. Rev.*, 2015, **2**, 041302.
3. S. V. Spirou, M. Basini, A. Lascialfari, C. Sangregorio and C. Innocenti, *Nanomaterials*, 2018, **8**, 401.
4. K. Mahmoudi, A. Bouras, D. Bozec, R. Ivkov and C. Hadjipanayis, *Int. J. Hyperthermia*, 2018, **34**, 1316-1328.
5. M. Levy, A. Quarta, A. Espinosa, A. Figuerola, C. Wilhelm, M. García-Hernández, A. Genovese, A. Falqui, D. Alloyeau and R. Buonsanti, *Chem. Mater.*, 2011, **23**, 4170-4180.

6. I. Conde-Leboran, D. Baldomir, C. Martinez-Boubeta, O. Chubykalo-Fesenko, M. Del Puerto Morales, G. Salas, D. Cabrera, J. Camarero, F. J. Teran and D. Serantes, *J. Phys. Chem. C.*, 2015, **119**, 15698-15706.
7. N. Gehrke, D. Heinke, D. Eberbeck, F. Ludwig, T. Wawrzik, C. Kuhlmann and A. Briel, *IEEE Trans. Magn.*, 2015, **51**, 1-4.
8. I. M. Obaidat, B. Issa and Y. Haik, *Nanomaterials*, 2015, **5**, 63-89.
9. L. M. Bauer, S. F. Situ, M. A. Griswold and A. C. S. Samia, *Nanoscale*, 2016, **8**, 12162-12169.
10. D. F. Coral, P. Mendoza Zélis, M. Marciello, M. D. P. Morales, A. Craievich, F. H. Sánchez and M. B. Fernández Van Raap, *Langmuir*, 2016, **32**, 1201-1213.
11. E. Myrovali, N. Maniotis, A. Makridis, A. Terzopoulou, V. Ntomprougkidis, K. Simeonidis, D. Sakellari, O. Kalogirou, T. Samaras and R. Salikhov, *Sci. Rep.*, 2016, **6**, 37934.
12. P. De la Presa, Y. Luengo, M. Multigner, R. Costo, M. Morales, G. Rivero and A. Hernando, *J. Phys. Chem. C.*, 2012, **116**, 25602-25610.
13. M. Cacciola and M. Osaci, *IOP Conference Series: Materials Science and Engineering*, 2015, **85**, 012021.
14. R. Di Corato, G. Béalle, J. Kolosnjaj-Tabi, A. Espinosa, O. Clement, A. K. Silva, C. Menager and C. Wilhelm, *ACS nano*, 2015, **9**, 2904-2916.
15. M. V. Zyuzin, M. Cassani, M. J. Barthel, H. Gavilan, N. Silvestri, A. Escudero, A. Scarpellini, F. Lucchesi, F. J. Teran and W. J. Parak, *ACS Appl. Mater. Interfaces*, 2019.
16. J. Carrey, B. Mehdaoui and M. Respaud, *J. Appl. Phys.*, 2011, **109**, 083921.
17. B. Mehdaoui, A. Meffre, J. Carrey, S. Lachaize, L. M. Lacroix, M. Gougeon, B. Chaudret and M. Respaud, *Adv. Funct. Mater.*, 2011, **21**, 4573-4581.
18. C. L. Dennis and R. Ivkov, *Int. J. Hyperthermia*, 2013, **29**, 715-729.
19. H. Mamiya, *J. Nanomater.*, 2013, **2013**.
20. E. Lima, E. De Biasi, R. D. Zysler, M. V. Mansilla, M. L. Mojica-Pisciotti, T. E. Torres, M. P. Calatayud, C. Marquina, M. R. Ibarra and G. F. Goya, *J. Nanopart. Res.*, 2014, **16**, 2791.
21. D. Cabrera, J. Camarero, D. Ortega and F. J. Teran, *J. Nanopart. Res.*, 2015, **17**, 121.
22. U. M. Engelmann, C. Shasha, E. Teeman, I. Slabu and K. M. Krishnan, *J. Magn. Magn. Mater.*, 2019, **471**, 450-456.
23. O. Grauer, M. Jaber, K. Hess, M. Weckesser, W. Schwindt, S. Maring, J. Wolfer and W. Stummer, *J. Neurooncol.*, 2019, **141**, 83-94.
24. G. F. Goya, L. Asín and M. R. Ibarra, *Int. J. Hyperthermia*, 2013, **29**, 810-818.
25. R. Thomas, I.-K. Park and Y. Y. Jeong, *Int. J. Mol. Sci.*, 2013, **14**, 15910-15930.
26. W. Aadinath, T. Ghosh and C. Anandharamakrishnan, *J. Magn. Magn. Mater.*, 2016, **401**, 1159-1172.
27. A. V. Apkarian, R. A. Stea and S. J. Bolanowski, *Somatosens. Motor Res.*, 1994, **11**, 259-267.
28. M. Johannsen, U. Gneveckow, L. Eckelt, A. Feussner, N. Waldöfner, R. Scholz, S. Deger, P. Wust, S. Loening and A. Jordan, *Int. J. Hyperthermia*, 2005, **21**, 637-647.
29. M. Johannsen, U. Gneveckow, B. Thiesen, K. Taymoorian, C. H. Cho, N. Waldöfner, R. Scholz, A. Jordan, S. A. Loening and P. Wust, *Eur. Urol.*, 2007, **52**, 1653-1662.
30. M. Johannsen, B. Thiesen, U. Gneveckow, K. Taymoorian, N. Waldöfner, R. Scholz, S. Deger, K. Jung, S. A. Loening and A. Jordan, *Prostate.*, 2006, **66**, 97-104.
31. A. Jordan, R. Scholz, K. Maier-Hauff, M. Johannsen, P. Wust, J. Nadobny, H. Schirra, H. Schmidt, S. Deger and S. Loening, *J. Magn. Magn. Mater.*, 2001, **225**, 118-126.
32. Y. Kida, H. Ishiguri, K. Ichimi and T. Kobayashi, *No Shinkei Geka*, 1990, **18**, 521-526.
33. K. Maier-Hauff, F. Ulrich, D. Nestler, H. Niehoff, P. Wust, B. Thiesen, H. Orawa, V. Budach and A. Jordan, *J. Neurooncol.*, 2011, **103**, 317-324.

34. B. Stea, D. Shimm, J. Kittelson and T. Cetas, in *Interstitial Hyperthermia*, Springer, 1992, pp. 183-193.
35. R. D. Tucker, *J. Endourol.*, 2003, **17**, 601-607.
36. R. D. Tucker, C. Huidobro and T. Larson, *J. Endourol.*, 2005, **19**, 865-867.
37. R. D. Tucker, C. E. Platz, C. Huidobro and T. Larson, *Urology*, 2002, **60**, 166-169.
38. J. Kudr, Y. Haddad, L. Richtera, Z. Heger, M. Cernak, V. Adam and O. Zitka, *Nanomaterials*, 2017, **7**, 243.
39. C. S. Kumar, *Mater. Today*, 2010, **12**, 24-30.
40. A. C. Anselmo and S. Mitragotri, *Bioeng. Tran. Med.*, 2016, **1**, 10-29.
41. S. Dutz and R. Hergt, *Int. J. Hyperthermia*, 2013, **29**, 790-800.
42. B. D. Cullity and C. D. Graham, *Introduction to magnetic materials*, John Wiley & Sons, 2011.
43. S. Ruta, R. Chantrell and O. Hovorka, *Sci. Rep.*, 2015, **5**, 1-7.
44. R. E. Rosensweig, *J. Magn. Magn. Mater.*, 2002, **252**, 370-374.
45. M. Shliomis and V. Stepanov, *Adv. Chem. Phys.*, 1994, **87**, 1-30.
46. S. Laurent, S. Dutz, U. O. Häfeli and M. Mahmoudi, *Adv. Colloid Interface Sci.*, 2011, **166**, 8-23.
47. Q. A. Pankhurst, J. Connolly, S. K. Jones and J. Dobson, *J. Phys. D: Appl. Phys.*, 2003, **36**, R167.
48. L.-M. Lacroix, R. B. Malaki, J. Carrey, S. Lachaize, M. Respaud, G. Goya and B. Chaudret, *J. Appl. Phys.*, 2009, **105**, 023911.
49. E. C. Stoner and E. Wohlfarth, *IEEE Trans. Magn.*, 1991, **27**, 3475-3518.
50. R. Hergt, S. Dutz, R. Müller and M. Zeisberger, *J. Phys.: Condens. Matter*, 2006, **18**, S2919.
51. R. Chantrell, N. Walmsley, J. Gore and M. Maylin, *Phys. Rev. B*, 2000, **63**, 024410.
52. G. Salas, J. Camarero, D. Cabrera, H. l. n. Takacs, M. Varela, R. Ludwig, H. Dähring, I. Hilger, R. Miranda and M. a. d. P. Morales, *J. Phys. Chem. C.*, 2014, **118**, 19985-19994.
53. E. Garaio, J. M. Collantes, J. A. Garcia, F. Plazaola, S. Mornet, F. Couillaud and O. Sandre, *J. Magn. Magn. Mater.*, 2014, **368**, 432-437.
54. M. Kallumadil, M. Tada, T. Nakagawa, M. Abe, P. Southern and Q. A. Pankhurst, *J. Magn. Magn. Mater.*, 2009, **321**, 1509-1513.
55. W. J. Atkinson, I. A. Brezovich and D. P. Chakraborty, *IEEE Trans. Biomed. Eng.*, 1984, 70-75.
56. B. Thiesen and A. Jordan, *Int. J. Hyperthermia*, 2008, **24**, 467-474.
57. C. Blanco-Andujar, A. Walter, G. Cotin, C. Bordeianu, D. Mertz, D. Felder-Flesch and S. Begin-Colin, *Nanomedicine*, 2016, **11**, 1889-1910.
58. D. Faivre, *Iron oxides: from nature to applications*, John Wiley & Sons, 2016.
59. R. Hergt, S. Dutz and M. Röder, *J. Phys.: Condens. Matter*, 2008, **20**, 385214.
60. A. Doaga, A. Cojocariu, W. Amin, F. Heib, P. Bender, R. Hempelmann and O. Caltun, *Mater. Chem. Phys.*, 2013, **143**, 305-310.
61. S. Sabale, V. Jadhav, V. Khot, X. Zhu, M. Xin and H. Chen, *J. Mater. Sci. Mater. Med.*, 2015, **26**, 127.
62. Ç. E. Demirci, P. Manna, Y. Wroczynskyj, S. Aktürk and J. van Lierop, *J. Phys. D: Appl. Phys.*, 2017, **51**, 025003.
63. J.-H. Lee, J.-t. Jang, J.-s. Choi, S. H. Moon, S.-h. Noh, J.-w. Kim, J.-G. Kim, I.-S. Kim, K. I. Park and J. Cheon, *Nat. Nanotechnol.*, 2011, **6**, 418.
64. A. Roca, M. Morales, K. O'Grady and C. Serna, *Nanotechnology*, 2006, **17**, 2783.
65. P. Guardia, A. Labarta and X. Batlle, *J. Phys. Chem. C.*, 2010, **115**, 390-396.
66. D. Caruntu, G. Caruntu and C. J. O'Connor, *J. Phys. D: Appl. Phys.*, 2007, **40**, 5801.
67. V. Mameli, A. Musinu, A. Ardu, G. Ennas, D. Peddis, D. Niznansky, C. Sangregorio, C. Innocenti, N. T. Thanh and C. Cannas, *Nanoscale*, 2016, **8**, 10124-10137.
68. Q. Song and Z. J. Zhang, *J. Phys. Chem. B.*, 2006, **110**, 11205-11209.
69. S. Ammar, N. Jouini, F. Fiévet, Z. Beji, L. Smiri, P. Moliné, M. Danot and J.-M. Grenèche, *J. Phys.: Condens. Matter*, 2006, **18**, 9055.

70. A. Bordet, L. M. Lacroix, P. F. Fazzini, J. Carrey, K. Soulantica and B. Chaudret, *Angew. Chem. Int. Ed.*, 2016, **55**, 15894-15898.
71. A. Meffre, B. Mehdaoui, V. Kelsen, P. F. Fazzini, J. Carrey, S. Lachaize, M. Respaud and B. Chaudret, *Nano Lett.*, 2012, **12**, 4722-4728.
72. P. Guardia, A. Riedinger, S. Nitti, G. Pugliese, S. Marras, A. Genovese, M. E. Materia, C. Lefevre, L. Manna and T. Pellegrino, *J. Mater. Chem. B*, 2014, **2**, 4426-4434.
73. P. Guardia, R. Di Corato, L. Lartigue, C. Wilhelm, A. Espinosa, M. Garcia-Hernandez, F. Gazeau, L. Manna and T. Pellegrino, *ACS nano*, 2012, **6**, 3080-3091.
74. R. Di Corato, A. Espinosa, L. Lartigue, M. Tharaud, S. Chat, T. Pellegrino, C. Ménager, F. Gazeau and C. Wilhelm, *Biomaterials*, 2014, **35**, 6400-6411.
75. A. Sathya, P. Guardia, R. Brescia, N. Silvestri, G. Pugliese, S. Nitti, L. Manna and T. Pellegrino, *Chem. Mater.*, 2016, **28**, 1769-1780.
76. J. t. Jang, H. Nah, J. H. Lee, S. H. Moon, M. G. Kim and J. Cheon, *Angew. Chem.*, 2009, **121**, 1260-1264.
77. B. Mehdaoui, A. Meffre, L.-M. Lacroix, J. Carrey, S. Lachaize, M. Gougeon, M. Respaud and B. Chaudret, *J. Magn. Magn. Mater.*, 2010, **322**, L49-L52.
78. A. Shavel, B. Rodríguez-González, M. Spasova, M. Farle and L. M. Liz-Marzán, *Adv. Funct. Mater.*, 2007, **17**, 3870-3876.
79. R. Das, J. Alonso, Z. Nemati Porshokouh, V. Kalappattil, D. Torres, M.-H. Phan, E. Garaio, J. A. n. García, J. L. Sanchez Llamazares and H. Srikanth, *J. Phys. Chem. C.*, 2016, **120**, 10086-10093.
80. H. Sun, B. Chen, X. Jiao, Z. Jiang, Z. Qin and D. Chen, *J. Phys. Chem. C.*, 2012, **116**, 5476-5481.
81. L. Lartigue, P. Hugounenq, D. Alloyeau, S. P. Clarke, M. Levy, J.-C. Bacri, R. Bazzi, D. F. Brougham, C. Wilhelm and F. Gazeau, *ACS nano*, 2012, **6**, 10935-10949.
82. Y. Lv, Y. Yang, J. Fang, H. Zhang, E. Peng, X. Liu, W. Xiao and J. Ding, *RSC Advances*, 2015, **5**, 76764-76771.
83. S.-h. Noh, W. Na, J.-t. Jang, J.-H. Lee, E. J. Lee, S. H. Moon, Y. Lim, J.-S. Shin and J. Cheon, *Nano Lett.*, 2012, **12**, 3716-3721.
84. A. l. Walter, C. Billotey, A. Garofalo, C. Ulhaq-Bouillet, C. Lefèvre, J. Taleb, S. Laurent, L. Vander Elst, R. N. Muller and L. n. Lartigue, *Chem. Mater.*, 2014, **26**, 5252-5264.
85. A. Lak, M. Cassani, B. T. Mai, N. Winckelmans, D. Cabrera, E. Sadrollahi, S. Marras, H. Remmer, S. Fiorito and L. Cremades-Jimeno, *Nano Lett.*, 2018, **18**, 6856-6866.
86. P. Guardia, S. Nitti, M. Materia, G. Pugliese, N. Yaacoub, J.-M. Greneche, C. Lefevre, L. Manna and T. Pellegrino, *J. Mater. Chem. B*, 2017, **5**, 4587-4594.
87. E. Fantechi, A. G. Roca, B. Sepúlveda, P. Torruella, S. Estradé, F. Peiró, E. Coy, S. Jurga, N. G. Bastús and J. Nogués, *Chem. Mater.*, 2017, **29**, 4022-4035.
88. R. Das, N. Rinaldi-Montes, J. Alonso, Z. Amghouz, E. Garaio, J. García, P. Gorria, J. Blanco, M. Phan and H. Srikanth, *ACS Appl. Mater. Interfaces*, 2016, **8**, 25162-25169.
89. D. Niculaes, A. Lak, G. C. Anyfantis, S. Marras, O. Laslett, S. K. Avugadda, M. Cassani, D. Serantes, O. Hovorka and R. Chantrell, *ACS nano*, 2017, **11**, 12121-12133.
90. K. H. Bae, M. Park, M. J. Do, N. Lee, J. H. Ryu, G. W. Kim, C. Kim, T. G. Park and T. Hyeon, *ACS nano*, 2012, **6**, 5266-5273.
91. J.-P. Fortin, C. Wilhelm, J. Servais, C. Ménager, J.-C. Bacri and F. Gazeau, *J. Am. Chem. Soc.*, 2007, **129**, 2628-2635.
92. M. Lévy, C. Wilhelm, J.-M. Siaugue, O. Horner, J.-C. Bacri and F. Gazeau, *J. Phys.: Condens. Matter*, 2008, **20**, 204133.
93. S. Purushotham and R. Ramanujan, *J. Appl. Phys.*, 2010, **107**, 114701.
94. G. Salas, C. Casado, F. J. Teran, R. Miranda, C. J. Serna and M. P. Morales, *J. Mater. Chem.*, 2012, **22**, 21065-21075.

95. S. Kubickova, D. Niznansky, M. Morales Herrero, G. Salas and J. Vejpravova, *Appl. Phys. Lett.*, 2014, **104**, 223105.
96. R. S. Sapieszko and E. Matijević, *J. Colloid Interface Sci.*, 1980, **74**, 405-422.
97. F. A. Tourinho, R. Franck and R. Massart, *J. Mater. Sci.*, 1990, **25**, 3249-3254.
98. K. Tao, H. Dou and K. Sun, *Colloids Surf. Physicochem. Eng. Aspects*, 2008, **320**, 115-122.
99. A. Faiyas, E. Vinod, J. Joseph, R. Ganesan and R. Pandey, *J. Magn. Magn. Mater.*, 2010, **322**, 400-404.
100. S. Park, C.-H. Kim, W.-J. Lee, S. Sung and M.-H. Yoon, *Mater. Sci. Eng.*, 2017, **114**, 1-22.
101. A. P. LaGrow, M. O. Besenhard, A. Hodzic, A. Sergides, L. K. Bogart, A. Gavriilidis and N. T. K. Thanh, *Nanoscale*, 2019, **11**, 6620-6628.
102. Z. Li, B. Tan, M. Allix, A. I. Cooper and M. J. Rosseinsky, *small*, 2008, **4**, 231-239.
103. M. Mascolo, Y. Pei and T. Ring, *Materials*, 2013, **6**, 5549-5567.
104. N. Gehrke, A. Briel, F. Ludwig, H. Remmer, T. Wawrzik and S. Wellert, in *Magnetic Particle Imaging*, Springer, 2012, pp. 99-103.
105. N. Gehrke, D. Heinke, D. Eberbeck and A. Briel, 2013.
106. T. Sugimoto and E. Matijević, *J. Colloid Interface Sci.*, 1980, **74**, 227-243.
107. H. Gavilán, M. Brollo, L. Gutiérrez, S. Veintemillas-Verdaguer and M. Morales, *Clinical Applications of Magnetic Nanoparticles: From Fabrication to Clinical Applications*, 2018, 1.
108. M. A. Vergés, R. Costo, A. Roca, J. Marco, G. Goya, C. Serna and M. Morales, *J. Phys. D: Appl. Phys.*, 2008, **41**, 134003.
109. M. Marciello, V. Connord, S. Veintemillas-Verdaguer, M. A. Vergés, J. Carrey, M. Respaud, C. J. Serna and M. P. Morales, *J. Mater. Chem. B*, 2013, **1**, 5995-6004.
110. D. Forge, Y. Gossuin, A. Roch, S. Laurent, L. V. Elst and R. N. Muller, *Contrast Media Mol. Imaging*, 2010, **5**, 126-132.
111. S. Lefebure, E. Dubois, V. Cabuil, S. Neveu and R. Massart, *J. Mater. Res.*, 1998, **13**, 2975-2981.
112. T. Yoshida, T. Nakamura, O. Higashi and K. Enpuku, *Jpn. J. Appl. Phys.*, 2018, **57**, 080302.
113. S. K. R. Williams, J. R. Runyon and A. A. Ashames, *Journal*, 2010, 634-642.
114. N. Löwa, P. Knappe, F. Wiekhorst, D. Eberbeck, A. F. Thünemann and L. Trahms, *J. Magn. Magn. Mater.*, 2015, **380**, 266-270.
115. N. Löwa, D. Eberbeck, U. Steinhoff, F. Wiekhorst and L. Trahms, in *Magnetic Particle Imaging*, Springer, 2012, pp. 73-78.
116. A. Styskalik, D. Skoda, C. E. Barnes and J. Pinkas, *Catalysts*, 2017, **7**, 168.
117. A. G. Roca, L. Gutiérrez, H. Gavilán, M. E. F. Brollo, S. Veintemillas-Verdaguer and M. del Puerto Morales, *Adv. Drug Del. Rev.*, 2018.
118. M. Niederberger and G. Garnweitner, *Chem. Eur. J.*, 2006, **12**, 7282-7302.
119. S. J. Kemp, R. M. Ferguson, A. P. Khandhar and K. M. Krishnan, *RSC Advances*, 2016, **6**, 77452-77464.
120. J. Shan, L. Wang, H. Yu, J. Ji, W. Amer, Y. Chen, G. Jing, H. Khalid, M. Akram and N. Abbasi, *Mater. Sci. Technol.*, 2016, **32**, 602-614.
121. S. Belaïd, D. Stanicki, L. Vander Elst, R. N. Muller and S. Laurent, *Nanotechnology*, 2018, **29**, 165603.
122. W. Y. William, J. C. Falkner, C. T. Yavuz and V. L. Colvin, *Chem. Commun.*, 2004, 2306-2307.
123. A. Shavel and L. M. Liz-Marzán, *Phys. Chem. Chem. Phys.*, 2009, **11**, 3762-3766.
124. R. Hufschmid, H. Arami, R. M. Ferguson, M. Gonzales, E. Teeman, L. N. Brush, N. D. Browning and K. M. Krishnan, *Nanoscale*, 2015, **7**, 11142-11154.
125. S. G. Kwon, Y. Piao, J. Park, S. Angappane, Y. Jo, N.-M. Hwang, J.-G. Park and T. Hyeon, *J. Am. Chem. Soc.*, 2007, **129**, 12571-12584.

126. M. Gonzales-Weimuller, M. Zeisberger and K. M. Krishnan, *J. Magn. Magn. Mater.*, 2009, **321**, 1947-1950.
127. C.-J. Chen, R.-K. Chiang, H.-Y. Lai and C.-R. Lin, *J. Phys. Chem. C.*, 2010, **114**, 4258-4263.
128. A. Lassenberger, T. Grünewald, P. Van Oostrum, H. Rennhofer, H. Amenitsch, R. Zirbs, H. Lichtenegger and E. Reimhult, *Chem. Mater.*, 2017, **29**, 4511-4522.
129. L. M. Bronstein, X. Huang, J. Retrum, A. Schmucker, M. Pink, B. D. Stein and B. Dragnea, *Chem. Mater.*, 2007, **19**, 3624-3632.
130. J. Park, K. An, Y. Hwang, J.-G. Park, H.-J. Noh, J.-Y. Kim, J.-H. Park, N.-M. Hwang and T. Hyeon, *Nat. Mater.*, 2004, **3**, 891.
131. A. H. Yusoff, M. N. Salimi and M. F. Jamlos, *Adv. Nano Res.*, 2018, **6**, 1.
132. I. Sato, M. Umemura, K. Mitsudo, M. Kioi, H. Nakashima, T. Iwai, X. Feng, K. Oda, A. Miyajima and A. Makino, *J Physiol. Sci.*, 2014, **64**, 177-183.
133. K. Murase, M. Aoki, N. Banura, K. Nishimoto, A. Mimura, T. Kuboyabu and I. Yabata, *Open j. Med. Imag.*, 2015, **5**, 85.
134. Y. V. Kolen'ko, M. Bañobre-López, C. Rodríguez-Abreu, E. Carbó-Argibay, A. Sailsman, Y. Piñeiro-Redondo, M. F. Cerqueira, D. Y. Petrovykh, K. Kovnir and O. I. Lebedev, *J. Phys. Chem. C.*, 2014, **118**, 8691-8701.
135. M. Avolio, H. Gavilán, E. Mazario, F. Brero, P. Arosio, A. Lascialfari and M. P. Morales, *Phys. Chem. Chem. Phys.*, 2019, **21**, 18741-18752.
136. P. Hugounenq, M. Levy, D. Alloyeau, L. Lartigue, E. Dubois, V. r. Cabuil, C. Ricolleau, S. p. Roux, C. Wilhelm and F. Gazeau, *J. Phys. Chem. C.*, 2012, **116**, 15702-15712.
137. Z. Nemati, J. Alonso, L. Martinez, H. Khurshid, E. Garaio, J. Garcia, M. Phan and H. Srikanth, *J. Phys. Chem. C.*, 2016, **120**, 8370-8379.
138. D. Kim, N. Lee, M. Park, B. H. Kim, K. An and T. Hyeon, *J. Am. Chem. Soc.*, 2008, **131**, 454-455.
139. H. Ai, C. Flask, B. Weinberg, X. Shuai, M. D. Pagel, D. Farrell, J. Duerk and J. Gao, *Adv. Mater.*, 2005, **17**, 1949-1952.
140. R. Chen, M. G. Christiansen, A. Sourakov, A. Mohr, Y. Matsumoto, S. Okada, A. Jasanoff and P. Anikeeva, *Nano Lett.*, 2016, **16**, 1345-1351.
141. K. Lee, S. Lee, M. Oh and B. Ahn, *Metals*, 2018, **8**, 107.
142. E. C. Abenojar, S. Wickramasinghe, J. Bas-Concepcion and A. C. S. Samia, *Prog. Nat. Sci.*, 2016, **26**, 440-448.
143. A. Feld, A. Weimer, A. Kornowski, N. Winckelmans, J.-P. Merkl, H. Kloust, R. Zierold, C. Schmidtke, T. Schotten and M. Riedner, *ACS nano*, 2018, **13**, 152-162.
144. S. Sun, H. Zeng, D. B. Robinson, S. Raoux, P. M. Rice, S. X. Wang and G. Li, *J. Am. Chem. Soc.*, 2004, **126**, 273-279.
145. A. Shavel, B. Rodríguez-González, J. Pacifico, M. Spasova, M. Farle and L. M. Liz-Marzán, *Chem. Mater.*, 2009, **21**, 1326-1332.
146. D. Caruntu, G. Caruntu, Y. Chen, C. J. O'Connor, G. Goloverda and V. L. Kolesnichenko, *Chem. Mater.*, 2004, **16**, 5527-5534.
147. H. Gavilán, O. Posth, L. K. Bogart, U. Steinhoff, L. Gutiérrez and M. P. Morales, *Acta Mater.*, 2017, **125**, 416-424.
148. G. Salazar-Alvarez, J. Qin, V. Sepelak, I. Bergmann, M. Vasilakaki, K. Trohidou, J. Ardisson, W. Macedo, M. Mikhaylova and M. Muhammed, *J. Am. Chem. Soc.*, 2008, **130**, 13234-13239.
149. N. Lee, Y. Choi, Y. Lee, M. Park, W. K. Moon, S. H. Choi and T. Hyeon, *Nano Lett.*, 2012, **12**, 3127-3131.
150. A. Espinosa, R. Di Corato, J. Kolosnjaj-Tabi, P. Flaud, T. Pellegrino and C. Wilhelm, *ACS nano*, 2016, **10**, 2436-2446.

151. J. Kolosnjaj-Tabi, R. Di Corato, L. Lartigue, I. Marangon, P. Guardia, A. K. Silva, N. Luciani, O. Clement, P. Flaud and J. V. Singh, *ACS nano*, 2014, **8**, 4268-4283.
152. A. Bordet, R. F. Landis, Y. Lee, G. Y. Tonga, J. M. Asensio, C.-H. Li, P.-F. Fazzini, K. Soulantica, V. M. Rotello and B. Chaudret, *ACS nano*, 2019, **13**, 2870-2878.
153. M. S. Darwish, H. Kim, H. Lee, C. Ryu, J. Y. Lee and J. Yoon, *Nanomaterials*, 2019, **9**, 1176.
154. Y. Luengo, M. A. Roldan, M. Varela, F. Herranz, M. P. Morales and S. Veintemillas-Verdaguer, *J. Phys. Chem. C.*, 2019, **123**, 7356-7365.
155. A. F. Rebolledo, O. Bomatí-Miguel, J. F. Marco and P. Tartaj, *Adv. Mater.*, 2008, **20**, 1760-1765.
156. S. Gul, S. B. Khan, I. U. Rehman, M. A. Khan and M. Khan, *Front. Mater.*, 2019, **6**, 179.
157. Z. Hedayatnasab, F. Abnisa and W. M. A. W. Daud, *Materials & Design*, 2017, **123**, 174-196.
158. S. Majidi, F. Zeinali Sehrig, S. M. Farkhani, M. Soleymani Goloujeh and A. Akbarzadeh, *Artif Cells Nanomed. Biotechnol.*, 2016, **44**, 722-734.
159. D. Bandyopadhyay, G. Singh and A. V. Kulkarni, *Sci. Rep.*, 2019, **9**, 1-9.
160. S. Araújo-Barbosa and M. Morales, *J. Alloys Compd.*, 2019, **787**, 935-943.
161. A. Salati, A. Ramazani and M. A. Kashi, *J. Magn. Magn. Mater.*, 2020, **498**, 166172.
162. S. Del Sol-Fernández, Y. Portilla-Tundidor, L. Gutiérrez, O. F. Odio, E. Reguera, D. F. Barber and M. Morales, *ACS Appl. Mater. Interfaces*, 2019, **11**, 26648-26663.
163. Q. Feng, Y. Liu, J. Huang, K. Chen, J. Huang and K. Xiao, *Sci. Rep.*, 2018, **8**, 2082.
164. M. F. Casula, E. Conca, I. Bakaimi, A. Sathya, M. E. Materia, A. Casu, A. Falqui, E. Sogne, T. Pellegrino and A. G. Kanaras, *Phys. Chem. Chem. Phys.*, 2016, **18**, 16848-16855.
165. D. Yoo, H. Jeong, S. H. Noh, J. H. Lee and J. Cheon, *Angew. Chem. Int. Ed.*, 2013, **52**, 13047-13051.
166. L. Zhang, Z. Liu, Y. Liu, Y. Wang, P. Tang, Y. Wu, H. Huang, Z. Gan, J. Liu and D. Wu, *Biomaterials*, 2020, **230**, 119655.
167. P. B. Balakrishnan, N. Silvestri, T. Fernandez-Cabada, F. Marinaro, S. Fernandes, S. Fiorito, M. Miscuglio, D. Serantes, S. Ruta and K. Livesey, *Adv. Mater.*, 2020, **32**, 2003712.
168. J. Xie, C. Yan, Y. Yan, L. Chen, L. Song, F. Zang, Y. An, G. Teng, N. Gu and Y. Zhang, *Nanoscale*, 2016, **8**, 16902-16915.
169. R. Gupta and D. Sharma, *ACS Appl. Nano Mater.*, 2020, **3**, 2026-2037.
170. A. Espinosa, M. Bugnet, G. Radtke, S. Neveu, G. A. Botton, C. Wilhelm and A. Abou-Hassan, *Nanoscale*, 2015, **7**, 18872-18877.
171. A. Lopez-Ortega, M. Estrader, G. Salazar-Alvarez, A. G. Roca and J. Nogues, *Phys. Rep.*, 2015, **553**, 1-32.
172. H. Yu, M. Chen, P. M. Rice, S. X. Wang, R. White and S. Sun, *Nano Lett.*, 2005, **5**, 379-382.
173. C. Wang, H. Yin, S. Dai and S. Sun, *Chem. Mater.*, 2010, **22**, 3277-3282.
174. H. Kakwere, M. E. Materia, A. Curcio, M. Prato, A. Sathya, S. Nitti and T. Pellegrino, *Nanoscale*, 2018, **10**, 3930-3944.
175. F. Mazuel, A. Espinosa, N. Luciani, M. Reffay, R. Le Borgne, L. Motte, K. Desboeufs, A. Michel, T. Pellegrino and Y. Lalatonne, *ACS nano*, 2016, **10**, 7627-7638.
176. E. A. Hussein, M. M. Zagho, G. K. Nasrallah and A. A. Elzatahry, *Int. J. Nanomed.*, 2018, **13**, 2897.
177. A. Curcio, A. K. Silva, S. Cabana, A. Espinosa, B. Baptiste, N. Menguy, C. Wilhelm and A. Abou-Hassan, *Theranostics*, 2019, **9**, 1288.
178. A. Karpavičius, A. Coene, P. Bender and J. Leliaert, *Nanoscale Advances*, 2021, **3**, 1633-1645.
179. P. Bender, D. Honecker and L. Fernández Barquín, *Appl. Phys. Lett.*, 2019, **115**, 132406.
180. C. Martinez-Boubeta, K. Simeonidis, A. Makridis, M. Angelakeris, O. Iglesias, P. Guardia, A. Cabot, L. Yedra, S. Estradé, F. Peiró, Z. Saghi, P. A. Midgley, I. Conde-Leborán, D. Serantes and D. Baldomir, *Sci. Rep.*, 2013, **3**, 1652.
181. J. G. Ovejero, D. Cabrera, J. Carrey, T. Valdivielso, G. Salas and F. J. Teran, *Phys. Chem. Chem. Phys.*, 2016, **18**, 10954-10963.

182. P. H. Linh, N. V. Chien, D. D. Dung, P. H. Nam, D. T. Hoa, N. T. N. Anh, L. V. Hong, N. X. Phuc and P. T. Phong, *J. Mater. Sci.*, 2018, **53**, 8887–8900.
183. C. Martinez-Boubeta, K. Simeonidis, D. Serantes, I. Conde-Leborán, I. Kazakis, G. Stefanou, L. Peña, R. Galceran, L. Balcells, C. Monty, D. Baldomir, M. Mitrakas and M. Angelakeris, *Adv. Funct. Mater.*, 2012, **22**, 3737-3744.
184. C. Guibert, V. Dupuis, V. Peyre and J. Fresnais, *J. Phys. Chem. C.*, 2015, **119**, 28148-28154.
185. R. Fu, Y. Yan, C. Roberts, Z. Liu and Y. Chen, *Sci. Rep.*, 2018, **8**, 1-10.
186. D. Serantes, K. Simeonidis, M. Angelakeris, O. Chubykalo-Fesenko, M. Marciello, M. Del Puerto Morales, D. Baldomir and C. Martinez-Boubeta, *J. Phys. Chem. C.*, 2014, **118**, 5927-5934.
187. M. E. Materia, P. Guardia, A. Sathya, M. Pernia Leal, R. Marotta, R. Di Corato and T. Pellegrino, *Langmuir*, 2015, **31**, 808-816.
188. S. Dutz, J. H. Clement, D. Eberbeck, T. Gelbrich, R. Hergt, R. Müller, J. Wotschadlo and M. Zeisberger, *J. Magn. Magn. Mater.*, 2009, **321**, 1501-1504.
189. S. K. Avugadda, M. E. Materia, R. Nigmatullin, D. Cabrera, R. Marotta, T. F. Cabada, E. Marcello, S. Nitti, E. J. Artés-Ibañez, P. Basnett, C. Wilhelm, F. J. Teran, I. Roy and T. Pellegrino, *Chem. Mater.*, 2019, **31**, 5450-5463.
190. A. Weddemann, A. Auge, D. Kappe, F. Wittbracht and A. Hütten, *J. Magn. Magn. Mater.*, 2010, **322**, 643-646.
191. K. Nakata, Y. Hu, O. Uzun, O. Bakr and F. Stellacci, *Adv. Mater.*, 2008, **20**, 4294-4299.
192. L. Gutiérrez, L. De La Cueva, M. Moros, E. Mazarío, S. De Bernardo, J. M. De La Fuente, M. P. Morales and G. Salas, *Nanotechnology*, 2019, **30**, 112001.
193. R. Mejías, P. Hernández Flores, M. Talelli, J. L. Tajada-Herráiz, M. E. F. Brollo, Y. Portilla, M. P. Morales and D. F. Barber, *ACS Appl. Mater. Interfaces*, 2019, **11**, 340-355.
194. D. Cabrera, A. Coene, J. Leliaert, E. J. Artés-Ibáñez, L. Dupré, N. D. Telling and F. J. Teran, *ACS Nano*, 2018, **12**, 2741-2752.
195. D. Soukup, S. Moise, E. Céspedes, J. Dobson and N. D. Telling, *Acs Nano*, 2015, **9**, 231-240.
196. J.-P. Fortin, F. Gazeau and C. Wilhelm, *Eur. Biophys. J.*, 2008, **37**, 223-228.
197. E. Alphandéry, S. Faure, L. Raison, E. Duguet, P. A. Howse and D. A. Bazylinski, *J. Phys. Chem. C.*, 2011, **115**, 18-22.
198. H. A. Albarqi, L. H. Wong, C. Schumann, F. Y. Sabei, T. Korzun, X. Li, M. N. Hansen, P. Dhagat, A. S. Moses and O. Taratula, *ACS nano*, 2019, **13**, 6383-6395.
199. S. K. Avugadda, M. E. Materia, R. Nigmatullin, D. Cabrera, R. Marotta, T. F. Cabada, E. Marcello, S. Nitti, E. J. Artés-Ibañez and P. Basnett, *Chem. Mater.*, 2019, **31**, 5450-5463.
200. I. Andreu, E. Natividad, L. Solozábal and O. Roubeau, *ACS Nano*, 2015, **9**, 1408-1419.
201. S. L. Saville, B. Qi, J. Baker, R. Stone, R. E. Camley, K. L. Livesey, L. Ye, T. M. Crawford and O. Thompson Mefford, *J. Colloid Interface Sci.*, 2014, **424**, 141-151.
202. S. Ranoo, B. Lahiri, T. Muthukumaran and J. Philip, *Appl. Phys. Lett.*, 2019, **115**, 043102.
203. N. Usov, R. Rytov and V. Bautin, *Sci. Rep.*, 2021, **11**, 1-11.
204. B. Mehdaoui, R. P. Tan, A. Meffre, J. Carrey, S. Lachaize, B. Chaudret and M. Respaud, *Phys. Rev. B*, 2013, **87**, 174419.
205. E. Alphandéry, S. Faure, O. Seksek, F. Guyot and I. Chebbi, *ACS nano*, 2011, **5**, 6279-6296.
206. E. Alphandéry, S. Faure, L. Raison, E. Duguet, P. A. Howse and D. A. Bazylinski, *J. Phys. Chem. C.*, 2011, **115**, 18-22.
207. I. Andreu, E. Natividad, L. Solozábal and O. Roubeau, *ACS Nano*, 2015, **9**, 1408-1419.
208. J. M. Asensio, J. Marbaix, N. Mille, L.-M. Lacroix, K. Soulantica, P.-F. Fazzini, J. Carrey and B. Chaudret, *Nanoscale*, 2019, **11**, 5402-5411.
209. B. Sanz, R. Cabreira-Gomes, T. E. Torres, D. P. Valdés, E. Lima Jr, E. De Biasi, R. D. Zysler, M. R. Ibarra and G. F. Goya, *ACS Appl. Nano Mater.*, 2020, **3**, 8719-8731.

210. E. Alphandéry, I. Chebbi, F. Guyot and M. Durand-Dubief, *Int. J. Hyperthermia*, 2013, **29**, 801-809.
211. W. Wu, Z. Wu, T. Yu, C. Jiang and W. S. Kim, *Sci. Technol. Adv. Mater.*, 2015, **16**, 023501.
212. N. C. Bigall, C. Wilhelm, M.-L. Beoutis, M. García-Hernandez, A. A. Khan, C. Giannini, A. Sánchez-Ferrer, R. Mezzenga, M. E. Materia and M. A. Garcia, *Chem. Mater.*, 2013, **25**, 1055-1062.
213. J. M. Anderson and M. S. Shive, *Adv. Drug Del. Rev.*, 2012, **64**, 72-82.
214. J. F. Berret, N. Schonbeck, F. Gazeau, D. El Kharrat, O. Sandre, A. Vacher and M. Airiau, *J. Am. Chem. Soc.*, 2006, **128**, 1755-1761.
215. F. Xiong, Y. Chen, J. Chen, B. Yang, Y. Zhang, H. Gao, Z. Hua and N. Gu, *J. Control. Release*, 2013, **172**, 993-100.
216. R. Di Corato, N. C. Bigall, A. Ragusa, D. Dorfs, A. Genovese, R. Marotta, L. Manna and T. Pellegrino, *Acs Nano*, 2011, **5**, 1109-1121.
217. P. Basnett, E. Marcello, B. Lukasiewicz, B. Panchal, R. Nigmatullin, J. C. Knowles and I. Roy, *J. Mater. Sci. Mater. Med.*, 2018, **29**, 179.
218. D. Cabrera, A. Lak, T. Yoshida, M. Materia, D. Ortega, F. Ludwig, P. Guardia, A. Sathya, T. Pellegrino and F. Teran, *Nanoscale*, 2017, **9**, 5094-5101.
219. P. Phong, L. Nguyen, L. Phong, P. Nam, D. Manh, I. J. Lee and N. Phuc, *J. Magn. Magn. Mater.*, 2017, **428**, 36-42.
220. B. Sanz, M. P. Calatayud, E. De Biasi, E. Lima Jr, M. V. Mansilla, R. D. Zysler, M. R. Ibarra and G. F. Goya, *Sci. Rep.*, 2016, **6**, 38733.
221. M. K. Kuimova, S. W. Botchway, A. W. Parker, M. Balaz, H. A. Collins, H. L. Anderson, K. Suhling and P. R. Ogilby, *Nat. Chem.*, 2009, **1**, 69.
222. M. K. Kuimova, G. Yahioglu, J. A. Levitt and K. Suhling, *J. Am. Chem. Soc.*, 2008, **130**, 6672-6673.
223. Y. Piñeiro-Redondo, M. Bañobre-López, I. Pardiñas-Blanco, G. Goya, M. A. López-Quintela and J. Rivas, *Nanoscale Res. Lett.*, 2011, **6**, 383.
224. N. A. Usov, R. A. Rytov and V. A. Bautin, *Beilstein Archives*, 2019, **2019**, 57.
225. G. Vallejo-Fernandez, O. Whear, A. Roca, S. Hussain, J. Timmis, V. Patel and K. O'Grady, *J. Phys. D: Appl. Phys.*, 2013, **46**, 312001.
226. E. Céspedes, J. M. Byrne, N. Farrow, S. Moise, V. S. Coker, M. Bencsik, J. R. Lloyd and N. D. Telling, *Nanoscale*, 2014, **6**, 12958-12970.
227. D. Serantes, R. Chantrell, H. Gavilán, M. del Puerto Morales, O. Chubykalo-Fesenko, D. Baldomir and A. Satoh, *Phys. Chem. Chem. Phys.*, 2018, **20**, 30445-30454.
228. S. Kokura, T. Yoshikawa and T. Ohnishi, *Hyperthermic oncology from bench to bedside*, Springer, 2016.
229. N. Bohmer and A. Jordan, *Beilstein J. Nanotechnol.*, 2015, **6**, 167-176.
230. K. Maier-Hauff, R. Rothe, R. Scholz, U. Gneveckow, P. Wust, B. Thiesen, A. Feussner, A. von Deimling, N. Waldoefner and R. Felix, *J. Neurooncol.*, 2007, **81**, 53-60.
231. P. Wust, U. Gneveckow, P. Wust, U. Gneveckow, M. Johannsen, D. Böhmer, T. Henkel, F. Kahmann, J. Sehouli and R. Felix, *Int. J. Hyperthermia*, 2006, **22**, 673-685.
232. J. Van der Zee, *Ann. Oncol.*, 2002, **13**, 1173-1184.
233. S. Nardecchia, P. Sánchez-Moreno, J. de Vicente, J. A. Marchal and H. Boulaiz, *Nanomaterials*, 2019, **9**, 191.
234. D. Hanahan and R. A. Weinberg, *Cell*, 2000, **100**, 57-70.
235. D. Hanahan and R. A. Weinberg, *Cell*, 2011, **144**, 646-674.
236. R. S. Bindra, M. E. Crosby and P. M. Glazer, *Cancer Metastasis Rev.*, 2007, **26**, 249-260.
237. J. Overgaard, *Int. J. Radiat. Oncol. Biol. Phys.*, 1989, **16**, 535-549.
238. M. R. Horsman and J. Overgaard, *Clin. Oncol.*, 2007, **19**, 418-426.
239. J. Overgaard, *Radiother. Oncol.*, 2013, **109**, 185-187.
240. O. S. Nielsen, *Int. J. Radiat. Biol. Relat. Stud. Phys. Chem. Med.*, 1981, **39**, 73-82.

241. P. Vaupel and M. R. Horsman, *Int. J. Hyperthermia*, 2010, **26**, 209-210.
242. C. W. Song, *Cancer Res.*, 1984, **44**, 4721s-4730s.
243. N. F. Voelxen, S. Blatt, P. Knopf, M. Henkel, C. Appelhans, L. A. Righesso, A. Pabst, J. Goldschmitt, S. Walenta and A. Neff, *Clin. Oral Investig.*, 2018, **22**, 1033-1043.
244. I. F. Tannock and D. Rotin, *Cancer Res.*, 1989, **49**, 4373-4384.
245. K. Engin, D. B. Leeper, A. J. Thistlethwaite, L. Tupchong, D. Phil and J. D. McFarlane, *Int. J. Radiat. Oncol. Biol. Phys.*, 1994, **29**, 125-132.
246. T. M. Zagar, J. R. Oleson, Z. Vujaskovic, M. W. Dewhirst, O. I. Craciunescu, K. L. Blackwell, L. R. Prosnitz and E. L. Jones, *Int. J. Hyperthermia*, 2010, **26**, 612-617.
247. J. Van Der Zee, M. De Bruijne, J. Mens, A. Ameziane, M. Broekmeyer-Reurink, T. Drizdal, M. Linthorst and G. Van Rhoon, *Int. J. Hyperthermia*, 2010, **26**, 638-648.
248. N. R. Datta, E. Puric, D. Klingbiel, S. Gomez and S. Bodis, *Int. J. Radiat. Oncol. Biol. Phys.*, 2016, **94**, 1073-1087.
249. M. Franckena, *Int. J. Hyperthermia*, 2012, **28**, 543-548.
250. M. Franckena and J. van der Zee, *Curr. Opin. Obstet. Gynecol.*, 2010, **22**, 9-14.
251. A. Chicheł, J. Skowronek, M. Kubaszewska and M. Kanikowski, *Rep Pract Oncol Radiother.*, 2007, **12**, 267-275.
252. B. Emami, C. Scott, C. A. Perez, S. Asbell, P. Swift, P. Grigsby, A. Montesano, P. Rubin, W. Curran and J. Delrowe, *Int. J. Radiat. Oncol. Biol. Phys.*, 1996, **34**, 1097-1104.
253. H. Etemadi and P. G. Plieger, *Adv. Ther.*, 2020, **3**, 2000061.
254. E. L. Gillette and B. A. Ensley, *Int. J. Radiat. Oncol. Biol. Phys.*, 1979, **5**, 209-213.
255. J. Overgaard, *Int. J. Radiat. Oncol. Biol. Phys.*, 1980, **6**, 1507-1517.
256. O. S. Nielsen, *Dan. Med. Bull.*, 1984, **31**, 376-390.
257. G. C. Li and H. B. Kal, *Eur. J. Cancer*, 1977, **13**, 65-69.
258. S. A. Sapareto, G. P. Raaphorst and W. C. Dewey, *Int. J. Radiat. Oncol. Biol. Phys.*, 1979, **5**, 343-347.
259. D. Chang, M. Lim, J. A. Goos, R. Qiao, Y. Y. Ng, F. M. Mansfeld, M. Jackson, T. P. Davis and M. Kavallaris, *Front. Pharmacol.*, 2018, **9**, 831.
260. A. Ohki, T. Kuboyabu, M. Aoki, M. Yamawaki and K. Murase, *Int. J. Nanomedl. Nanosurg.*, 2016, **2**, 1-6.
261. A. Attaluri, S. K. Kandala, M. Wabler, H. Zhou, C. Cornejo, M. Armour, M. Hedayati, Y. Zhang, T. L. DeWeese and C. Herman, *Int. J. Hyperthermia*, 2015, **31**, 359-374.
262. P. Drake, H.-J. Cho, P.-S. Shih, C.-H. Kao, K.-F. Lee, C.-H. Kuo, X.-Z. Lin and Y.-J. Lin, *J. Mater. Chem.*, 2007, **17**, 4914-4918.
263. P.-S. Jiang, H.-Y. Tsai, P. Drake, F.-N. Wang and C.-S. Chiang, *Int. J. Hyperthermia*, 2017, **33**, 770-778.
264. A. Hervault and N. T. K. Thanh, *Nanoscale*, 2014, **6**, 11553-11573.
265. A. Rajan and N. K. Sahu, *J. Nanopart. Res.*, 2020, **22**, 1-25.
266. M. Bañobre-López, A. Teijeiro and J. Rivas, *Rep Pract Oncol Radiother.*, 2013, **18**, 397-400.
267. C. S. Kumar and F. Mohammad, *Adv. Drug Del. Rev.*, 2011, **63**, 789-808.
268. M. Moros, J. Idiago-López, L. Asín, E. Moreno-Antolín, L. Beola, V. Grazú, R. M. Fratila, L. Gutiérrez and J. M. de la Fuente, *Adv. Drug Del. Rev.*, 2019, **138**, 326-343.
269. S. Nikazar, M. Barani, A. Rahdar, M. Zoghi and G. Z. Kyzas, *ChemistrySelect*, 2020, **5**, 12590-12609.
270. M. W. Tibbitt, J. E. Dahlman and R. Langer, *J. Am. Chem. Soc.*, 2016, **138**, 704-717.
271. J. P. May and S.-D. Li, *Expert Opin. Drug Deliv.*, 2013, **10**, 511-527.
272. H. Hatakeyama, S. Y. Wu, M. S. Lingegowda, C. Rodriguez-Aguayo, G. Lopez-Berestein, L. Ju-Seog, C. Rinaldi, E. J. Juan, A. K. Sood and M. Torres-Lugo, *Mol. Cancer Ther.*, 2017, **16**, 966-976.
273. S. Eynali, S. Khoei, S. Khoee and E. Esmaelbeygi, *Int. J. Hyperthermia*, 2017, **33**, 327-335.

274. M. Torres-Lugo and C. Rinaldi, *Nanomedicine*, 2013, **8**, 1689-1707.
275. N. Datta, S. Krishnan, D. Speiser, E. Neufeld, N. Kuster, S. Bodis and H. Hofmann, *Cancer Treat. Rev.*, 2016, **50**, 217-227.
276. M. L. Tebaldi, C. M. Oda, L. O. Monteiro, A. L. de Barros, C. J. Santos and D. C. F. Soares, *J. Magn. Magn. Mater.*, 2018.
277. C. D. Landon, J.-Y. Park, D. Needham and M. W. Dewhirst, *Open Nanomed J.*, 2011, **3**, 38-64.
278. M. Bonini, D. Berti and P. Baglioni, *Curr. Opin. Colloid Interface Sci.*, 2013, **18**, 459-467.
279. R. Kumari, D. Sunil and R. S. Ningthoujam, *J. Control. Release*, 2020, **319**, 135-156.
280. A. Sharma, J. F. Arambula, S. Koo, R. Kumar, H. Singh, J. L. Sessler and J. S. Kim, *Chem. Soc. Rev.*, 2019, **48**, 771-813.
281. X. Guo, Y. Cheng, X. Zhao, Y. Luo, J. Chen and W.-E. Yuan, *Journal of Nanobiotechnology*, 2018, **16**, 1-10.
282. M. Huo, J. Yuan, L. Tao and Y. Wei, *Polym. Chem.*, 2014, **5**, 1519-1528.
283. L. Zhang, R. Guo, M. Yang, X. Jiang and B. Liu, *Adv. Mater.*, 2007, **19**, 2988-2992.
284. D. Schmaljohann, *Adv. Drug Del. Rev.*, 2006, **58**, 1655-1670.
285. K. Soleimani, E. Arkan, H. Derakhshankhah, B. Haghshenas, R. Jahanban-Esfahlan and M. Jaymand, *Carbohydr. Polym.*, 2021, **252**, 117229.
286. A. Najafipour, A. Gharieh, A. Fassihi, H. Sadeghi-Aliabadi and A. R. Mahdavian, *Mol. Pharm.*, 2020.
287. N. Shahabadi, M. Razlansari, H. Zhaleh and K. Mansouri, *Mater. Sci. Eng.*, 2019, **101**, 472-486.
288. B. T. Mai, S. Fernandes, P. B. Balakrishnan and T. Pellegrino, *Acc. Chem. Res.*, 2018, **51**, 999-1013.
289. S. Yang, D. Chen, N. Li, X. Mei, X. Qi, H. Li, Q. Xu and J. Lu, *J. Mater. Chem.*, 2012, **22**, 25354-25361.
290. X. Yang, J. J. Grailer, I. J. Rowland, A. Javadi, S. A. Hurley, V. Z. Matson, D. A. Steeber and S. Gong, *ACS nano*, 2010, **4**, 6805-6817.
291. B. Wang, C. Xu, J. Xie, Z. Yang and S. Sun, *J. Am. Chem. Soc.*, 2008, **130**, 14436-14437.
292. A. R. K. Sasikala, A. GhavamiNejad, A. R. Unnithan, R. G. Thomas, M. Moon, Y. Y. Jeong, C. H. Park and C. S. Kim, *Nanoscale*, 2015, **7**, 18119-18128.
293. N. Vanparijs, L. Nuhn and B. G. De Geest, *Chem. Soc. Rev.*, 2017, **46**, 1193-1239.
294. M. A. Ward and T. K. Georgiou, *Polymers*, 2011, **3**, 1215-1242.
295. J. Thévenot, H. Oliveira, O. Sandre and S. Lecommandoux, *Chem. Soc. Rev.*, 2013, **42**, 7099-7116.
296. T. Y. Liu, K. H. Liu, D. M. Liu, S. Y. Chen and I. W. Chen, *Adv. Funct. Mater.*, 2009, **19**, 616-623.
297. S. Louguet, B. Rousseau, R. Epherre, N. Guidolin, G. Goglio, S. Mornet, E. Duguet, S. Lecommandoux and C. Schatz, *Polym. Chem.*, 2012, **3**, 1408-1417.
298. J.-F. Lutz, Ö. Akdemir and A. Hoth, *J. Am. Chem. Soc.*, 2006, **128**, 13046-13047.
299. J.-F. Lutz, J. Andrieu, S. Üzgün, C. Rudolph and S. Agarwal, *Macromolecules*, 2007, **40**, 8540-8543.
300. B. T. Mai, P. B. Balakrishnan, M. J. Barthel, F. Piccardi, D. Niculaes, F. Marinaro, S. Fernandes, A. Curcio, H. Kakwere and G. Autret, *ACS Appl. Mater. Interfaces*, 2019.
301. S. Fernandes, T. Fernandez, S. Metze, P. B. Balakrishnan, B. T. Mai, J. Conteh, C. De Mei, A. Turdo, S. Di Franco and G. Stassi, *ACS Appl. Mater. Interfaces*, 2021.
302. T.-J. Li, C.-C. Huang, P.-W. Ruan, K.-Y. Chuang, K.-J. Huang, D.-B. Shieh and C.-S. Yeh, *Biomaterials*, 2013, **34**, 7873-7883.
303. A. Riedinger, P. Guardia, A. Curcio, M. A. Garcia, R. Cingolani, L. Manna and T. Pellegrino, *Nano Lett.*, 2013, **13**, 2399-2406.
304. J. H. Lee, K. J. Chen, S. H. Noh, M. A. Garcia, H. Wang, W. Y. Lin, H. Jeong, B. J. Kong, D. B. Stout and J. Cheon, *Angew. Chem.*, 2013, **125**, 4480-4484.
305. S. H. Hu, B. J. Liao, C. S. Chiang, P. J. Chen, I. W. Chen and S. Y. Chen, *Adv. Mater.*, 2012, **24**, 3627-3632.
306. K. Hayashi, W. Sakamoto and T. Yogo, *Adv. Funct. Mater.*, 2016, **26**, 1708-1718.
307. Z.-Q. Zhang and S.-C. Song, *Biomaterials*, 2017, **132**, 16-27.

308. K. Hayashi, K. Ono, H. Suzuki, M. Sawada, M. Moriya, W. Sakamoto and T. Yogo, *ACS Appl. Mater. Interfaces*, 2010, **2**, 1903-1911.
309. E. G. Fuller, H. Sun, R. D. Dhavalikar, M. Unni, G. M. Scheutz, B. S. Sumerlin and C. Rinaldi, *ACS Appl. Polym. Mater.*, 2019.
310. F. Tang, L. Li and D. Chen, *Adv. Mater.*, 2012, **24**, 1504-1534.
311. X. Yao, X. Niu, K. Ma, P. Huang, J. Grothe, S. Kaskel and Y. Zhu, *Small*, 2017, **13**, 1602225.
312. W. Chen, C.-A. Cheng and J. I. Zink, *ACS nano*, 2019, **13**, 1292-1308.
313. E. Ruiz-Hernandez, A. Baeza and M. Vallet-Regi, *ACS nano*, 2011, **5**, 1259-1266.
314. C. R. Thomas, D. P. Ferris, J. H. Lee, E. Choi, M. H. Cho, E. S. Kim, J. F. Stoddart, J. S. Shin, J. Cheon and J. I. Zink, *J. Am. Chem. Soc.*, 2010, **132**, 10623-10625.
315. B. Rühle, S. Datz, C. Argyo, T. Bein and J. Zink, *Chem. Commun.*, 2016, **52**, 1843-1846.
316. Y. Zhu and C. Tao, *RSC Advances*, 2015, **5**, 22365-22372.
317. F.-C. Lin, Y. Xie, T. Deng and J. I. Zink, *J. Am. Chem. Soc.*, 2021, **143**, 6025-6036.
318. F.-C. Lin and J. I. Zink, *J. Am. Chem. Soc.*, 2020, **142**, 5212-5220.
319. W. Chen, C. A. Glackin, M. A. Horwitz and J. I. Zink, *Acc. Chem. Res.*, 2019, **52**, 1531-1542.
320. C. R. Thomas, D. P. Ferris, J.-H. Lee, E. Choi, M. H. Cho, E. S. Kim, J. F. Stoddart, J.-S. Shin, J. Cheon and J. I. Zink, *J. Am. Chem. Soc.*, 2010, **132**, 10623-10625.
321. U. Bulbake, S. Doppalapudi, N. Kommineni and W. Khan, *Pharmaceutics*, 2017, **9**, 12.
322. Y. Dou, K. Hynynen and C. Allen, *J. Control. Release*, 2017, **249**, 63-73.
323. S. Nardecchia, P. Sánchez-Moreno, J. d. Vicente, J. A. Marchal and H. Boulaiz, *Nanomaterials (Basel, Switzerland)*, 2019, **9**, 191.
324. S. A. T, K. T. Shalumon and J. P. Chen, *Curr. Pharm. Des.*, 2019, **25**, 1490-1504.
325. A. Hardiansyah, M.-C. Yang, T.-Y. Liu, C.-Y. Kuo, L.-Y. Huang and T.-Y. Chan, *Nanoscale Res. Lett.*, 2017, **12**, 355-355.
326. E. Amstad, J. Kohlbrecher, E. Müller, T. Schweizer, M. Textor and E. Reimhult, *Nano Lett.*, 2011, **11**, 1664-1670.
327. H. Guo, W. Chen, X. Sun, Y.-N. Liu, J. Li and J. Wang, *Carbohydr. Polym.*, 2015, **118**, 209-217.
328. A. T S, Y.-J. Lu and J.-P. Chen, *Int. J. Mol. Sci.*, 2020, **21**, 5187.
329. R. Di Corato, G. Béalle, J. Kolosnjaj-Tabi, A. Espinosa, O. Clément, A. K. Silva, C. Ménager and C. Wilhelm, *ACS Nano*, 2015, **9**, 2904-2916.
330. R. V. Ferreira, T. M. Martins, A. M. Goes, J. D. Fabris, L. C. Cavalcante, L. E. Outon and R. Z. Domingues, *Nanotechnology*, 2016, **27**, 085105.
331. S. A. Shah, M. U. Aslam Khan, M. Arshad, S. U. Awan, M. U. Hashmi and N. Ahmad, *Colloids Surf. B. Biointerfaces*, 2016, **148**, 157-164.
332. K. Y. Vlasova, A. Piroyan, I. M. Le-Deygen, H. M. Vishwasrao, J. D. Ramsey, N. L. Klyachko, Y. I. Golovin, P. G. Rudakovskaya, Kireev, II, A. V. Kabanov and M. Sokolsky-Papkov, *J. Colloid Interface Sci.*, 2019, **552**, 689-700.
333. Y. Guo, Y. Zhang, J. Ma, Q. Li, Y. Li, X. Zhou, D. Zhao, H. Song, Q. Chen and X. Zhu, *J. Control. Release*, 2018, **272**, 145-158.
334. W. Lin, X. Xie, Y. Yang, X. Fu, H. Liu, Y. Yang and J. Deng, *Drug Deliv.*, 2016, **23**, 3436-3443.
335. M. Gogoi, M. K. Jaiswal, H. D. Sarma, D. Bahadur and R. Banerjee, *Integrative Biology*, 2017, **9**, 555-565.
336. N. Babincová, P. Sourivong, P. Babinec, C. Bergemann, M. Babincová and Š. Durdík, *Z Naturforsch C J Biosci*, 2018, **73**, 265-271.
337. Y.-J. Lu, E.-Y. Chuang, Y.-H. Cheng, T. S. Anilkumar, H.-A. Chen and J.-P. Chen, *Chem. Eng. J.*, 2019, **373**, 720-733.
338. G. Béalle, R. Di Corato, J. Kolosnjaj-Tabi, V. Dupuis, O. Clément, F. Gazeau, C. Wilhelm and C. Ménager, *Langmuir*, 2012, **28**, 11834-11842.

339. M. Gogoi, N. Kumar and S. Patra, *Nanoarchitectonics for Smart Delivery and Drug Targeting*, 2016, **pp**, 743-782.
340. S. H. Alavizadeh, F. Gheybi, A. R. Nikpoor, A. Badiee, S. Golmohammadzadeh and M. R. Jaafari, *Mol. Pharm.*, 2017, **14**, 712-721.
341. F. Meng, Z. Zhong and J. Feijen, *Biomacromolecules*, 2009, **10**, 197-209.
342. D. E. Discher and F. Ahmed, *Annu. Rev. Biomed. Eng.*, 2006, **8**, 323-341.
343. B. T. Mai, M. Barthel, R. Marotta and T. Pellegrino, *Polymer*, 2019, **165**, 19-27.
344. H. Oliveira, E. Pérez-Andrés, J. Thevenot, O. Sandre, E. Berra and S. Lecommandoux, *J. Control. Release*, 2013, **169**, 165-170.
345. C. Sanson, O. Diou, J. Thevenot, E. Ibarboure, A. Soum, A. Brûlet, S. Miraux, E. Thiaudière, S. Tan and A. Brisson, *ACS nano*, 2011, **5**, 1122-1140.
346. S. Acharya and S. K. Sahoo, *Adv. Drug Del. Rev.*, 2011, **63**, 170-183.
347. I. Bala, S. Hariharan and M. R. Kumar, *Crit. Rev. Ther. Drug Carrier Syst.*, 2004, **21**.
348. A. R. G. Sivakumar Balasubramanian, Y. Nagaoka, S. Iwai, M. Suzuki, V. Kizhikkilot, Y. Yoshida, T. Maekawa and S. D. Nair, *Int. J. Nanomed.*, 2014, **9**, 437.
349. K. Hayashi, M. Nakamura, H. Miki, S. Ozaki, M. Abe, T. Matsumoto, W. Sakamoto, T. Yogo and K. Ishimura, *Theranostics*, 2014, **4**, 834.
350. S. R. Veloso, R. G. Andrade and E. M. Castanheira, *Adv. Colloid Interface Sci.*, 2021, **288**, 102351.
351. R.-Z. Tang, Z.-Z. Liu, S.-S. Gu and X.-Q. Liu, *J. Mater. Chem. B*, 2021, **9**, 1521-1535.
352. S. R. Veloso, R. G. Andrade, B. C. Ribeiro, A. V. Fernandes, A. R. O. Rodrigues, J. Martins, P. M. Ferreira, P. J. Coutinho and E. Castanheira, *Nanomaterials*, 2020, **10**, 1702.
353. K.-Y. Qian, Y. Song, X. Yan, L. Dong, J. Xue, Y. Xu, B. Wang, B. Cao, Q. Hou and W. Peng, *Biomaterials*, 2020, **259**, 120299.
354. H. T. Nguyen, T. T. P. Tran, S. G. Jin, C. S. Yong, D. H. Truong, T. H. Tran and J. O. Kim, *J. Pharm. Investig.*, 2019, **49**, 519-526.
355. S. Yu, C. He and X. Chen, *Macromol. Biosci.*, 2018, **18**, 1800240.
356. S. R. Veloso, P. M. Ferreira, J. A. Martins, P. J. Coutinho and E. Castanheira, *Pharmaceutics*, 2018, **10**, 145.
357. M. Sepantafar, R. Maheronnaghsh, H. Mohammadi, F. Radmanesh, M. M. Hasani-Sadrabadi, M. Ebrahimi and H. Baharvand, *Trends Biotechnol.*, 2017, **35**, 1074-1087.
358. Y.-J. Liang, H. Wang, H. Yu, G. Feng, F. Liu, M. Ma, Y. Zhang and N. Gu, *Colloids Surf. Physicochem. Eng. Aspects*, 2020, **588**, 124364.
359. Y. Yang, F. Wang, K. Zheng, L. Deng, L. Yang, N. Zhang, C. Xu, H. Ran, Z. Wang and Z. Wang, *PLoS One*, 2017, **12**, e0177049.
360. W. Gao, Y. Zheng, R. Wang, H. Chen, X. Cai, G. Lu, L. Chu, C. Xu, N. Zhang and Z. Wang, *Acta Biomater.*, 2016, **29**, 298-306.
361. K. Fang, L. Song, Z. Gu, F. Yang, Y. Zhang and N. Gu, *Colloids Surf. B. Biointerfaces*, 2015, **136**, 712-720.
362. J. Yu, K. Wang, C. Fan, X. Zhao, J. Gao, W. Jing, X. Zhang, J. Li, Y. Li and J. Yang, *Adv. Mater.*, 2021, **33**, 2008395.
363. P. Yuan, T. Yang, T. Liu, X. Yu, Y. Bai, Y. Zhang and X. Chen, *Biomaterials*, 2020, **262**, 120357.
364. X. Dai, Y. Zhang, L. Gao, T. Bai, W. Wang, Y. Cui and W. Liu, *Adv. Mater.*, 2015, **27**, 3566-3571.
365. J. I. Kim, B. Kim, C. Chun, S. H. Lee and S.-C. Song, *Biomaterials*, 2012, **33**, 4836-4842.
366. S. Brulé, M. Levy, C. Wilhelm, D. Letourneur, F. Gazeau, C. Ménager and C. Le Visage, *Adv. Mater.*, 2011, **23**, 787-790.
367. W. Xie, Q. Gao, Z. Guo, D. Wang, F. Gao, X. Wang, Y. Wei and L. Zhao, *ACS Appl. Mater. Interfaces*, 2017, **9**, 33660-33673.

368. F. Gao, W. Xie, Y. Miao, D. Wang, Z. Guo, A. Ghosal, Y. Li, Y. Wei, S. S. Feng and L. Zhao, *Advanced healthcare materials*, 2019, **8**, 1900203.
369. C. Wang, N. Zhao, Y. Huang, R. He, S. Xu and W. Yuan, *Chem. Eng. J.*, 2020, **401**, 126100.
370. X. Zhou, L. Wang, Y. Xu, W. Du, X. Cai, F. Wang, Y. Ling, H. Chen, Z. Wang and B. Hu, *RSC advances*, 2018, **8**, 9812-9821.
371. H. Wu, L. Song, L. Chen, W. Zhang, Y. Chen, F. Zang, H. Chen, M. Ma, N. Gu and Y. Zhang, *Acta Biomater.*, 2018, **74**, 302-311.
372. G. Dai, L. Sun, J. Xu, G. Zhao, Z. Tan, C. Wang, X. Sun, K. Xu and W. Zhong, *Acta Biomater.*, 2021.
373. J. Pan, P. Hu, Y. Guo, J. Hao, D. Ni, Y. Xu, Q. Bao, H. Yao, C. Wei and Q. Wu, *ACS nano*, 2020.
374. S.-h. Noh, S. H. Moon, T.-H. Shin, Y. Lim and J. Cheon, *Nano Today*, 2017, **13**, 61-76.
375. A. Espinosa, J. Kolosnjaj-Tabi, A. Abou-Hassan, A. Plan Sangnier, A. Curcio, A. K. Silva, R. Di Corato, S. Neveu, T. Pellegrino and L. M. Liz-Marzán, *Adv. Funct. Mater.*, 2018, **28**, 1803660.
376. Y. Chen, L. Li, W. Chen, H. Chen and J. Yin, *Chin. Chem. Lett.*, 2019, **30**, 1353-1360.
377. C. Bohren and D. Huffman, *John Wiley & Sons*, 1983.
378. U. Kreibig and M. Vollmer, *Optical properties of metal clusters*, Springer Science & Business Media, 2013.
379. D. Pissuwan, S. M. Valenzuela and M. B. Cortie, *Trends Biotechnol.*, 2006, **2**, 62-67.
380. X. Huang, P. K. Jain, I. H. El-Sayed and M. A. El-Sayed, *Lasers Med. Sci.*, 2008, **23**, 217.
381. Z. Bao, X. Liu, Y. Liu, H. Liu and K. Zhao, *Asian J. Pharm.*, 2016, **11**, 349-364.
382. J. Estelrich and M. A. Busquets, *Molecules*, 2018, **23**, 1567.
383. A. R. Rastinehad, H. Anastos, E. Wajswol, J. S. Winoker, J. P. Sfakianos, S. K. Doppalapudi, M. R. Carrick, C. J. Knauer, B. Taouli and S. C. Lewis, *Proceedings of the National Academy of Sciences*, 2019, **116**, 18590-18596.
384. N. Teraphongphom, C. S. Kong, J. M. Warram and E. L. Rosenthal, *Laryngoscope Investig.*, 2017, **2**, 447-452.
385. Q. Lu, X. Dai, P. Zhang, X. Tan, Y. Zhong, C. Yao, M. Song, G. Song, Z. Zhang and G. Peng, *Int. J. Nanomed.*, 2018, **13**, 2491.
386. S. Shen, S. Wang, R. Zheng, X. Zhu, X. Jiang, D. Fu and W. Yang, *Biomaterials*, 2015, **39**, 67-74.
387. S. Shen, F. Kong, X. Guo, L. Wu, H. Shen, M. Xie, X. Wang, Y. Jin and Y. Ge, *Nanoscale*, 2013, **5**, 8056-8066.
388. H. Yan, W. Shang, X. Sun, L. Zhao, J. Wang, Z. Xiong, J. Yuan, R. Zhang, Q. Huang and K. Wang, *Adv. Funct. Mater.*, 2018, **28**, 1705710.
389. A. M. Smith, M. C. Mancini and S. Nie, *Nat. Nanotechnol.*, 2009, **4**, 710-711.
390. E. Hemmer, A. Benayas, F. Légaré and F. Vetrone, *Nanoscale Horizons*, 2016, **1**, 168-184.
391. Y. Cai, Z. Wei, C. Song, C. Tang, W. Han and X. Dong, *Chem. Soc. Rev.*, 2019, **48**, 22-37.
392. Y. Liu, Q. Jia and J. Zhou, *Adv. Ther.*, 2018, **1**, 1800055.
393. F. Yang, A. Skripka, M. S. Tabatabaei, S. H. Hong, F. Ren, Y. Huang, J. K. Oh, S. Martel, X. Liu and F. Vetrone, *Chem. Mater.*, 2019, **31**, 3201-3210.
394. R. R. Allison, G. H. Downie, R. Cuenca, X.-H. Hu, C. J. Childs and C. H. Sibata, *Photodiagnosis Photodyn. Ther.*, 2004, **1**, 27-42.
395. A. P. Castano, T. N. Demidova and M. R. Hamblin, *Photodiagnosis Photodyn. Ther.*, 2004, **1**, 279-293.
396. M. R. Detty, S. L. Gibson and S. J. Wagner, *J. Med. Chem.*, 2004, **47**, 3897-3915.
397. T. J. Dougherty, in *Endoscopic Laser Surgery Handbook*, Marcel Dekker Inc New York, 1987, p. 424.
398. T. J. Dougherty, C. J. Gomer, B. W. Henderson, G. Jori, D. Kessel, M. Korbelik, J. Moan and Q. Peng, *J. Natl. Cancer Inst.*, 1998, **90**, 889-905.
399. S. W. Flanagan, P. L. Moseley and G. R. Buettner, *FEBS Lett.*, 1998, **431**, 285-286.
400. C.-H. Hou, F.-L. Lin, S.-M. Hou and J.-F. Liu, *Int. J. Mol. Sci.*, 2014, **15**, 17380-17395.

401. K. S. Kim, J. Kim, J. Y. Lee, S. Matsuda, S. Hideshima, Y. Mori, T. Osaka and K. Na, *Nanoscale*, 2016, **8**, 11625-11634.
402. A. Ribas and J. D. Wolchok, *Science*, 2018, **359**, 1350-+.
403. Y. Singh, V. K. Pawar, J. G. Meher, K. Raval, A. Kumar, R. Shrivastava, S. Bhadauria and M. K. Chourasia, *J. Control. Release*, 2017, **254**, 92-106.
404. F. Galli, J. V. Aguilera, B. Palermo, S. N. Markovic, P. Nisticò and A. Signore, *J. Exp. Clin. Cancer Res.*, 2020, **39**, 1-21.
405. J.-M. Anaya, Y. Shoenfeld, A. Rojas-Villarraga, R. A. Levy and R. Cervera, 2013.
406. H.-G. Zhang, K. Mehta, P. Cohen and C. Guha, *Cancer Lett.*, 2008, **271**, 191-204.
407. J. J. Skitzki, E. A. Repasky and S. S. Evans, *Current Opin. Investig. Drugs*, 2009, **10**, 550.
408. E. Strauch, D. Fabian, J. Turner and A. Lefor, *Surg. Oncol.*, 1994, **3**, 45-52.
409. T. Kobayashi, K. Kakimi, E. Nakayama and K. Jimbow, *Nanomedicine*, 2014, **9**, 1715-1726.
410. S. S. Evans, E. A. Repasky and D. T. Fisher, *Nat. Rev. Immunol.*, 2015, **15**, 335-349.
411. H.-Y. Wang, J. C.-M. Fu, Y.-C. Lee and P.-J. Lu, *Mol. Cell. Biol.*, 2013, **33**, 4889-4899.
412. A. Ito, H. Honda and T. Kobayashi, *Cancer Immunol. Immunother.*, 2006, **55**, 320-328.
413. J. M. Tarr, P. J. Young, R. Morse, D. J. Shaw, R. Haigh, P. G. Petrov, S. J. Johnson, P. G. Winyard and P. Eggleton, *J. Mol. Biol.*, 2010, **401**, 799-812.
414. L. Beola, V. Grazú, Y. Fernández-Afonso, R. M. Fratila, M. de Las Heras, J. s. M. de la Fuente, L. Gutiérrez and L. Asín, *ACS Appl. Mater. Interfaces*, 2021.
415. M. Paulides, H. D. Trefna, S. Curto and D. Rodrigues, *Adv. Drug Del. Rev.*, 2020, **163**, 3-18.
416. A. A. Petryk, A. J. Giustini, R. E. Gottesman, B. S. Trembly and P. J. Hoopes, *Int. J. Hyperthermia*, 2013, **29**, 819-827.
417. F. K. van Landeghem, K. Maier-Hauff, A. Jordan, K.-T. Hoffmann, U. Gneveckow, R. Scholz, B. Thiesen, W. Brück and A. von Deimling, *Biomaterials*, 2009, **30**, 52-57.
418. A. Chauhan, S. Midha, R. Kumar, R. Meena, P. Singh, S. K. Jha and B. K. Kuanr, *Biomaterials science*, 2021, **9**, 2972-2990.
419. T. J. Carter, G. Agliardi, F. Y. Lin, M. Ellis, C. Jones, M. Robson, A. Richard-Londt, P. Southern, M. Lythgoe and M. Zaw Thin, *Small*, 2021, **17**, 2005241.
420. L. Beola, V. Grazú, Y. Fernández-Afonso, R. M. Fratila, M. de Las Heras, J. s. M. de la Fuente, L. Gutiérrez and L. Asín, *ACS Appl. Mater. Interfaces*, 2021, **13**, 12982-12996.
421. S. Zanganeh, G. Hutter, R. Spitler, O. Lenkov, M. Mahmoudi, A. Shaw, J. S. Pajarinen, H. Nejadnik, S. Goodman and M. Moseley, *Nat. Nanotechnol.*, 2016, **11**, 986-994.
422. K. Liberek, A. Lewandowska and S. Zietkiewicz, *EMBO J.*, 2008, **27**, 328-335.
423. S. K. Calderwood and D. R. Ciocca, *Int. J. Hyperthermia*, 2008, **24**, 31-39.
424. K. Ohnishi, A. Takahashi, S. Yokota and T. Ohnishi, *Int. J. Radiat. Biol.*, 2004, **80**, 607-614.
425. S. K. Calderwood, M. A. Khaleque, D. B. Sawyer and D. R. Ciocca, *Trends Biochem. Sci.*, 2006, **31**, 164-172.
426. S. M. Todryk, A. A. Melcher, A. G. Dalgleish and R. G. Vile, *Immunology*, 2000, **99**, 334-337.
427. S. Basu and P. K. Srivastava, *Cell Stress Chaperones*, 2000, **5**, 443.
428. A. Sato, Y. Tamura, N. Sato, T. Yamashita, T. Takada, M. Sato, Y. Osai, M. Okura, I. Ono, A. Ito, H. Honda, K. Wakamatsu, S. Ito and K. Jimbow, *Cancer Sci.*, 2010, **101**, 1939-1946.
429. T. Takada, T. Yamashita, M. Sato, A. Sato, I. Ono, Y. Tamura, N. Sato, A. Miyamoto, A. Ito and H. Honda, *J. Biomed. Biotechnol.*, 2009, **2009**.
430. A. Ito, F. Matsuoka, H. Honda and T. Kobayashi, *Cancer Gene Ther.*, 2003, **10**, 918-925.
431. K. Tanaka, A. Ito, T. Kobayashi, T. Kawamura, S. Shimada, K. Matsumoto, T. Saida and H. Honda, *Int. J. Cancer*, 2005, **116**, 624-633.
432. R. Guanghui, H. Xiaoyan, Y. Shuyi, C. Jun and Q. Guobin, *J. Biochem. Mol. Toxicol.*, 2019, **33**, e22339.

433. P. Berraondo, M. F. Sanmamed, M. C. Ochoa, I. Etxeberria, M. A. Aznar, J. L. Pérez-Gracia, M. E. Rodríguez-Ruiz, M. Ponz-Sarvise, E. Castañón and I. Melero, *Br. J. Cancer*, 2019, **120**, 6-15.
434. A. Ito, K. Tanaka, K. Kondo, M. Shinkai, H. Honda, K. Matsumoto, T. Saida and T. Kobayashi, *Cancer Sci.*, 2003, **94**, 308-313.
435. W. L. Farrar, H. M. Johnson and J. J. Farrar, *J. Immunol.*, 1981, **126**, 1120-1125.
436. K. Shimizu, R. C. Fields, M. Giedlin and J. J. Mule, *Proc. Natl. Acad. Sci. U. S. A.*, 1999, **96**, 2268-2273.
437. S. Toraya-Brown, M. R. Sheen, P. Zhang, L. Chen, J. R. Baird, E. Demidenko, M. J. Turk, P. J. Hoopes, J. R. Conejo-Garcia and S. Fiering, in *Handbook of immunological properties of engineered nanomaterials: Volume 3: Engineered Nanomaterials and the Immune Cell Function*, World Scientific, 2016, pp. 309-347.
438. E. Alphandéry, A. Idbaih, C. Adam, J.-Y. Delattre, C. Schmitt, F. Guyot and I. Chebbi, *J. Control. Release*, 2017, **262**, 259-272.
439. D. S. Vinay, E. P. Ryan, G. Pawelec, W. H. Talib, J. Stagg, E. Elkord, T. Lichtor, W. K. Decker, R. L. Whelan and H. S. Kumara, 2015.
440. J. A. Seidel, A. Otsuka and K. Kabashima, *Front. Oncol.*, 2018, **8**, 86.
441. Y. Chao, G. Chen, C. Liang, J. Xu, Z. Dong, X. Han, C. Wang and Z. Liu, *Nano Lett.*, 2019, **19**, 4287-4296.
442. Z. Wang, F. Zhang, D. Shao, Z. Chang, L. Wang, H. Hu, X. Zheng, X. Li, F. Chen and Z. Tu, *Adv. Sci.*, 2019, **6**, 1901690.
443. X. Liu, J. Zheng, W. Sun, X. Zhao, Y. Li, N. Gong, Y. Wang, X. Ma, T. Zhang and L.-Y. Zhao, *ACS nano*, 2019, **13**, 8811-8825.
444. S. A. Collins, B.-a. Guinn, P. T. Harrison, M. F. Scallan, G. C. O'Sullivan and M. Tangney, *Curr. Gene Ther.*, 2008, **8**, 66-78.
445. P. Lamichhane, R. Deshmukh, J. A. Brown, S. Jakubski, P. Parajuli, T. Nolan, D. Raja, M. Badawy, T. Yoon, M. Zmiyiwsky and N. Lamichhane, *Medicines*, 2019, **6**.
446. Z. S. Guo, B. Lu, Z. Guo, E. Giehl, M. Feist, E. Dai, W. Liu, W. J. Storkus, Y. He and Z. Liu, *J. Immunother.*, 2019, **7**, 1-21.
447. P. J. Hoopes, K. L. Moodie, A. A. Petryk, J. D. Petryk, S. Sechrist, D. J. Gladstone, N. F. Steinmetz, F. A. Veliz, A. A. Bursey and R. J. Wagner, 2017.
448. M. Zheng, J. Huang, A. Tong and H. Yang, *Molecular Therapy-Oncolytics*, 2019, **15**, 234-247.
449. C. Dai, C. Wang, R. Hu, H. Lin, Z. Liu, L. Yu, Y. Chen and B. Zhang, *Biomaterials*, 2019, **219**, 119374.
450. A. Quarta, D. Bernareggi, F. Benigni, E. Luison, G. Nano, S. Nitti, M. C. Cesta, L. Di Ciccio, S. Canevari and T. Pellegrino, *Nanoscale*, 2015, **7**, 2336-2351.
451. L. Zhang, H. Chen, L. Wang, T. Liu, J. Yeh, G. Lu, L. Yang and H. Mao, *Nanotechnol. Sci. Appl*, 2010, **3**, 159.
452. I. Tsiapa, E. K. Efthimiadou, E. Fragogeorgi, G. Loudos, A. D. Varvarigou, P. Bouziotis, G. C. Kordas, D. Mihailidis, G. C. Nikiforidis and S. Xanthopoulos, *J. Colloid Interface Sci.*, 2014, **433**, 163-175.
453. M. Radović, M. P. Calatayud, G. F. Goya, M. R. Ibarra, B. Antić, V. Spasojević, N. Nikolić, D. Janković, M. Mirković and S. Vranješ-Đurić, *J. Biomed. Mater. Res. A*, 2015, **103**, 126-134.
454. S. J. DeNardo, G. L. DeNardo, A. Natarajan, L. A. Miers, A. R. Foreman, C. Gruettner, G. N. Adamson and R. Ivkov, *J. Nucl. Med.*, 2007, **48**, 437-444.
455. B. T. Mai, P. B. Balakrishnan, M. J. Barthel, F. Piccardi, D. Niculaes, F. Marinaro, S. Fernandes, A. Curcio, H. Kakwere, G. Autret, R. Cingolani, F. Gazeau and T. Pellegrino, *ACS Appl Mater Interfaces*, 2019, **11**, 5727-5739.
456. L. Lartigue, D. Alloyeau, J. Kolosnjaj-Tabi, Y. Javed, P. Guardia, A. Riedinger, C. Pechoux, T. Pellegrino, C. Wilhelm and F. Gazeaut, *Acs Nano*, 2013, **7**, 3939-3952.
457. C. Lei, Y. Sun, D. C. Tsang and D. Lin, *Environ. Pollut.*, 2018, **232**, 10-30.

458. L. Sercombe, T. Veerati, F. Moheimani, S. Y. Wu, A. K. Sood and S. Hua, *Front. Pharmacol.*, 2015, **6**, 286-286.
459. E. Beltrán-Gracia, A. López-Camacho, I. Higuera-Ciapara, J. B. Velázquez-Fernández and A. A. Vallejo-Cardona, *Cancer Nanotechnol.*, 2019, **10**, 11.
460. L. R. Baden, H. M. El Sahly, B. Essink, K. Kotloff, S. Frey, R. Novak, D. Diemert, S. A. Spector, N. Rouphael and C. B. Creech, *N. Engl. J. Med.*, 2021, **384**, 403-416.
461. F. P. Polack, S. J. Thomas, N. Kitchin, J. Absalon, A. Gurtman, S. Lockhart, J. L. Perez, G. Pérez Marc, E. D. Moreira and C. Zerbini, *N. Engl. J. Med.*, 2020, **383**, 2603-2615.
462. X. Jiang, B. Q. Li, X. Qu, H. Yang and H. Liu, *J. Mater. Chem. B*, 2017, **5**, 8983-8990.
463. A. Benayas, F. Ren, E. Carrasco, V. Marzal, B. del Rosal, B. A. Gonfa, Á. Juarranz, F. Sanz-Rodríguez, D. Jaque and J. García-Solé, *Adv. Funct. Mater.*, 2015, **25**, 6650-6659.
464. B. del Rosal, D. Ruiz, I. Chaves-Coira, B. H. Juárez, L. Monge, G. Hong, N. Fernández and D. Jaque, *Adv. Funct. Mater.*, 2018, **28**, 1806088.
465. D. Ruiz, B. del Rosal, M. Acebrón, C. Palencia, C. Sun, J. Cabanillas-González, M. López-Haro, A. B. Hungría, D. Jaque and B. H. Juarez, *Adv. Funct. Mater.*, 2017, **27**, 1604629.
466. J. Zhou, B. Del Rosal, D. Jaque, S. Uchiyama and D. Jin, *Nat. Methods*, 2020, **17**, 967-980.
467. E. N. Cerón, D. H. Ortgies, B. Del Rosal, F. Ren, A. Benayas, F. Vetrone, D. Ma, F. Sanz-Rodríguez, J. G. Solé and D. Jaque, *Adv. Mater.*, 2015, **27**, 4781-4787.
468. D. Le Bihan, J. Delannoy and R. L. Levin, *Radiology*, 1989, **171**, 853-857.
469. A. V. Makela, J. M. Gaudet, M. A. Schott, O. C. Sehl, C. H. Contag and P. J. Foster, *Mol. Imaging Biol.*, 2020, 1-11.
470. B. Zheng, T. Vazin, P. W. Goodwill, A. Conway, A. Verma, E. U. Saritas, D. Schaffer and S. M. Conolly, *Sci. Rep.*, 2015, **5**, 1-9.
471. A. Rivera-Rodriguez, L. B. Hoang-Minh, A. Chiu-Lam, N. Sarna, L. Marrero-Morales, D. A. Mitchell and C. Rinaldi, *bioRxiv*, 2020.
472. P. Chandrasekharan, Z. W. Tay, D. Hensley, X. Y. Zhou, B. K. Fung, C. Colson, Y. Lu, B. D. Fellows, Q. Huynh and C. Saayujya, *Theranostics*, 2020, **10**, 2965.
473. Y. Lu, A. Rivera-Rodriguez, Z. W. Tay, D. Hensley, K. B. Fung, C. Colson, C. Saayujya, Q. Huynh, L. Kabuli and B. Fellows, *Int. J. Hyperthermia*, 2020, **37**, 141-154.

Teresa Pellegrino, received her master in Chemistry in 2000 and her Ph.D. in Chemical Synthesis and Applied Enzymatic Chemistry in 2005 from the University of Bari, Italy. After being Post Doc at National Nanotechnology laboratory in Lecce and a permanent staff scientist at the Nanotech Center of CNR, since 2014 she is tenured team leader of the Nanomaterials for Biomedical Applications group at the Italian Institute of Technology, Genoa, Italy. Her current research interests focus on the development of inorganic nanostructures for drug delivery, magnetic hyperthermia, photo-thermal treatment and radiotherapy exploiting cation exchange radio-protocols. She has been the recipient of the ERC-Starting grant ICARO (GA 678109) and the ERC-proof of principle Hypercube (GA 899661). At IIT, she has generated 9 families of patents and 23 applications. She has co-authored over 130 peer-reviewed papers in international journals in the field of nanoscience, chemistry, nanomedicine and drug.

Helena Gavilán, received her master in Chemical Science and Technology in 2014 and her Ph.D. in Advanced Chemistry in 2017 from the Complutense University of Madrid (UCM), Spain. She is a senior Postdoc at Dr. Teresa Pellegrino's group at IIT since 2018. Her field of expertise is the colloidal synthesis and characterization of magnetic nanoparticles designed for biomedical applications. She has 7 years of experience in the solvothermal and hydrothermal synthesis of nanoparticles and she is co-author of 20 scientific puplicatio in peer review journals. Working at IIT, she explores methods for the gram-scale preparation of ferrite nanoparticles with optimal properties for magnetic hyperthermia. Her current research interests focus on the development of inorganic nanostructures for magnetic hyperthermia and photothermia and she is involved in the start-up project HyperCube.

TABLE OF CONTENT